NUMERICAL OPTIMIZATION OF CRYOGENIC SEPARATION OF OIL SANDS AND CLAY IN FLUIDIZED BEDS

by

Mohsen Bayati

A thesis submitted in partial fulfillment of the requirements for the degree of

Master of Science

Department of Mechanical Engineering

University of Alberta

ABSTRACT

Fluidized beds offer efficient solutions for segregation of clay and bitumen pellets in the oil production industry. However, the hydrodynamics of these systems is not well-known and they are mostly operated as "black box". The removal of clay pellets in the mechanical separation of oil sands method, requires an efficient method of separation of the pellets. By using computational fluid dynamics (CFD), the hydrodynamics of these equipments can be studied and the affecting parameters on the flow behavior be identified. In this thesis challenges in preparation of a validated CFD model are addressed and the effects of design and operating parameters on the efficiency of the method are studied. The Eulerian-Lagrangian approach is used in the CFD simulations of a slice of the bed and results are compared to a 3D full size bed and to results from literature for validation. The first study is dedicated to the analysis of the fluidization process in a fluidized bed formed with mono-dispersed sand particles. Results of the simulations are compared against experimental data and empirical solutions. A validated and grid-converged numerical model which can present the hydrodynamics of the fluidized bed is the outcome of this study. Later, bitumen pellets are added to the fluidized bed simulations, as the third phase, to study the segregation process. Results of simulations are compared to the published experimental and analytical works. To study the effect of design and operating parameters of the fluidized bed on the segregation of particles, the density ratio of the particles is decreased to increase the sensitivity of the problem. The results of the simulations showed that the carrier phase properties, as well as the width and

the height of the bed, are not affecting the final degree of the mixture. However, the rate of segregation of particles is increased by reducing the static height of the bed. Also, the model showed that there should be an optimum inlet velocity at which the rate of segregation of particles is fastest and which produces the best level of segregation of particles, as expected. Among the tested values in the current study the inlet velocity of 1.25 times the minimum fluidization velocity of the jetsam was the fastest rate of segregation and most segregated state of the mixture.

To my dear mother, ***Farah****, and my late father,* ***Mehdi****.*

For all their love, kindness and support.

ACKNOWLEDGEMENT

I would like to acknowledge my supervisor, Dr. Carlos F. Lange, for his kind and continuous help and understanding.

Also I would like to acknowledge the WestGrid (www.westgrid.ca) and Compute Canada Calcul Canada (www.computecanada.ca) by which this computationally extensive research was enabled.

Table of Contents

List of Figures

List of Tables

List of Symbols and Nomenclatures

Greek

β	Fluid-particle friction coefficient (kg m^{-3} s^{-1})
δ_n	Displacement of the particle in normal direction (m)
δ_t	Displacement of the particle in tangential direction (m)
ϵ_g	Gas void fraction (-)
$\epsilon_{g,mf}$	Gas void fraction at minimum fluidization condition (-)
ϵ_s	Particles void fraction (-)
η_{nj}	Damping coefficient of the particle in normal direction (-)
η_{tj}	Damping coefficient of the particle in tangential direction (-)
Θ	Granular temperature (m^2 s^{-2})
γ	Dissipation due to inelastic collisions (-)
ν	Poisson ratio (-)

ω Particle angular velocity (s^{-1})

ϕ_s Sphericity of the particle (-)

ρ_g Gas density (kg m^{-3})

$\rho_{p,i}$ Density of particle i (kg m^{-3})

ρ_s Solid density (kg m^{-3})

τ Reynolds shear stress (kg m^{-1} s^{-2})

μ_g Gas viscosity (kg m^{-1} s^{-1})

ξ A constant for drag factor (-)

Roman

A Cross-sectional area of the bed (m^2)

A_p Particle projection area (m^2)

C_D Drag coefficient (-)

C Particles' velocity fluctuations (m s^{-2})

d Diameter of the particle (m)

$\overline{d}_p$ Mean diameter of the particles (m)

d^* Dimensionless measure of particle diameter (-)

f Drag factor (-)

e Coefficient of restitution (-)

F A constant for drag factor (-)

F_0 A constant for drag factor (-)

F_3 A constant for drag factor (-)

$\mathbf{f}_{drag,i}$ Drag force on particle i (kg m s^{-2})

$\mathbf{f}_{p-f,i}$ The force imposed by the carrier phase to particle i (kg m s^{-2})

$\mathbf{F}_{nij}$ Normal force between particles i and j (kg m s^{-2})

$\mathbf{F}_{tij}$ Tangential force between particles i and j (kg m s^{-2})

$\mathbf{f}_{c,ij}$ Contact force between particles i and j

$\mathbf{f}_{d,ij}$ Damping force between particles i and j

$\mathbf{F}^A$ Volumetric particle-fluid interaction force, model A (kg m s^{-2})

$\mathbf{F}^B$ Volumetric particle-fluid interaction force, model B (kg m s^{-2})

g Gravity acceleration (m s^{-2})

$\mathbf{G}$ Relative velocity of particle at contact point (m s^{-1})

$\mathbf{G}_{ct}$ Slip velocity of particle at contact point (m s^{-1})

G Shear modulus (kg m^{-1} s^{-2})

H Static height of the bed (m)

$\mathbf{I}_i$ Rotational inertial momentum of particle i (kg m^2)

k	Permeability (m^2)
k_n	Stiffness in normal direction (-)
k_t	Stiffness in tangential direction (-)
L	Length of the bed (m)
m_i	Mass of the particle i (kg)
$\mathbf{n}$	Normal vector
k_c	Total number of particles in a computational cell (-)
n	Number of particles (-)
P	Overall portion of a component of the mixture (-)
Δp_o	Hydrostatic pressure drop (kg m^{-1} s^{-2})
Δp_d	Hydrodynamic pressure drop (kg m^{-1} s^{-2})
Δp	Total pressure drop (kg m^{-1} s^{-2})
P_s	Solid pressure (kg m^{-1} s^{-2})
Δp_w	Frictional pressure drop (kg m^{-1} s^{-2})
r	Particle radius (m)
Re	Reynolds Number
T_g	Gas phase stress tensor (kg m^{-1} s^{-2})
T_s	Solid phase stress tensor (kg m^{-1} s^{-2})

U_{mf} Superficial inlet velocity of the gas at minimum fluidization condition (m s^{-1})

$U_{mf,jetsam}$ Minimum fluidization velocity of the jetsam (m s^{-1})

$\mathbf{v}$ Particle velocity (m s^{-1})

u^* Dimensionless gas velocity (-)

U Superficial inlet velocity of the gas (m s^{-1})

$V_{p,i}$ Volume of the particle i (m^3)

∇V Volume of the computational cell (m^3)

W Total weight of the particles (kg m s^{-1})

Y Young modulus (kg m^{-1} s^{-2})

Chapter 1

Introduction

Canada has the world's third-largest proved reserves of crude oil, ninety percent of which, or 169 billion barrels, are found in the tar sands. Considering the daily production rate of oil from the Alberta's tar sands, 2.3 million bpd in 2014 [Alberta, 2016], it is imperative to develop new methods of oil extraction to reduce the cost of the production and the footprint on the landscape [Honarvar et al., 2011].

Current methods of extraction of oil from tar sands, surface mining, steam assisted gravity drainage (SAGD), cyclic steam stimulation (CSS) or vapor extraction (VAPEX), require tremendous amounts of water, up to ten times the produced oil, energy and sometimes solvents. The Energy Returned On Energy Invested "EROEI" of these methods is about 5 to 6 [Board, 2006], which increases the total production cost and has serious effects on the environment. Also, residual hydrocarbons along with the clay are disposed of in oil sand tailing ponds, which are another concern of environmentalists. A new approach with a higher EROEI, which consumes fewer resources, while producing less pollution, is required to turn oil sands business into an efficient and green business.

A novel method was proposed and patented by Duma [2012] for mechanical processing of tar sands. In this process pellets of tar sands are formed by grinding oil sands and cooling down below the transition temperature, -25 °F, so that they do not aggregate and remain as distinct units. Because of impurities in the ore, a fraction of the pellets will unavoidably contain only clay, instead of oil sands. After pelletization, the clay pellets are separated from the oil sand pellets by means of a fluidized bed. Later, pellets are fractured using mechanical methods, e.g. by a ball mill or a hammer mill, to separate the bitumen from the sand.

A key point in this process is an efficient method of separation of clay and bitumen pellets in the fluidized bed. This will remove clay in the early stages of the process. This thesis aims to examine the process of separation of oil sand pellets from clay pellets in the fluidized bed of the mechanical processing of tar sands method.

It was early 1930's that the fluidization process and fluidized beds were introduced to the industry and they were developed more after World War II when a group of companies, Standard Oil New Jersey, M.W. Kellogg, Shell and Universal Oil Products designed the catalytic cracking method for gasoline [Yates, 2013]. "Fine solid particles are transformed into a fluid-like state, when they are in contact with a flow of gas, and they possess the behavior of a fluid" [Kunii and Levenspiel, 1997].

Researchers have performed numerous investigations on the operating parameters of a fluidized bed, such as the inlet velocity, density of particles, mass flux, and their mutual interactions, due to the extensive applications of fluidized-beds nowadays in industry [Cheremisinoff and Cheremisinoff, 1984].

The scale-up of the pilot-scale device to the full size and commercial device depends on many factors, which will be discussed in the following chapters. Even with the most conservative approaches, final designs do not always fulfill the expectations. This is because, although the hydrodynamics of these systems have been well

studied, unified equations and models to describe the bubble formation and particle interactions have not yet been developed. Without a real knowledge of the fluidization process, it is not possible to design an optimized fluidized bed. This requires the investigation of the fluidization process in depth by considering fundamentals of mass transfer, momentum transfer, heat transfer and chemical reaction [Cheremisinoff and Cheremisinoff, 1984].

With the improved computational power and algorithms, it is possible to model fluidized beds in pilot size and also industrial size as well [Staněk, 1994].

The literature review, to be discussed in next chapter, revealed that factors, such as carrier phase properties, particles size ratio and density ratio, and operating conditions of the bed are significant factors of the fluidization and separation processes.

The objective of this thesis is to employ computational fluid dynamics (CFD) techniques to produce a validated and grid-converged numerical model for fluidization and segregation processes and analyze the effect of bed operating parameters on the quality of the mixture. A literature review on experimental and numerical works on gas-solid fluidization and utilization of fluidized beds is presented in Chapter 2. Principles of gas-solid fluidized beds, classification of particles and fluidization regimes, physical approaches and governing equations of the fluidized beds, principles of mixing and segregation of particles and available methods of assessing the quality of mixtures are discussed in Chapter 3. Numerical algorithms and the software, materials, model setup and the methodology are discussed in details in Chapter 4. Results of the simulation of fluidization process and analysis of the results are presented in Chapter 5. Chapter 6 is dedicated to the simulation of the segregation process, and results of simulations are discussed and analyzed. Finally, conclusions and recommendations are given in Chapter 7.

Chapter 2

Review of fluidization and segregation processes

2.1 Literature review

The first large-scale, industrial fluidized bed was designed for coal gasification by Fritz Winkler and patented in 1922 (D.R.P. 437,970). Fluidized beds are widely used in industrial applications due to their unique and unusual but useful, behavior. The advantages of fluidized beds can be summarized as below [Kunii and Levenspiel, 1997]:

- Ease of operating control in continuous processes due to the smooth and fluid like flow of particles.
- Rapid preparation of a homogeneous mixture or of a segregated mixture of particles due to their density or size ratio.
- High rates of gas - solid mass and heat transfer, compared to other contacting

methods.

Mixing of fine powders, segregation of particles, heat exchange and gasification of powders, drying, coating, agglomeration and sizing of particles, and many other processes can be named as industrial applications of fluidized beds which benefit from the advantages of the fluidization process. However, their complex hydrodynamics can lead to the faulty design of a fluidization process. Formation of big bubbles or slug flows are some of the issues that can affect the performance of the fluidized bed. [Kunii and Levenspiel, 1997]

The high rate of heat transfer and sensitivity of mixture to density and size ratio in fluidized beds can have significant desirable effects on the separation of bitumen pellets from clay in mechanical processing of oil sands.

2.1.1 Fluidization

Fluidization refers to transforming fine solid particles, that are initially at rest in a cylinder, to a fluid state using an upward flow [Kunii and Levenspiel, 1997]. The hydrodynamics of fluidized beds at minimum fluidization conditions and equations of minimum fluidization velocity and pressure drop in bed were studied and developed by Ergun [1952]. The physics and regimes of the fluidized beds are described in Chapter 3.

Geldart [1973] and Geldart and Abrahamsen [1978] classified particles into four major groups (A, B, C and D) based on their behavior, when they are suspended in gas, to study the fluidization process. Kunii and Levenspiel [1997] classified fluidization regimes in fluidized beds into packed bed, bubbling fluidized bed or spouted fluidized bed, and circulating fluidized bed regimes which contain turbulent fluidized, fast fluidized, and pneumatic transport sub-regimes. These experimental classifica-

tions will help identify the flow regime applicable to the present study, which is essential to the selection of the numerical approach, as will be described next.

There are two main approaches to multiphase flow analysis and simulation of fluidization process, namely the Eulerian - Eulerian approach, which is also known as two-fluid model (TFM), and the Eulerian - Lagrangian approach, also known as discrete element method (CFD-DEM). The Eulerian - Eulerian approach was used to analyze the hydrodynamics of large-scale fluidized bed by many researchers. In this method [Crowe et al., 2011], the solid phase is treated as a continuous phase with equivalent properties of a fluid. Empirical and semi-empirical models have been developed to describe the equivalent dispersed phase properties. In the constant viscosity model, the solid phase viscosity is assumed to be a constant and the solid phase pressure is considered to be only a function of the local solid porosity and viscosity. The kinetic theory of dense gasses later was developed to model the properties of the solid phase in the Eulerian approach. Equations of granular temperature, solid pressure and viscosity, and particles drag model in particles cloud were developed and reviewed by Gidaspow [2012]. The hydrodynamics of fluidized beds have been widely studied and analyzed using the Eulerian - Eulerian approach in computational fluid dynamics method by many researchers [Gidaspow, 2012].

Van der Hoef et al. [2006] reviewed the developments on multiscale modeling of gas-solid fluidized beds at that time. This report covered Eulerian - Eulerian and Eulerian - Lagrangian approaches. The result of TFM simulations might be grid independent, if the size of the grid is on the order of few particle diameters (≈ 10). As the Eulerian approach requires a fine grid to produce accurate results, time steps of the order of 10^{-5} s should be used in a simulation, which is not feasible for simulation of commercial size fluidized bed. To overcome this problem, commercial scale fluidized beds are simulated over coarse spatial grids. In these coarse grids,

small-scale spatial structures are not resolved. The effect of these small-scale spatial structures are added to the system by modification of the closure equations. A proper method of modification of the closure problems is still an open topic in research [Van der Hoef et al., 2006].

A review of the developments of multiscale CFD of modeling gas-solid circulating fluidized bed (CFB) modeling by Wang et al. [2010] shows that, although the Eulerian - Eulerian approach might reach grid independent solution with conventional drag models in periodic domains, the drag force is overestimated and it fails to predict the S-shape of the axial voidage profile [Wang et al., 2010].

Mortier et al. [2011] reviewed the research works on granules drying application of fluidized beds. The authors reviewed both TFM and Lagrangian approaches in CFD modeling of fluidized beds. Using the TFM approach, physical characteristics of the dispersed phase, such as size and shape, are included through empirical relations and particles are not modeled as distinct particles. Comparing results of numerical studies and experimental works, the Lagrangian approach results are in better agreement with experimental data [Chiesa et al., 2005, Mortier et al., 2011].

Singh et al. [2013] reviewed the CFD modeling of combustion and gasification of fuels in fluidized beds. Simulation of gasification and combustion in commercial fluidized beds is still an open topic of research. The TFM approach is not suitable for simulation of fluidized bed with particle size variation unless extensive approximations are chosen. In addition in thermo-chemical reactions there is no appropriate model to describe the mechanism of reactions in commercial fluidized beds using the Eulerian approach. The Eulerian - Lagrangian approach seems to predict better results in thermo-chemical reactions. However, this approach is computationally expensive compared to TFM method, which makes it not to be suitable for commercial size fluidized beds [Singh et al., 2013].

Azimi [2014] reviewed the research works on coal separation in Air Dense Medium Fluidized Beds (ADMFB). Comparing results of simulations and experimental work for separation of coal and sand, poor results were achieved in most preliminary 2D simulations due to the inaccuracy and incapability of Eulerian - Eulerian approach in predicting interactions in the transient regime, at the stage of developing bubbles. However, the predictability of the model was significantly improved by modification of the drag model, coefficient of restitution and using a 3D domain in the simulation [Azimi, 2014].

Zhong et al. [2016] published a comprehensive review of the developments in the CFD simulation of fluidized beds and dense particulate systems using Eulerian - Eulerian approach. Particle size changes, shrinkage or agglomeration, are not addressed adequately in Eulerian - Eulerian approach, and sub-models are required to be developed in this approach [Zhong et al., 2016].

A review of the significant applications and advances in discrete particle simulation of particulate systems was done by Zhu et al. [2008]. The report covers particle packing, particle flow, and particle-fluid flows. The theoretical developments in discrete particle simulation of particular systems are addressed in another article by Zhu et al. [2007]. This review covers research works and developments on modeling particle-particle and particle-fluid interactions and coupling discrete element method with CFD in particle-fluid flows. The simulation of local average method of the gas phase coupled with the discrete element method (DEM) simulation of the solid phase can describe the characteristics of particle-fluid flows without any general assumption. This method produces results which can be used for a better understanding of granular materials and particulate systems and it could be used to study the micro-properties of granular materials to test continuum approaches in granular materials [Zhu et al., 2007].

The performance of particulate systems and multiphase processes mostly falls under 60% of the designed capacity, despite their wide industrial application [Zhu et al., 2008]. Many of multiphase processes are operated as "black box" reactors. This is mainly due to the complex dynamics of particles interactions. The bulk behavior of a reactor depends on the collective outcome of particles interactions. The DEM approach can reveal the underlying fundamentals of particulate system, that make it suitable for detailed studies of such systems [Zhu et al., 2008].

The DEM approach was first proposed by Cundall and Strack [1979] for geomechanics research to describe the behavior of assemblies of discs and spheres. The DEM was later coupled to the CFD to model a two-dimensional fluidized bed by Tsuji et al. [1993]. In this method, the discrete phase is modeled by using the DEM approach, that is based on Newton's laws of motion, and the carrier phase is modeled by the locally averaged variables method, first introduced by Anderson and Jackson [1967]. Due to the high demand of computational power by the DEM approach, progress in this area has been slow in the past. With the currently available computational power, the coupled CFD and DEM has been used in many pieces of research to describe the particle-fluid flow [Zhu et al., 2008].

Zhou et al. [2010] assessed and verified available formulations of momentum equation sets for the particle phase and fluid phase, namely set I, set II and set III, which will be reviewed in Chapter 3. Comparing results of simulations for different particulate systems, they recommended set II, and set I for future work in CFD-DEM simulation of particulate systems. However, the third set of equations conditionally can be used when the fluid flow is steady and uniform or the residual force acting on particles is zero [Zhou et al., 2010].

Xu and Yu [1997] studied the hydrodynamics of fluidized bed by using a coupled CFD and DEM approach. Plots of bed pressure drop versus superficial inlet velocity

were created for both increasing and decreasing inlet velocity cases. Results are in good agreement with measured pressure drop values from experimental works and the same trends were observed.

Goldschmidt et al. [2004] compared simulation results from DEM using a hard sphere approach simulation results and TFM simulation results with experimental results of a fluidized bed. They showed that the DEM approach results were in better agreement with experimental results compared to TFM approach. Complex structures such as formation of small bubbles near the bottom of the bed and strings of particles within larger bubbles were captured using the DEM approach. Comparing results of both CFD models, the kinetic theory of granular flow was capable of giving a meaningful estimate of particles' fluctuating velocities. However, regarding bed expansion dynamics, their simulations results did not follow their experiments. The deviation is mainly due to the formation of densely packed regions in which particles movements approach zero. CFD models were not able to capture these regions. Using the hard sphere discrete particle method, it is not possible to model the long-term particle contacts and multi-particle interactions. Also in TFM approach, when kinetic theory of granular flows is used for closure problems, these contacts are neglected [Goldschmidt et al., 2004].

Müller et al. [2009] validated results of DEM simulations of a fluidized bed against experimental data extracted by magnetic resonance measurements technique. They showed that simulation results are insensitive to the value of restitution coefficient and coefficient of friction, as long as particle-particle and particle-wall collisions energies are dissipated by some routes in the simulations [Müller et al., 2009].

Goniva et al. [2012] studied the influence of rolling friction on a single spout fluidized bed. An open source code was developed based on their work, CFDEM®coupling [Goniva et al., 2012], which couples the CFD solver, OpenFOAM [Weller et al., 1998],

with DEM solver, LIGGGHTS [Kloss et al., 2012] (based on LAMMPS [Plimpton, 1995]). By applying a rolling frictional model, the angle of the response of a granular material can be predicted more accurately. In a 2D spouted fluidized bed, the rolling friction can play a significant role in the results of simulations, especially in regions close to the side walls. The wall effect increases by increasing the rolling coefficient. The particle velocity is affected by the wall at the regions close to wall [Goniva et al., 2012].

Deb and Tafti [2012] used DEM coupled with their in-house developed CFD code, GenIDLEST, to simulate a 2D fluidized bed with a single jet at the inlet. Later, they extended the work to model the fluidized bed with multiple jets at the inlet. Results of numerical simulations are in good agreement with their experimental work in the region close to the distributor plate. However, the code was not able to capture three-dimensional structures at the free surface of the bed which resulted in deviation of simulation results and experimental work results [Deb and Tafti, 2012].

He et al. [2009] studied the hydrodynamics of fluidized beds by comparing results of DEM simulations of a 3D fluidized bed with experiments using PIV technique. They showed that the superficial inlet velocity had a significant effect on the vertical solid velocity and the extent of solids downflow. Also comparing results of the mean time averaged vertical solid velocity, they confirmed, that for averaging periods longer than 12.5 s, the results of the mean and RMS velocity changes with changing/increasing the averaging period slightly [He et al., 2009].

Traoré et al. [2014] simulated 2.7 millions of particles for 1 s on a cluster with 246 Opteron processors. Evolution of a single bubble from its formation until its explosion at the bed surface, the formation of "worm-like-shaped" structures as displayed by Tsuji et al. [2008], and occurrence of the bubbly regime were simulated using an efficient 4-way coupling CFD-DEM approach [Traoré et al., 2014].

2.1.2 Mixing and segregation

In bubbling fluidized bed, if solid particles with different physical properties, such as density, diameter, shape, are simultaneously fluidized, their different fluidization behavior leads to inhomogeneity of solid composition along the bed height. Particles which are accumulated at the bottom of the bed are referred to jetsam, while the other component, that occupies the top portion of the bed, is referred to flotsam [Rowe et al., 1972].

Mixing and segregation of particles have been studied by many researchers in experiments [Palappan and Sai, 2008a,b, Rao et al., 2011], analytical approaches [Daw and Frazier, 1988, Di Maio et al., 2013, Gibilaro and Rowe, 1974], and numerical studies [Di Renzo et al., 2008, Huilin et al., 2007]. Gibilaro and Rowe [1974] used simplified partial differential equations to model analytically a segregating gas fluidized bed. Based on their proposed models, four physical mechanisms exist in segregation of particles in a fluidized bed, namely overall particle circulation, an interchange between wake and bulk phases, axial spreading and a relative segregating flow rate. The model was successful in predicting the equilibrium segregation profiles in a gas fluidized bed for three segregation patterns, namely strongly segregating systems, perfect mixing, and intermediate case [Gibilaro and Rowe, 1974].

On another attempt Daw and Frazier [1988] studied the segregation of large particles ($d \sim 3$ mm) in gas fluidized bed and correlated the mixing index, which will be explained in Section 3.6.3, to particles size ratio, density ratio, static height of the bed, and the superficial inlet velocity. However, correlations for small particles and different geometries of fluidized beds were not covered in their report [Daw and Frazier, 1988].

Rao et al. [2011] reviewed the investigations on segregation of a binary mixture of

particles comprehensively. A new classification scheme for the minimum fluidization velocity ratio, pressure drop profiles, and segregation behavior of binary fluidized mixtures was proposed by comparison of published data and experiments. This classification is based on particles size and density ratio and consists of seven mixture types [Rao et al., 2011].

The experimental values and models, as described before, can be applied to validate the numerical works. CFD has been used by many researchers to study hydrodynamics of mixing and segregation of particles in fluidized beds numerically [Bokkers et al., 2004, Di Renzo et al., 2008, 2012, Feng and Yu, 2004, 2007, 2009, Huilin et al., 2007, Luo et al., 2015, Moon et al., 2007, Rhodes et al., 2001, Wang et al., 2015].

In 2004, Feng and Yu [2004] used a DEM approach to model segregation and mixing of particles in a fluidized bed. Two models are introduced in the literature for momentum conservation equations by using the available models for treatment of the pressure drop term, coupling schemes, and particle-fluid interaction forces, namely Model A and Model B. Due to the differences in the formulation of these two models, the accuracy of each model is still an open topic. A significant difference was observed between Model A and Model B in comparison of simulation results with experiment results. Verification of results against experiments, comparison of pressure drop and concentration of mixture components in height, showed that the Model B is favorable in the formulation of CFD-DEM modeling of fluidized bed [Feng and Yu, 2004]. In another study by Feng et al. [2004], they showed that the stable state of mixing and segregation of particles is strongly affected by the gas velocity. Later, Feng and Yu [2007] showed that the maximum degree of segregation of particles can be achieved at a specified gas velocity for a binary mixture of particles. They suggested that both particle-particle and particle-fluid forces play a significant

role in the separation and mixing of particles. These forces vary both spatially and temporally, which makes their behavior complicated. In another work, Feng and Yu [2009] showed that in a bi-sized mixture of particles the density ratio of the jetsam and flotsam is the dominant parameter that controls the degree of mixing of particles.

Bokkers et al. [2004] studied the mixing of particles of same size and density in a fluidized bed, which are marked by color difference only. They examined the effect of drag model on the formation of bubbles and degree of mixing and compared the results with experimental results. They showed that the Koch and Hill [Hill et al., 2001a] drag model predicted better results than the Ergun [Ergun, 1952] equation combined with Wen and Yu closures [Wen and Yu, 2013]. Besides, they showed that soft sphere and hard sphere models predict the same bubble size and shape.

Luo et al. [2015] studied mixing of particles of same size and density in a fluidized bed using the DEM approach. The CFD-DEM approach was successful in predicting the solid circulation pattern and formation of bubbles. The superficial inlet gas velocity has affects the bubble size that controls the rate of solid mixing.

Moon et al. [2007] used an equation-free coarse-grained approach to accelerate the simulation of segregation process. The method was able to speed up the simulation by a factor of two to ten. This method can be used to describe the stable state of the bed.

Di Renzo et al. [2012] compared results of experiments with CFD-DEM simulations of segregation of particles in a fluidized bed and proposed a model to predict the flotsam component in a binary mixture at equilibrium state. However, the model is not capable of describing the mixing degree at the macroscopically stable state of the bed.

Wang et al. [2015] implemented a hybrid TFM-DEM approach to analyze the segregation of particles in a fluidized bed. The dense solid phase and continuous

carrier phase were modeled by TFM approach, while the dilute solid phase was simulated by DEM approach. Results of simulation were validated against experiments. They showed that the model is capable of producing similar results as those of experiments. The particle size strongly affects the quality of mixture and segregation of particles. Particles' mean height was used to analyze the kinetics of segregation process. The drag force from the gas phase and continuum solid phase influences the particles behavior. The segregation of particles is controlled by the summation of upward drag forces, which is larger than the gravity force on flotsam particles [Wang et al., 2015].

Rhodes et al. [2001] studied numerically the mixing of particles of same size and density in a fluidized bed. They used the Lacey mixing index to quantify the quality of the mixture. The Lacey mixing index was developed based on statistical analysis of the mixture and it compares the quality of the achieved mixture with the quality of a completely random mixture. Standard deviation of the volume fraction of mixture components at different locations of the bed is used in this comparison. Samples at different locations of the bed are required to estimate the standard deviation of the volume fraction of mixture components. The DEM approach enables sampling of the bed without disturbing the mixture. Also, it is possible to change the sample size at each time step. In experimental works, sampling methods suffer from a transition of fluidized bed state to fixed bed state. This transition can be avoided in the DEM approach. They used rectangular boxes to obtain samples. The widths of these boxes were fixed, and their heights were set according to the number of particles in each sample box. This method helps to set the level of scrutiny in the estimation of the mixing index [Rhodes et al., 2001].

2.2 Statement of the problem

Considering the increasing demand for low-cost energy and environmental issues with current oil extraction methods, an economic and green method of oil extraction should be developed. The mechanical process of tar sands, as described in Chapter 1, may overcome environmental and economic issues related to current processes of oil extraction. The separation of bitumen and clay in the fluidized bed is a key point for an efficient method. Although there have been extensive studies on fluidized beds, valuable information about the hydrodynamics of separation and effect of operating parameters on the quality of the mixture is not available. It is vital to analyze the impact of significant factors on the process to design the fluidized bed at optimum condition. With the available computational power nowadays, it is possible to simulate the process using the DEM approach. The DEM approach can increase the accuracy of the results. As it was mentioned in the literature survey, many researchers up to now have studied the feasibility of implementation of DEM approach in CFD modeling of fluidized beds. However, the effect of parameters on the accuracy of results have not been addressed, and there is no general rule to model the fluidized bed using the DEM approach. It is necessary to study the effect of parameters on the simulation results to create an accurate numerical model. Later, the numerical model will be used to examine the effect of design parameters and operating parameters of the bed on mixing and segregation of particles in the fluidized bed.

2.3 Objectives of the study

Following the discussion of the need for producing a numerical model for fluidized beds, the objective of this research work is to analyze the effect of significant factors of a numerical model, such as grid size, boundary conditions, drag coefficient model and momentum exchange models on simulation results. Then, the numerical model will be used to study the segregation process in a fluidized bed, and analyze the effect of design and operating parameters of a fluidized bed, such as superficial inlet velocity, particles' density ratio, the physical properties of the carrier phase and the bed size, on the fluidization and segregation process.

2.4 Scope of the study

One of the significant factors in numerical methods is the size of the grid. The accuracy of the simulation results using different size of grids is investigated to find the optimum grid size on which results of simulations are independent of the grid size. The grid size analysis is based on the fluidization process and the pressure drop in the bed, as a characteristic quantity, is estimated for this purpose.

In gas-solid fluidized beds, the drag force is a dominant factor. The application of different drag models could introduce errors on bed expansion, pressure drop and particles concentration. In the current work, available drag models are examined and evaluated to obtain an accurate numerical model.

As it was discussed in the literature review, the DEM is a computationally expensive method. In most of the simulations a slice of the bed is considered as the simulation domain to reduce the required computational power and time. This assumption affects the results of simulations. The effect of a sliced domain is studied

and verified so that a true representation of the 3D fluidized bed is achieved.

The momentum exchange term in the simulation of gas-solid flow is the key point in the coupling of phases. The effect of the momentum exchange term on the hydrodynamics of fluidization process is considered using available models, Model A and Model B [Gidaspow, 2012]. The effect of models on the hydrodynamics of the fluidization process is examined by comparing the calculated pressure drop with the value of analytical and empirical solutions.

Further investigations are performed on the segregation of a binary mixture of spherical particles. At the first step a binary mixture of sand and bitumen at -50℃ with a density ratio of 2.5 is fluidized to be segregated. The effect of front and back planes is studied, and results are compared with a 3D case. The momentum exchange model is investigated, and results are compared with literature.

The results of the fluidization process and segregation of particles with density ratio of 2.5 are used to produce a numerical model for segregation of particles with a smaller density ratio. The numerical model is used to examine the effect of the carrier phase and the bed aspect ratio on the rate of segregation and the stable state of this mixture.

Chapter 3

The physics of the problem

3.1 Principles of gas-solid fluidization

Fluidization refers to transforming fine solid particles, that are initially at rest in a cylinder, to a fluid state using an upward flow. The total pressure loss of the fluid throughout the bed increases by increasing the superficial inlet velocity from zero. The pressure drop increases because frictional resistance increases. By further increase of the gas velocity, particles start to vibrate. At this stage, the weight of particles is counterbalanced by the frictional force between particles and the fluid and the pressure drop in the flow field at each height is equal to the overhead weight of fluid and particles. This state is called minimum fluidization state where particles are lifted in the flow and are supported by the flow field [Kunii and Levenspiel, 1969].

The dense-phase of particles, when it is fluidized by gas, looks like a boiling liquid. This fluidized dense phase has some unusual but useful properties of the system. Some of the behaviors of a solid-gas fluidized bed can be described as follows [Kunii and Levenspiel, 1969]:

- Light objects float on it, while heavy ones sink;
- The free surface of a fluidized bed remains horizontal even if the cylinder is tilted;
- Inter-connected cylinders share the same height by transfer of particles;
- Particles leave the cylinder if there is a hole on the side of it, and;
- The pressure difference between two points can be related to the static head.

3.2 Determination of minimum fluidization velocity

3.2.1 Experimental and empirical methods

Minimum fluidization condition of a bed can be obtained by monitoring the pressure drop while increasing the inlet velocity. Figure 3.1 presents pressure drop ($\triangle p$) versus the inlet velocity (U). The pressure drop in the bed proportionally increases as the inlet velocity increases. The pressure drop increases from zero at the static condition of the bed to the maximum pressure drop at minimum fluidization condition. At this point, the bed expands, and the drag force on particles equalizes the gravitational force on them. By further increasing the inlet velocity the bed suddenly unlocks, and the pressure drop falls slightly. This peak is mostly a result of inter-particles frictional force. After this stage, the bed expands and bubbles are formed in the bed, and the pressure drop remains practically unchanged in the bed even if the inlet velocity increases. A slight increase of the pressure drop is observed by further

increasing the inlet velocity, that is mostly as a result of the increase in wall-fluid friction force.

It can be noticed in Figure 3.1 that the pressure drop does not follow the same pattern at the minimum fluidization condition when decreasing the inlet velocity. In this figure, W is the weight of the bed and A is the cross-sectional area of the bed.

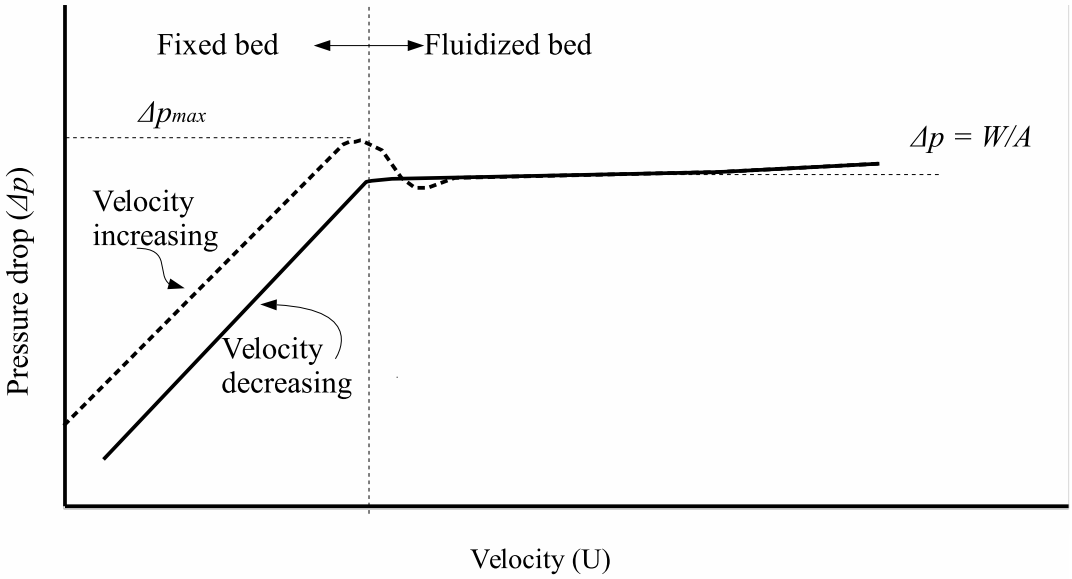

Figure 3.1: Pressure drop in a bed versus fluid velocity. Adapted from [Kunii and Levenspiel, 1969]

3.2.2 Theoretical method

Particles are supported by the flow field in the fluidization process. This means that the gravitational forces of particles are balanced by the drag force acting on particles due to the flow. Thus, the pressure drop in the bed can be quantified as below:

$$\triangle pA = H(1-\epsilon_g)(\rho_s - \rho_g)g \tag{3.1}$$

Where $\triangle p$ is the pressure drop, A is the cross-sectional area of the bed, H is the bed height, ϵ_g is the bed porosity, and ρ_s and ρ_g are the solid density and fluid density, respectively.

Ergun [1952] suggested that the pressure drop in a bed can be estimated as below:

$$\frac{\triangle p}{\triangle L} = 150\frac{(1-\epsilon_g)^2\mu_g U}{\epsilon_g^3 d_s^2} + 1.75\frac{(1-\epsilon_g)\rho_g U^2}{\epsilon_g^3 d_s} \tag{3.2}$$

In this equation μ_g is the gas viscosity and d_s is the diameter of the particle.

Kunii and Levenspiel [1969] replaced the minimum fluidization condition parameters in the Ergun equation and derived Equation 3.3 for minimum fluidization condition:

$$\frac{1.75}{\phi_s \epsilon_{g,mf}^3}\mathrm{Re}_{mf}^2 + \frac{150(1-\epsilon_{g,mf})}{\phi_s^2 \epsilon_{g,mf}^3}\mathrm{Re}_{mf} = \frac{d_s^3 \rho_g(\rho_s - \rho_g)g}{\mu_g^2} \tag{3.3}$$

$$\mathrm{Re}_{mf} = \frac{d_s U_{mf}\rho_g}{\mu_g} \tag{3.4}$$

where subscript mf refers to minimum fluidization condition, and ϕ_s is the sphericity of the particle which is defined as below:

$$\phi_s = \left(\frac{\text{surface of sphere}}{\text{surface of particle}} \right) \text{both of same volume} \tag{3.5}$$

3.3 Solid particles classification

There are many factors affecting the solids behaviour in a fluidized bed, of which the most important are:

1. Carrier phase density, ρ_g, and viscosity, μ_g;
2. Solid phase density, ρ_s;
3. Mean diameter of the particles, $\overline{d}_p$, and;
4. Particle shape, ϕ_s.

Figure 3.2 shows the classification of solid powders behavior (fluidized by gas) based on the mean particles diameter and solid-gas density difference, which can be described as follows [Geldart, 1973]:

1. Group A, aeratable particles

   When a packed bed is formed by particles of group A, the bed expands, and bubbles are formed later. Solids of the category are mixed vigorously.

2. Group B, sand-like particles

   In a bed formed by particles of group B, large bubbles grow in the bed. The size of these bubbles is controlled by the internal forces in the bed.

3. Group C, cohesive particles

   Particles of this group are mostly hard to be fluidized due to high inter-particle forces.

4. Group D, heavy particles

   Fluidized beds formed of this type of particles are liable to spout and formation of large bubbles.

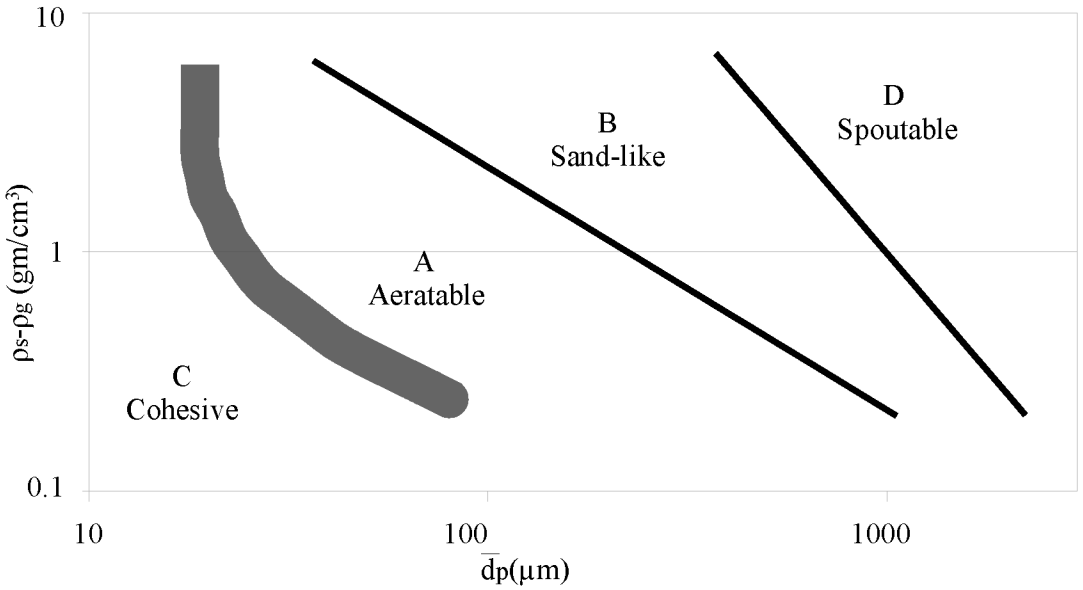

Figure 3.2: Geldart powder classification. Adapted from [Geldart, 1973].

3.4 Fluidization regimes

Fluidization happens in a fixed bed when the inlet velocity increases from zero to the minimum fluidization velocity. Further increase of the inlet velocity changes the flu-

idized bed behavior into bubbling or spout fluidized bed, later to turbulent fluidized bed and finally to pneumatic conveying of particles. Various attempts have been made to plot this behavior and plot flow regimes for gas-solid suspensions. A brief description of the regimes is as follows [Bi and Grace, 1995, Kunii and Levenspiel, 1997]:

- Fixed bed

  The superficial inlet velocity is less than the minimum fluidization condition. Particles are motionless, and the fluid percolates through the void space between particles. At minimum fluidization condition, the pressure drop across the bed equals the weight per unit area of particles and the bed height start to increase.

- Particulate fluidization

  The bed may continue expanding by increasing the superficial inlet velocity. This type of fluidization is also known as homogenous fluidization and mostly occurs in liquid fluidization beds.

- Aggressive fluidization

  This type of fluidization is also known as aggregative or heterogeneous or bubbling fluidization. Bubbling, slugging flow, and turbulent fluidized bed are under this category. Two separate solid phases are made up in this regime, namely dense phase and the discontinuous phase.

- Fast fluidization and pneumatic conveying regimes

  Increasing the fluid velocity, the bed turns to fast fluidization and pneumatic conveying regimes. In a fast fluidization bed, a dilute region exists with the

dense phase. Particles are carried by the fluid in the center and form the dilute region while the dense regions are formed on the walls of the bed. Increasing the inlet velocity, pneumatic conveying of particles starts, which can be distinguished from the fast fluidization regime as the dense regions disappear, replaced by a vertically uniform distribution of particles.

Figure 3.3 presents the model developed to describe the flow behavior based on the particles size, density, sphericity, and fluid phase density and viscosity [Kunii and Levenspiel, 1997]. This map of fluidization regimes will be useful to classify the type of flow behavior of the simulations in this study.

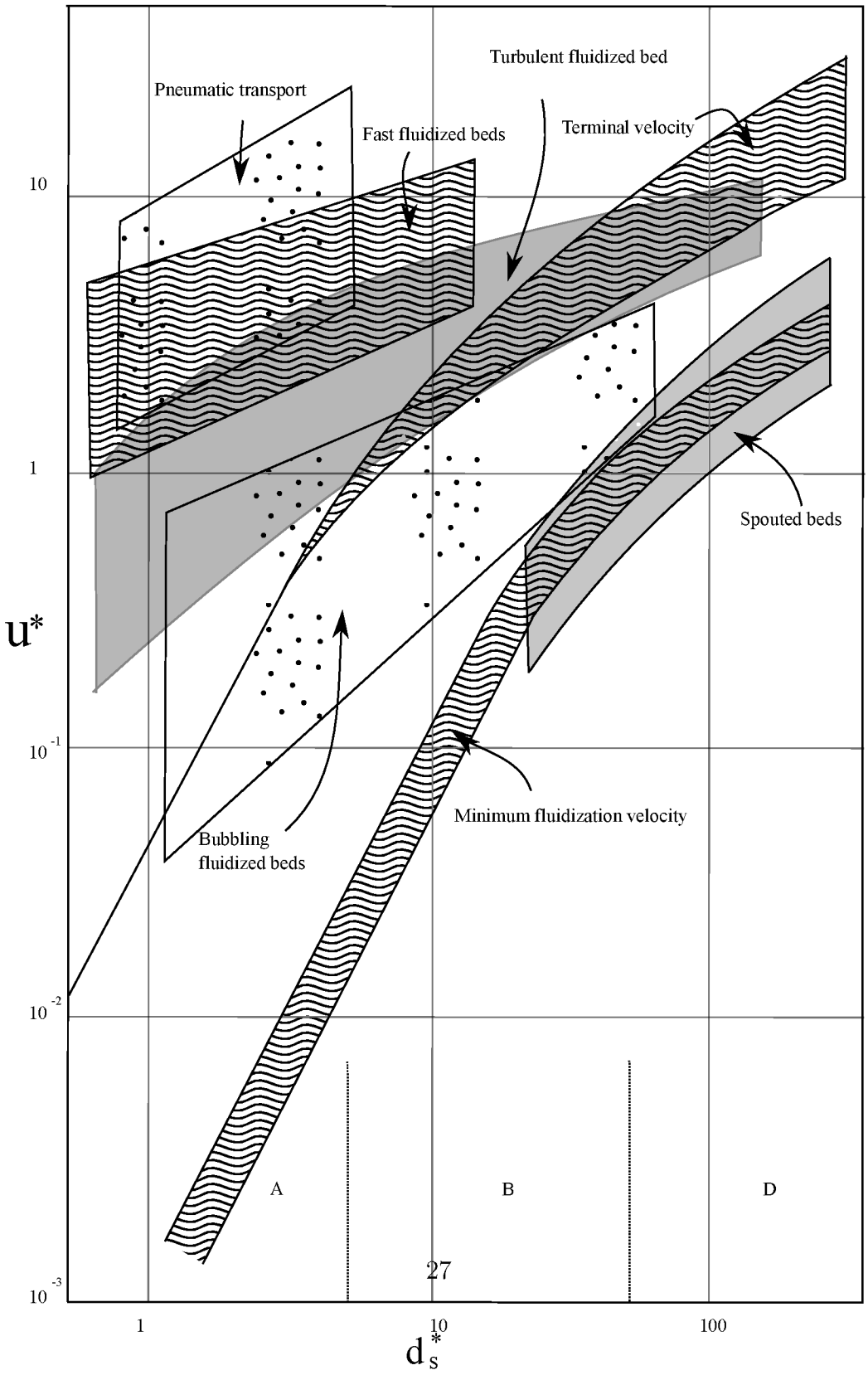

Figure 3.3: Fluidization regimes map. Adapted from [Kunii and Levenspiel, 1997]

Where

$$d_s^* = d_s \left[\frac{\rho_g(\rho_s - \rho_g)g}{\mu_g^2} \right]^{1/3} \tag{3.6}$$

$$u^* = u \left[\frac{\rho_g^2}{\mu_g(\rho_s - \rho_g)g} \right]^{1/3} \tag{3.7}$$

and g is the gravity.

3.5 Multiphase modelling approaches

There are two main approaches to model the mixture behavior. One considers the dispersed phase as a continuous phase and derives the equations based on a fluid characteristic. This approach is called the Eulerian perspective and requires empirical equations to model the behavior of the dispersed phase. On the other hand, the Lagrangian perspective considers every single particle and derives the equations of motions of the particles based on mass and velocity of the particles using Newton's laws of motion. The carrier phase in both approaches is treated as a continuous phase, and locally averaged variables are utilized in the governing equations of the carrier phase [Crowe et al., 2011].

3.5.1 Carrier phase governing equations

The carrier phase in Eulerian - Eulerian and Eulerian - Lagrangian approach is treated as a continuous phase and equations of conservation of mass, momentum, and energy for this phase are solved to model the carrier phase. A review of the

governing equations from the multiphase flows textbook by Crowe et al. [2011] is presented here.

Continuity equation

According to the conservation of mass, summation of the rate of mass accumulation and the net out-flux of mass should be zero.

Assuming there is no mass transfer and the fluid is incompressible the continuity equation can be written in differential form for a multidimensional flow as below:

$$\frac{\partial}{\partial t}(\epsilon_g \rho_g) + \nabla \cdot (\epsilon_g \rho_g \mathbf{u}) = 0 \tag{3.8}$$

Where $\mathbf{u}$ is the gas velocity.

Momentum equations

The conservation of momentum can be expressed as the summation of the rate of change of momentum in the control volume and net out-flux of momentum from the control volume, which is equal to the force on the fluid in the control volume.

For multidimensional flows, assuming there is no mass transfer, the momentum equations can be rewritten in the following form:

$$\frac{\partial}{\partial t}(\epsilon_g \rho_g \mathbf{u}) + \nabla \cdot (\epsilon_g \rho_g \mathbf{u}\mathbf{u}) = -\epsilon_g \nabla p_g + \nabla T_g + \epsilon_g \rho_g \mathbf{g} + \beta(\mathbf{v} - \mathbf{u}) \tag{3.9}$$

In this equation β is the fluid-particle friction coefficient, $\mathbf{v}$ is the solid velocity and the gas phase stress tensor, T_g, can be represented as:

$$T_g = 2\epsilon_g \mu_g \tau_g \tag{3.10}$$

Where τ_g represents the shear stress tensor that can be evaluated using the common methods for a single phase flow:

$$\tau_g = \frac{1}{2}\left(\nabla\cdot \mathbf{u} + (\nabla\cdot \mathbf{u})^T\right) - \frac{1}{3}(\nabla\cdot \mathbf{u})I \tag{3.11}$$

Turbulence models can be used to calculate the effective viscosity. A description of common turbulence modeling approaches can be found in a book by Wilcox et al. [1998].

3.5.2 Dispersed phase governing equations

Eulerian approach

The Eulerian - Eulerian approach, which can be called as the two-fluid model (TFM), treats the dispersed phase as a continuous phase. The conservation equations of mass, momentum, and energy of a fluid are solved to model the behavior of the phase. Equivalent properties of a fluid, such as viscosity or density, should be defined to solve the conservation equations.

The continuity equation of the dispersed phase can be derived by summing the conservation equations for individual particles over all particles in the control volume by using the volume fraction of the dispersed phase as below:

$$\frac{\partial}{\partial t}(\epsilon_s \rho_s) + \nabla \cdot (\epsilon_s \rho_s \mathbf{v}) = 0 \tag{3.12}$$

The momentum equation for a cloud of particles can be derived by summing conservation equations for individual particles in the control volume.

$$\frac{\partial(\epsilon_s \rho_s \mathbf{v})}{\partial t} + \nabla \cdot (\epsilon_s \rho_s \mathbf{v}\mathbf{v}) = -\epsilon_s \nabla P_s + \nabla T_s + \epsilon_s \rho_s g - \beta(\mathbf{v} - \mathbf{u}) \tag{3.13}$$

The solid phase stress tensor can be represented as below:

$$T_s = (-P_s + \xi_s \nabla \cdot \mathbf{v})I + 2\mu_s \tau_s \tag{3.14}$$

In this equation P_S is the solid phase pressure, ξ_s is the bulk viscosity, and μ_s represents the shear viscosity. These variables can be defined as functions of the granular temperature as well as the particle restitution coefficient, particle diameter, material density, and particles volume fraction.

The granular temperature, Θ, is based on the kinetic theory of dense gasses, which was first introduced by Bagnold [1954]. Later, Gidaspow [2012] used the granular temperature of the dense flows to describe the particles' velocity fluctuations, C, as below:

$$\Theta = \frac{1}{3}\langle C^2 \rangle \tag{3.15}$$

The conservation equation of the granular temperature is given as below:

$$\frac{3}{2}\left[\frac{\partial}{\partial t}(\epsilon_s \rho_s \Theta) + \nabla \cdot (\epsilon_s \rho_s \mathbf{v} \cdot \Theta)\right] = T_s : \nabla \mathbf{v} + \nabla \cdot \mathbf{v} + \nabla \cdot k \nabla \Theta - \gamma \tag{3.16}$$

where $T_s : \nabla \mathbf{v}$ is the generation of the fluctuation energy due the work of the shear stress in the particle phase, $\nabla \cdot \nabla \Theta$ is the conduction of the fluctuating energy and γ is the dissipation of due to inelastic collisions. For more information about TFM approach and kinetic theory, please refer to Gidaspow [2012].

As there is no need to consider every single particle dynamics in the two-fluid model large systems can be modeled, which is the main advantage of this approach. However, in a particular system with particle size distribution, a new phase should be considered for each particle size or empirical models should be used, which increases the complexity of the problem [Crowe et al., 2011].

Lagrangian approach

Governing equations

In the Eulerian - Lagrangian approach, the carrier phase is treated as a continuous fluid, and the conservation equations are used to model it. Particles in the dispersed phase are tracked individually or as parcels of particles in the flow field. Locally averaged variables are employed in the conservation equations to be solved. Momentum and mass transfer between the phases are permitted in these equations. Two models are proposed in the literature for the momentum equations formulation, namely Model A and B [Gidaspow, 2012]. The Model A assumes that the pressure drop is shared between the gas and solid phase, and the Model B assumes that the pressure

drop is applied to the gas phase only [Feng and Yu, 2004].

The continuity equation can be written as below:

$$\frac{\partial \epsilon_g}{\partial t} + \nabla\cdot(\epsilon_g \mathbf{u}) = 0 \tag{3.17}$$

The set of momentum conservation equations can be written as below:

- Model A

$$\frac{\partial \rho_g \epsilon_g \mathbf{u}}{\partial t} + \nabla\cdot(\rho_g \epsilon_g \mathbf{u}\mathbf{u}) = -\epsilon_g \nabla P - \mathbf{F}^{\mathrm{A}} + \nabla\cdot(\epsilon_g \tau) + \rho_g \epsilon_g \mathbf{g} \tag{3.18}$$

- Model B

$$\frac{\partial \rho_g \epsilon_g \mathbf{u}}{\partial t} + \nabla\cdot(\rho_g \epsilon_g \mathbf{u}\mathbf{u}) = -\nabla P - \mathbf{F}^{\mathrm{B}} + \nabla\cdot(\epsilon_g \tau) + \rho_g \epsilon_g \mathbf{g} \tag{3.19}$$

In these sets of equations, $\mathbf{F}^{\mathrm{A}}$ and $\mathbf{F}^{\mathrm{B}}$ are the volumetric particle - fluid interaction forces for the two models, and they are interchangeable using the following equation:

$$\mathbf{F}^{\mathrm{B}} = \frac{\mathbf{F}^{\mathrm{A}}}{\epsilon_g} - \rho_g \epsilon_s \mathbf{g} \tag{3.20}$$

On the dispersed phase side, the force acting on each particle is the summation of the forces due to the contact force of particles, $\mathbf{f}_{c,ij} + \mathbf{f}_{d,ij}$, the force imposed by the carrier phase, $\mathbf{f}_{p-f,i}$, and the gravity force as below:

$$m_i \frac{d\mathbf{u}_{p,i}}{dt} = \mathbf{f}_{p-f,i} + \sum_{j=1}^{k_i} (\mathbf{f}_{c,ij} + \mathbf{f}_{d,ij}) + \rho_{p,i} V_{p,i} \mathbf{g} \tag{3.21}$$

where $V_{p,i}$ is the volume of the particle i and $\mathbf{f}_{p-f,i}$ is the total particle - fluid interaction force on the particle and is the summation of the drag force, the buoyancy force, lifting force, the virtual mass force, Basset force, and others. $\mathbf{f}_{c,ij}$ and $\mathbf{f}_{d,ij}$ are the contact force and the viscous contact damping forces respectively

The rotational momentum can be written as below:

$$\mathbf{I}_i \frac{d\omega_i}{dt} = \sum_{j=1}^{k_i} \mathbf{T}_{ij} \tag{3.22}$$

$\mathbf{T}_{ij}$ is the torque between particles i and j.

According to the models introduced for momentum equations of the carrier phase, two models can be used to describe the particle - fluid interaction force, namely Model A and B. Considering only the pressure drop and buoyancy terms these models can be written as below:

$$\text{Model A} \quad \mathbf{f}_{p-f,i} = -V_{p,i} \nabla p_i + \mathbf{f}^{\mathrm{A}} \tag{3.23}$$

$$\text{Model B} \quad \mathbf{f}_{p-f,i} = \rho_g V_{p,i} \mathbf{g} + \mathbf{f}^{\mathrm{B}} \tag{3.24}$$

In Model A, the buoyancy force is related to the pressure drop term, ∇p_i, and the other part, $\mathbf{f}^{\mathrm{A}}$, is linked to the fluid drag force multiplied by the fluid volume fraction, $\epsilon_g \mathbf{f}_{drag,i}$. In Model B the buoyancy force is related to the static pressure

drop, ∇p_0, and the fluid drag force. It is good to notice that the total pressure drop, ∇P, consists of three factors in a bed [Feng and Yu, 2004]:

- The hydrostatic pressure drop, ∇p_0, which is due to the gravity force of the gas.
- The hydrodynamic pressure drop, ∇p_d, which is due to the relative motion between the gas and particles.
- The pressure drop due to the friction of the gas and the walls, ∇p_w. This term can be neglected compared to other terms of the total pressure drop.

Equations 3.23 and 3.24 can be rewritten in the following forms:

$$\text{Model A} \quad \mathbf{f}_{p-f,i} = -V_{p,i}\rho_g \mathbf{g} + V_{p,i}\nabla p_{d,i} + \epsilon_g \mathbf{f}_{drag,i} \tag{3.25}$$

$$\text{Model B} \quad \mathbf{f}_{p-f,i} = -V_{p,i}\rho_g \mathbf{g} + \epsilon_s \mathbf{f}_{drag,i} + \epsilon_g \mathbf{f}_{drag,i} \tag{3.26}$$

When forming a uniform bed of mono-sized particles, where there is no acceleration in either phase, the pressure drop is the summation of the static pressure drop, ∇p_0, and the dynamic pressure drop, ∇p_d. In this system, the point-wise values of the pressure drop around each particle, $\nabla p_{d,i}$, are identical and can be replaced with the locally averaged pressure drop value, ∇p_d. The particle volume, $V_{p,i}$, is equal to ϵ_s/n and the relation between the hydrodynamic pressure drop and the particle drag force can be written as below[Feng and Yu, 2004] :

$$\nabla p_d = n f_{drag,i} \tag{3.27}$$

The second term on the right hand side of Equation 3.25 can be written as below:

$$V_{p,i}\nabla p_{d,i} = \frac{\epsilon_s}{n} n f_{drag,i} \tag{3.28}$$

The Model A and B predict the same results for a packed bed of monosized particles. However, this concept is not applicable in the fluidization process, and Model A and B predict different results. This difference is because in Model A a point-wise value of the pressure drop around each particle is needed, $\nabla p_{d,i}$, while just locally averaged pressure drop value can be obtained through the continuum approach. In the fluidization process particles are not uniformly distributed in space and their velocity and trajectories are not the same. The non-uniform particle cloud results in a difference between the locally averaged pressure drop and the point-wise value of the pressure drop around each particle [Feng and Yu, 2004].

Particle - fluid interactions

The coupling of the forces between the dispersed phase and the carrier phase can be derived according to the Newton's third law of motion. The force of the dispersed phase acting on the gas phase should be equal to the force of the gas phase working on the dispersed phase but in the opposite direction. To achieve this relation three schemes are presented in the literature [Feng and Yu, 2004, Gidaspow, 2012]:

- The first scheme calculates the forces from particles to the gas phase by the local average method, and forces from the gas phase to the solid phase are calculated separately according to the individual particle velocity. The conditions of Newton's third law of motion are not guaranteed in this scheme.

- The second scheme calculates forces from particles to the gas phase at local-

average scale as used in scheme one, and then distributes the estimated values between individual particles according to certain averaging rules. For a mono-sized particle system the following relation can be derived according to this scheme:

$$\mathbf{f} = \frac{\mathbf{F}\nabla V}{k_c} \tag{3.29}$$

where k_c is the number of particles in the computational cell, ∇V is the volume of the CV and $\mathbf{F}$ is the volumetric particle-fluid interaction force.

This scheme can satisfy the Newton's third law of motion. However, this method distributes the interaction force between the particles uniformly, and does not consider the different trajectories and velocities of the particles. Besides, it is necessary to use a mean particles' velocities to calculate the interaction force, $\mathbf{F}$. The appropriate method of estimation of the mean particles' velocities is still an open topic.

- Xu and Yu [1997] introduced the third scheme, which calculates the particle - fluid interaction force at each time step on individual particles in a computational cell, and then calculates the summation of these values to produce the particle - fluid interaction force at the cell scale. The following equation can be used for this scheme:

$$\mathbf{F} = \frac{\sum_{i=1}^{k_c} \mathbf{f}}{\nabla V} \tag{3.30}$$

This scheme can overcome problems mentioned for scheme 1 and 2, and is widely used by researchers [Feng and Yu, 2004] .

The effect of particle cloud on the drag coefficient is still an open topic. Numerical methods such as Direct Numerical Simulation (DNS) and Lattice Boltzmann (LB) have been used to quantify the drag force from fluid to a particle in a particle cloud. However, these studies are mostly limited to simple geometries and cases due to their high demand of computational power. Therefore, calculation of the interaction force of the fluid to the particles, $\mathbf{f}$, in the current work is based on the calculation of pressure drop using available models in the literature, namely Model A and B [Feng and Yu, 2004, Gidaspow, 2012].

The hydrodynamic pressure drop is assumed to be shared uniformly between particles in Model A and B. The following models can be derived for each set of momentum equation [Feng and Yu, 2004]:

1. Model A

$$\mathbf{f}^{\mathrm{A}} = \frac{\epsilon_g}{n}\nabla p_d = \frac{\pi}{6} d_i^3 \frac{\epsilon_g}{\epsilon_s}\nabla p_d \tag{3.31}$$

2. Model B

$$\mathbf{f}^{\mathrm{B}} = \frac{\nabla p_d}{n} = \frac{\pi}{6} d_i^3 \frac{1}{\epsilon_s}\nabla p_d \tag{3.32}$$

The drag force is the main interaction force in a gas-solid system. The drag force on an isolated particle in a flow field can be written as below Crowe et al. [2011]:

$$\mathbf{F} = \frac{1}{2}\rho_g C_D A_p |\mathbf{u} - \mathbf{v}|(\mathbf{u} - \mathbf{v}) \tag{3.33}$$

Where C_D is the drag coefficient, and A_p is the area of the particle. The drag factor is the ratio of the drag coefficient to the Stokes drag, which is introduced as:

$$f = \frac{C_D \mathrm{Re}_r}{24} \tag{3.34}$$

and

$$\mathrm{Re}_r = \frac{\rho_g |\mathbf{u} - \mathbf{v}| r}{\mu_g} \tag{3.35}$$

The drag force on an isolated sphere in the flow is a well-known problem. Researchers have developed many models to quantify drag on a sphere [Haider and Levenspiel, 1989, Putnam, 1961, Schiller and Naumann, 1935]. However, there is not enough information on the effect of the particle cloud on the drag coefficient. Numerical and experimental works have been done to study the effect of particle cloud on the drag coefficient. The drag force on particles in a bed formed of multi-sized particles is still and open topic [Feng and Yu, 2004]. However, equations of pressure drop and drag force for monosized systems are used for multi-sized beds as well. Different models are presented in the literature for the drag force of a particle in particle cloud as the friction coefficient as explained next [Crowe et al., 2011, Gidaspow, 2012]:

According to Darcy's law the pressure drop can be related to the friction coefficient, β, as below Gidaspow [2012]:

$$-\epsilon_g \frac{\partial p}{\partial x} - \beta(\mathbf{u} - \mathbf{v}) = 0 \tag{3.36}$$

- Ergun [1952]

  Based on the Ergun equation of pressure drop, Equation 3.2, the friction coefficient can be written as below:

$$\beta = 150\frac{\epsilon_s^2 \mu_g}{\epsilon_g (d\phi_s)^2} + 1.75\frac{\rho_g |\mathbf{u} - \mathbf{v}| \epsilon_s}{\phi_s d} \tag{3.37}$$

- Wen and Yu [1966]

  Wen and Yu [1966] suggested a correction to Richardson and Zaki [1954] equation of the pressure drop, when the porosity is greater than 0.8 and derived the following equation for the friction coefficient:

$$\beta = \frac{3}{4} C_D \frac{\epsilon_g \epsilon_s |\mathbf{u} - \mathbf{v}| \rho_g}{d} f(\epsilon_g) \tag{3.38}$$

  where C_D is the drag coefficient of an isolated particle as below:

$$\begin{aligned} C_D &= \frac{24}{\mathrm{Re}_s}\left(1 + 0.15(\mathrm{Re}_s)^{0.687}\right), \quad \mathrm{Re}_s < 1000 \\ C_D &= 0.44, \quad \mathrm{Re}_s \geq 1000 \end{aligned} \tag{3.39}$$

where Re_s is as follows:

$$\mathrm{Re}_s = \frac{\epsilon_g \rho_g (|\mathbf{u} - \mathbf{v}|) d}{\mu_g} \tag{3.40}$$

and $f(\epsilon_g)$ is a correction for presence of the particle cloud and is given as below:

$$f(\epsilon_g) = \epsilon_g^{3.7} \tag{3.41}$$

- Gidaspow [2012]

  Gidaspow [2012] suggested that the drag model proposed by Ergun [1952], Equation 3.37, is valid for dense flows, when $\epsilon_g < 0.8$, and to use Wen and Yu [1966] drag model, Equation 3.38, for dilute flows, when ϵ_g is greater than 0.8, with a correction as below:

$$f(\epsilon_g) = \epsilon_g^{-2.65} \tag{3.42}$$

- Di Felice [1994]

  Di Felice [1994] found by analysis of published data a correction for $f(\epsilon_g)$ and suggested the following equation:

$$f(\epsilon_g) = \epsilon_g^{-\xi} \tag{3.43}$$

where ξ is the following empirical equation:

$$\xi = 3.7 - 0.65 \exp\left[-\frac{(1.5 - \log(\mathrm{Re}_r))^2}{2}\right], \quad 10^{-2} < \mathrm{Re}_r < 10^4 \tag{3.44}$$

- Koch and Hill [2001]

  Koch and Hill [2001] developed a model for drag coefficient of a particle in particle cloud based on Lattice - Boltzmann method as below:

$$F_0 = \begin{cases} \frac{1+3\sqrt{\epsilon_s/2}+(135/64)\epsilon_s \ln(\epsilon_s)+16.14\epsilon_s}{1+0.681\epsilon_s-8.48\epsilon_s^2+8.16\epsilon_s^3} & , \epsilon_s < 0.4 \\ \frac{10\epsilon_s}{(1-\epsilon_s^3)} & , \epsilon_s > 0.4 \end{cases} \tag{3.45}$$

$$F_3 = 0.0673 + 0.212\epsilon_s + \frac{0.0232}{(1-\epsilon_s)^5} \tag{3.46}$$

$$F = F_0 + \frac{F_3 \mathrm{Re}}{2} \tag{3.47}$$

$$\beta_p = \frac{18\mu_g(1-\epsilon_s)^2\epsilon_s^2 F}{d_s^2} \tag{3.48}$$

$$\mathrm{Re} = \frac{\rho_g \epsilon_s |\mathbf{u} - \mathbf{v}| d_s}{\mu_g} \tag{3.49}$$

$$\mathbf{F}_{p,f} = \frac{V_p \beta_p}{\epsilon_s} (\mathbf{u} - \mathbf{v}) \tag{3.50}$$

Particle - particle interactions

The Hard Sphere Model (HSM) or the Soft Sphere Model (SSM) can be used to model the total particles' interactions forces in Lagrangian approach. An overview of the models is presented below. Further explanation of the models can be found in [Crowe et al., 2011].

1. Hard Sphere Model (HSM)

   HSM is based on the impulsive forces, which are defined by the integral of the forces acting on a particle versus time. In this approach particles are assumed to be rigid without any deformation.

   Three assumptions are made for HSM:

   (a) particle deformation is negligible;

   (b) the friction on sliding particles obeys Coulomb's friction law;

   (c) once a particle stops sliding there is no further sliding.

2. Soft Sphere Model (SSM)

   The soft-sphere model assumes an overlap displacement δ to consider the deformation of the particles as they collide. This displacement distance is shown

in Figure 3.4. A frictional force is resulted when particles collide and are deformed. This force is generated because of the presence of the normal collision force. Particles' tangential and normal forces of the collisions are calculated by using the spring, dashpot and friction slider mechanical elements. Figure 3.5 presents a schematic of these elements. In this model, the relation between pre-collision and post-collision velocities can be obtained. Also, forces acting on particles during the contact period are calculated.

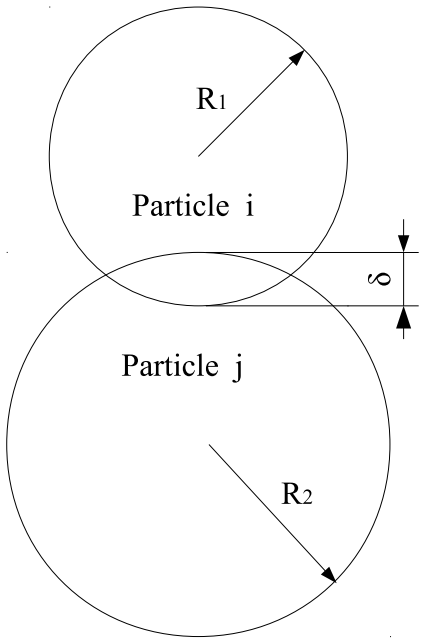

Figure 3.4: Displacement of two particles in contact. Adapted from [Crowe et al., 2011]

Forces acting on particles can be calculated using Equation 3.51 for the normal force and Equation 3.52 for the tangential force.

The normal component of the contact force is the summation of the spring and the dashpot forces:

$$\mathbf{F}_{nij} = (k_n \delta_n - \eta_{nj} \mathbf{G} \cdot \mathbf{n})\mathbf{n} \tag{3.51}$$

And the tangential component of the contact force is the summation of the slider, spring and the dash-pot forces:

$$\mathbf{F}_{tij} = -k_t \delta_t - \eta_{tj} \mathbf{G}_{ct} \tag{3.52}$$

where $\mathbf{G}$ is the relative velocity of the particles and defined as below:

$$\mathbf{G} = \mathbf{v}_i - \mathbf{v}_j \tag{3.53}$$

and $\mathbf{G}_{ct}$ is the slip velocity at the contact point, which is given by:

$$\mathbf{G}_{ct} = \mathbf{G} - (\mathbf{G} \cdot \mathbf{n})\mathbf{n} + R^*(\omega_i + \omega_j) \times \mathbf{n} \tag{3.54}$$

By assuming the second particle's diameter to be infinite, particle - wall collision equations can be derived.

Three parameters should be defined for this model:

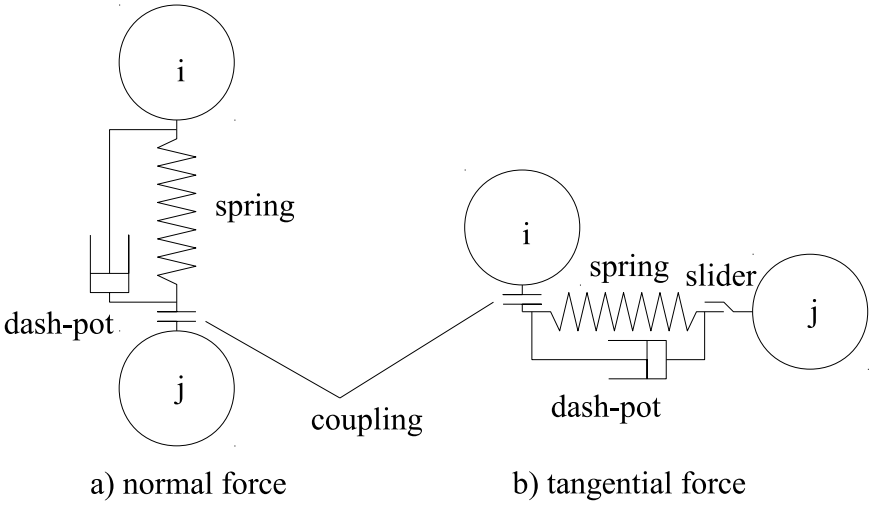

Figure 3.5: Contact forces in particle collision. Adapted from [Crowe et al., 2011]

- Stiffness k

  Stiffness can be calculated using Hertzian contact theory by using physical properties of particles as below:

(3.55) $$k_t = 8G^* \sqrt{R^* \delta_n}$$

(3.56) $$k_n = \frac{4}{3} Y^* \sqrt{R^* \delta_n}$$

- Damping coefficient η

  Damping coefficient is deduced from the stiffness as below:

$$\eta_n = -2\sqrt{\frac{5}{6}}\beta\sqrt{S_n m^*} \tag{3.57}$$

$$\eta_t = -2\sqrt{\frac{5}{6}}\beta\sqrt{S_t m^*} \tag{3.58}$$

- friction coefficient f

  Friction coefficient is measurable and can be described by an empirical value.

In these equations Y^*, G^*, R^*, β and S are defined as below:

$$\frac{1}{Y^*} = \frac{1-\nu_1^2}{Y_1} + \frac{1-\nu_2^2}{Y_2} \tag{3.59}$$

$$\frac{1}{G^*} = \frac{2(2+\nu_1)(1-\nu_1)}{Y_1} + \frac{2(2+\nu_2)(1-\nu_2)}{Y_2} \tag{3.60}$$

$$\frac{1}{R^*} = \frac{1}{r_1} + \frac{1}{r_2} \tag{3.61}$$

$$\beta = \frac{\ln(e)}{\sqrt{\ln^2(e) + \pi^2}} \tag{3.62}$$

$$S_n = 2Y^* \sqrt{R^* \delta_n} \tag{3.63}$$

$$S_t = 8G^* \sqrt{R^* \delta_n} \tag{3.64}$$

In the above equations, Y is the Young modulus of the particle, G is the shear modulus, ν is the Poisson ratio, e is the coefficient of restitution, m is the mass of the particle, and r is the radius of the particle.

The total force acting on particle i is the summation of the tangential and normal forces of particles which are in contact with particle i and is written as below:

$$\mathbf{F}_i = \sum_j (\mathbf{F}_{nij} + \mathbf{F}_{tij}) \tag{3.65}$$

And the torque can be calculated using summation of torques imposed to the particle i by tangential component of the contact force:

$$\mathbf{T}_i = \sum_j (R_i \mathbf{n} \times \mathbf{F}_{tij}) \tag{3.66}$$

3.6 Mixing and segregation

3.6.1 Introduction

A perfect mixture of two types of particles is achieved, when any sample drawn out of the batch of particles contains the same portion of particles components as in the whole mixture [Rhodes, 2008]. A perfect mixture of particles is not achievable. Instead, a random mixture of particles is defined to be a mixture of particles, in which the probability of finding a particle of any component is proportional to the composition of the mixture. Segregation of particles may occur, if physical properties of particles are different. In a segregating mixture, the probability of finding particles of one component in one part of the mixture is greater than the other component. Figure 3.6 presents schematics of the mixtures types [Rhodes, 2008].

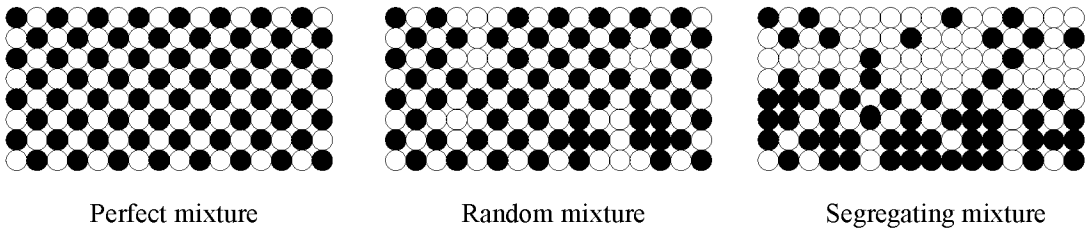

Figure 3.6: Mixtures types. Adapted from [Rhodes, 2008].

3.6.2 Segregation causes and mechanisms

In a mixture of particles, if any of the physical properties of a mixture component is different, then there is a tendency for separation of particles. In many of the mixing and segregation processes the size distribution, shape and density of the particles are significant factors in the mixture quality. Four mechanisms are distinguished in segregation processes based on the particles' size ratio [Rhodes, 2008]:

- Trajectory segregation

  According to the drag force on a sphere the retarding force on a particle is proportional to the square of its diameter, $f = \frac{1}{2}\rho_g U^2 C_d(\pi\frac{d_s^2}{4})$, and the deceleration of the particle can be calculated as below:

$$\text{Deceleration of the particle} = \frac{\text{retarding force}}{\text{mass of particle}} \tag{3.67}$$

  The travel distance of a particle to settle is proportional to the square of its diameter. Therefore, a particle of twice the diameter would move four times the distance to settle, which results in segregation of particles with different size. This method is used in a conveying belt mostly.

- Percolation of particles

  Particles of the same size tend to aggregate in a moving mass of particles. This movement trend leads to creation of a gap between the particles so that a smaller particle moves downward while a larger one moves upward. This mechanism mostly occurs in hoppers during charging and discharging of particles.

- Rise of coarse particles due to vibrations

  Vibrations in a mixture of particles of different size can cause segregation. Larger particles would travel upward while smaller particles move downward.

- Elutration segregation

  At the presence of an upward flow in a cylinder, particles with terminal velocities lower than the upward flow velocity are carried upward and heavier particles are settled.

3.6.3 Assessing the mixture

There have been many investigations to assess the quality of a mixture. While some of these studies consider the exchange coefficient between the bubble wake and the particles, others analyze the mixing indices based on statistical approaches. Over forty mixing indices have been developed to quantify the mixture quality. Poux et al. [1991] reviewed and compared mixing indices published in the literature. Some of the mixing indices are presented in Table 3.1.

Table 3.1: Mixing indices. Adapted from [Poux et al., 1991].

Index no.	**Author**	**Mixing Index**	**Range**
1	Lacey	$M = (\sigma_0^2 - S^2)/(\sigma_0^2 - \sigma_R^2)$	0 to 1
2	Kramer	$M = (\sigma_0 - S)/(\sigma_0 - \sigma_R)$	0 to 1
3	Lacey, Weidendam and Bonilla	$M = \sigma_R/S$	< 1 to 1
4	Ashton and Valentin	$M^2 = (\log \sigma_0^2 - \log S^2)/$ $(\log \sigma_0^2 - log\sigma_R^2)$	0 to 1
5	Poole, Taylor and Wall	$M = S/\sigma_R$	$\gg 1$ to 1
6	Carely Macauley and Donald	$M = (S^2 - \sigma_R^2)/(1 - (1/n))$	$\gg 0$ to 0

For simplicity the Lacey mixing index [Lacey, 1954] is selected as a tool in this study to measure the quality of the mixture and to compare with the published data for validation purposes.

The Lacey mixing index is the ratio of the achieved mixture to the b best possible mixture, and the range is from zero to one for a segregating mixture and a random mixture, respectively. This index is based on statistical approach and measures the

degree of the mixture using the variation of compositions among samples drawn out of the mixture, σ^2.

The standard deviation of a completely random mixture, composed of particles of the same size, σ_R^2, is calculated as below:

$$\sigma_R^2 = \frac{P(1-P)}{n} \tag{3.68}$$

where P is the overall portion of any component of the mixture and n is the number of particles in each sample.

The standard deviation of a segregating mixture, composed of mono-sized particles, can be estimated as below:

$$\sigma_0^2 = P(1-P) \tag{3.69}$$

which is independent of the sample size.

The standard deviation of a mixture samples can be estimated as below:

$$S^2 = \frac{1}{n}\sum_{i=1}^{n}(x_i - \bar{x})^2 \tag{3.70}$$

where $\bar{x}$ is the sample arithmetic mean defined as below:

$$\bar{x} = \frac{1}{n}\sum_{i=1}^{n} x_i \tag{3.71}$$

Chapter 4

Numerical method

The name CFD refers to the use of numerical methods and a computer, or computers, to model the fluid dynamics of a desired flow. In this method partial differential equations (PDE) and ordinary differential equations (ODE) forming the governing equations are approximated and numerical schemes are used to solve them. Discretization methods should be used to approximate the solution of differential equations by use of an equivalent system of algebraic equations. Three main methods are introduced in the literature for the discretization procedure [Ferziger and Perić, 2002]:

1. Finite difference method (FDM)

   FDM discretizes the domain into nodes and solves the differential equations for each node based on the neighboring nodes. The method is very straightforward and efficient on structured grids. However, the implementation of the method to complex flows and geometries is complex and conservation in not enforced unless special care is taken [Ferziger and Perić, 2002].

2. Finite element method (FEM)

FEM breaks the domain into a set of discrete volumes or finite elements, which are mostly unstructured. The differential equations are multiplied by weight functions before they are integrated over the entire domain. One of the simplest approximations to the solution over each element is the linear approximation constructed from the value of the boundaries. This approximation guarantees the continuity. This estimate is then multiplied by a weight function, which is mostly the same form of the solution. This approximation is then submitted into the weighted integral of the conservation law and by selecting the best solution from the set of allowed functions, which corresponds to the one with minimum residual, the final solution is found. This method satisfies the conservation and can be used for complex geometries by using unstructured grids [Ferziger and Perić, 2002].

3. Finite volume method (FVM)

   FVM divides the domain into a finite number of contiguous control volumes (CV) and solves the integral form of the conservation equations at the centroid of each CV. Interpolation methods are used to calculate the variables at the surface of each CV. The method uses both structured and unstructured grids, so it is suitable for complex geometries. Also, this method is conservative by considering the in-flux and out-flux of variables at the boundaries, and the rate of changes inside each CV. However, it is difficult to develop methods of orders higher than second for 3D domains compared to FEM, because FVM requires three levels of approximation: interpolation and integration [Ferziger and Perić, 2002].

A non-linear algebraic system of equations can be developed by using any of the methods mentioned above. Then, iterative methods are used to solve the system of

equations as below [Ferziger and Perić, 2002]:

$$\mathbf{A}\mathbf{x} = \mathbf{b} \tag{4.1}$$

$$\epsilon = \mathbf{A}\mathbf{x} - \mathbf{b} \tag{4.2}$$

where $\mathbf{A}$ is the matrix of coefficients, $\mathbf{x}$ is the variable vector, $\mathbf{b}$ is the source term vector and ϵ is the vector of iterations residual.

Following software packages are used to solve the discretized equations derived in Chapter 3:

- OpenFOAM ® 2-3-0

  OpenFOAM ® (Open Field Operation and Manipulation) is a free, open source CFD package developed by OpenCFD Ltd. at ESI Group and is distributed by the OpenFOAM Foundation. The software is coded in C++ programming language and benefits from the modularity and object oriented features of C++. This feature enables the software to the development of customized numerical solvers and pre-/post processing utilities for CFD [Weller et al., 1998]. OpenFOAM is based on FVM and solves PDEs and ODEs.

- LIGGGHTS® - Public

  LIGGGHTS® (LAMMPS Improved for General Granular and Granular Heat Transfer Simulations) is an open source software package for modeling granular material by the implementation of discrete element method (DEM) [Kloss et al., 2012]. LIGGGHTS® is based on LAMMPS® (Large Atomic and Molecular Massively Parallel Simulator), which is an open source software package developed by Sandia National Laboratories for Molecular dynamics simulations

on distributed memory machines [Plimpton, 1995]. LIGGGHTS is based on FDM and solves ODEs.

- CFDEM® coupling - 2.3.0

  CFDEM® coupling (Computational Fluid Dynamics - Discrete Elements Method coupling) is an open source software package developed mainly by DCS Computing and is a modular framework which couples and transfers data between CFD code and the DEM code using the particle - fluid interactions and volume fraction [Goniva et al., 2012].

4.1 Solver: cfdemSolverPiso

cfdemSolverPiso is a coupled CFD-DEM solver, which couples the CFD solver, pisoFoam, to the DEM engine, LIGGGHTS. The CFD solver uses the volume averaged Navier-Stokes equations for the continuous phase and the DEM engine solves Newton's equations of motion for the dispersed phase. The coupling code calculates forces on the particles due to the flow field and transfers them to the DEM engine, LIGGGHTS, where the trajectory and position of particles are calculated and updated in the CFD solver. The pisoFoam is a finite volume based solver for unsteady, incompressible, and turbulent flows, which uses the PISO algorithm, first introduced by Issa [1986].

4.1.1 Governing equations

Following the description of the physics of the problem in Chapter 3.5.2, a summary of the equations which are used in this study are presented in Table 4.1.

Table 4.1: Governing equations used in Eulerian - Lagrangian approach for simulation of fluidization process and segregation process

Mass conservation for gas phase	$\frac{\partial \epsilon_g}{\partial t} + \nabla \cdot (\epsilon_g \mathbf{u}) = 0$
Momentum conservation for gas phase - Model A	$\frac{\partial \rho_g \epsilon_g \mathbf{u}}{\partial t} + \nabla \cdot (\rho_g \epsilon_g \mathbf{u}\mathbf{u}) = -\epsilon_g \nabla P - \mathbf{F}^{\mathrm{A}} + \nabla \cdot (\epsilon_g \tau) + \rho_g \epsilon_g \mathbf{g}$ $\mathbf{f}_{p-f,i} = -V_{p,i} \rho_g \mathbf{g} + V_{p,i} \nabla p_{d,i} + \epsilon_g \mathbf{f}_{drag,i}$
Momentum conservation for gas phase - Model B	$\frac{\partial \rho_g \epsilon_g \mathbf{u}}{\partial t} + \nabla \cdot (\rho_g \epsilon_g \mathbf{u}\mathbf{u}) = -\nabla P - \mathbf{F}^{\mathrm{B}} + \nabla \cdot (\epsilon_g \tau) + \rho_g \epsilon_g \mathbf{g}$ $\mathbf{f}_{p-f,i} = -V_{p,i} \rho_g \mathbf{g} + \epsilon_s \mathbf{f}_{drag,i} + \epsilon_g \mathbf{f}_{drag,i}$
Stress tensor	$\tau_g = \frac{1}{2} \left(\nabla \cdot \mathbf{u} + (\nabla \cdot \mathbf{u})^T \right)$
Particle momentum Equation	$m_i \frac{d\mathbf{u}_{p,i}}{dt} = \mathbf{f}_{p-f,i} + \sum_{j=1}^{k_i} (\mathbf{f}_{c,ij} + \mathbf{f}_{d,ij}) + \rho_{p,i} V_{p,i} \mathbf{g}$
Coupling scheme	$\mathbf{F} = \frac{\sum_{i=1}^{k_c} \mathbf{f}_{p-f,i}}{\nabla V}$ [Xu and Yu, 1997]
Drag models	Gidaspow [2012] Di Felice [1994] Koch and Hill [2001]
Particle - particle interactions	Soft sphere approach. See Section 3.5.2.

4.1.2 Solution algorithm

The algorithm for the solution of the problem is as follows [Goniva et al., 2012]:

1. Particles' positions and velocities are calculated in the DEM solver.
2. Particles' positions, velocities, and other necessary data are transferred to the CFD solver.
3. The corresponding control volume of each particle is determined based on its location in the domain.
4. Volume fraction and a mean velocity are determined for particles in the respective computational cell.
5. Fluid forces which are acting on each particle are calculated.

6. Particle - fluid interaction forces and momentum exchange are assembled by using the ensemble averaging method over all particles in a CFD cell.

7. Forces on the particles due to the flow field are transferred to the DEM solver to be used in the next time step.

8. Fluid velocity and pressure are calculated in CFD cells and particles are represented by the volume fraction and momentum exchange term.

9. Additional equations are solved for both phases, such as heat transfer and species transfer.

10. The routine is repeated from (1).

The gas phase solver, pisoFoam, is based on the pressure implicit with splitting of operator (PISO) algorithm first introduced by Issa [1986], which is as below:

1. Set the boundary conditions.

2. Use the velocity and pressure fields from the previous time step, (u^n) and (p^n), or initial condition as an immediate estimate for the current time step.

3. Calculate an estimate for the current time step velocity (u^{m*}) field by solving the linearized momentum equation.

4. Solve the pressure correction equation to obtain the pressure correction term (p').

5. Correct the velocity and pressure fields by using the pressure correction term and find the velocity (u^m) and pressure (p^m) fields which satisfy the continuity equation.

6. Solve the second pressure correction equation and correct the velocity (u^m) and pressure (p^m) fields again.

7. Repeat from 3 using the corrected velocity (u^m) and pressure (p^m) fields as the improved estimations until all corrections are negligible and store the latest values for velocity and pressure fields as (u^{n+1}) and (p^{n+1}) respectively.

8. Increase the time step and repeat from step 1 [Ferziger and Perić, 2002].

Particles' force balances and their trajectories are calculated using Newton's law of motion in LIGGGHTS. LIGGGHTS is based on LAMMMPS, which uses the fast parallel algorithm for short-range molecular dynamics developed by Plimpton [1995] as below:

1. A list of non-zero interacting neighboring pairwise particles is generated.

2. Interaction forces, F_x are calculated for each pairwise particles and summations of the forces are stored in the force matrix, f_x.

3. New position of particles are computed by using the force balance of each particle, f_x, and then they are stored in the position matrix, x_x.

4.1.3 File structure

CFDEM ® coupling and OpenFOAM ® use the dictionary files to define the parameters of the simulation. Dictionary files are created in the simulation run folder under two main sub-folders, namely CFD and DEM. The CFD folder contains information related to the gas phase, geometry and the grid of the gas phase simulation, and the DEM folder includes information required by LIGGGHTS for calculation of particles' force balance and positions, such as particle diameter, density, properties and

simulation domain properties. Figure 4.1 presents a schematic of the file structure of the simulation setup.

4.2 Model setup

The workbench experiment developed by Feng and Yu [2004] is used in the current work to model the fluidization and segregation process in the fluidized bed. Results are compared for verification and validation purposes. Figure 4.2 presents a schematic of the geometry, mesh and initial conditions of the model.

4.2.1 Geometry

A rectangular bed, width = 65 mm, height = 260 mm and depth = 8.1 mm, is used in the simulation to study the fluidization and segregation process in the fluidized bed.

4.2.2 Mesh

The domain is discretized into structured hexahedral control volumes. Grid sensitivity analysis is performed to study the effect of the grid size on the simulations' results.

4.2.3 Boundary conditions

Velocity inlet boundary condition is used for the inlet considering the volume fraction of the gas phase to be one and for particles to be zero, so that just air is injected at the inlet. The effect of the inlet velocity is studied by considering different inlet velocities and comparing to the minimum fluidization velocity of the jetsam particles.

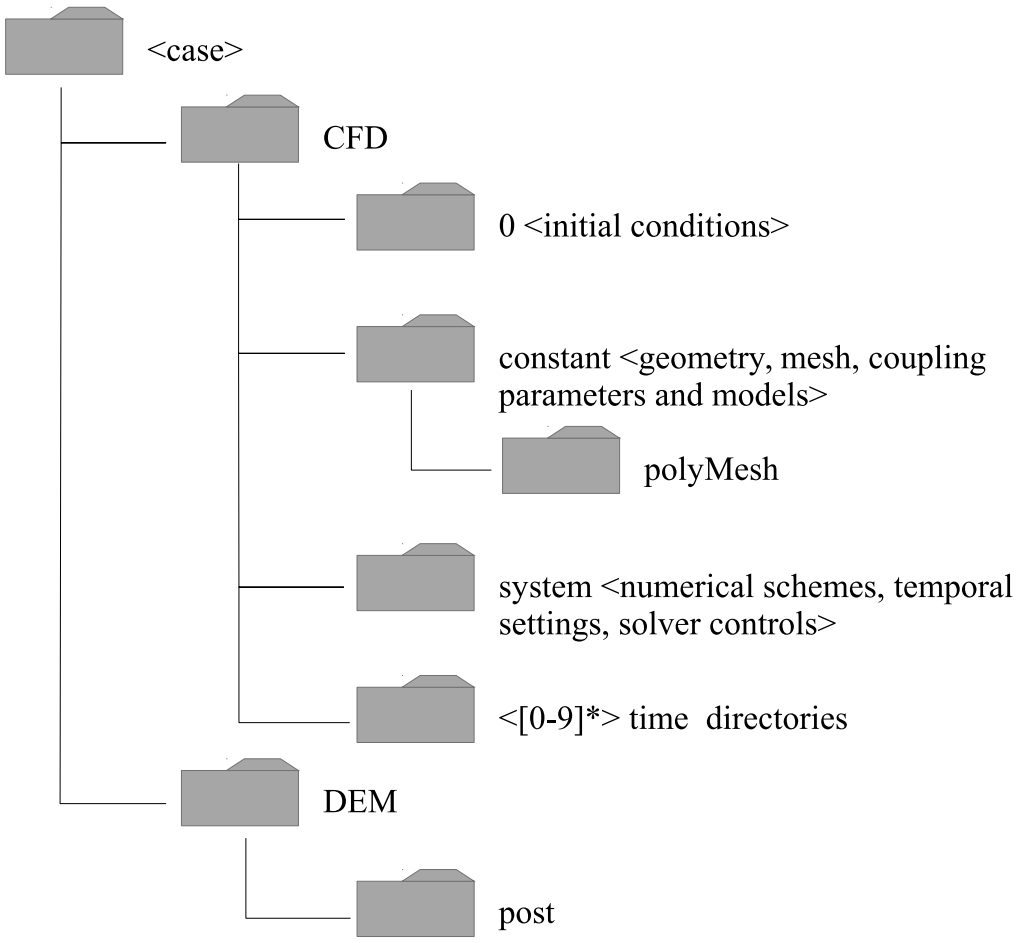

Figure 4.1: CFDEM ® coupling file structure.

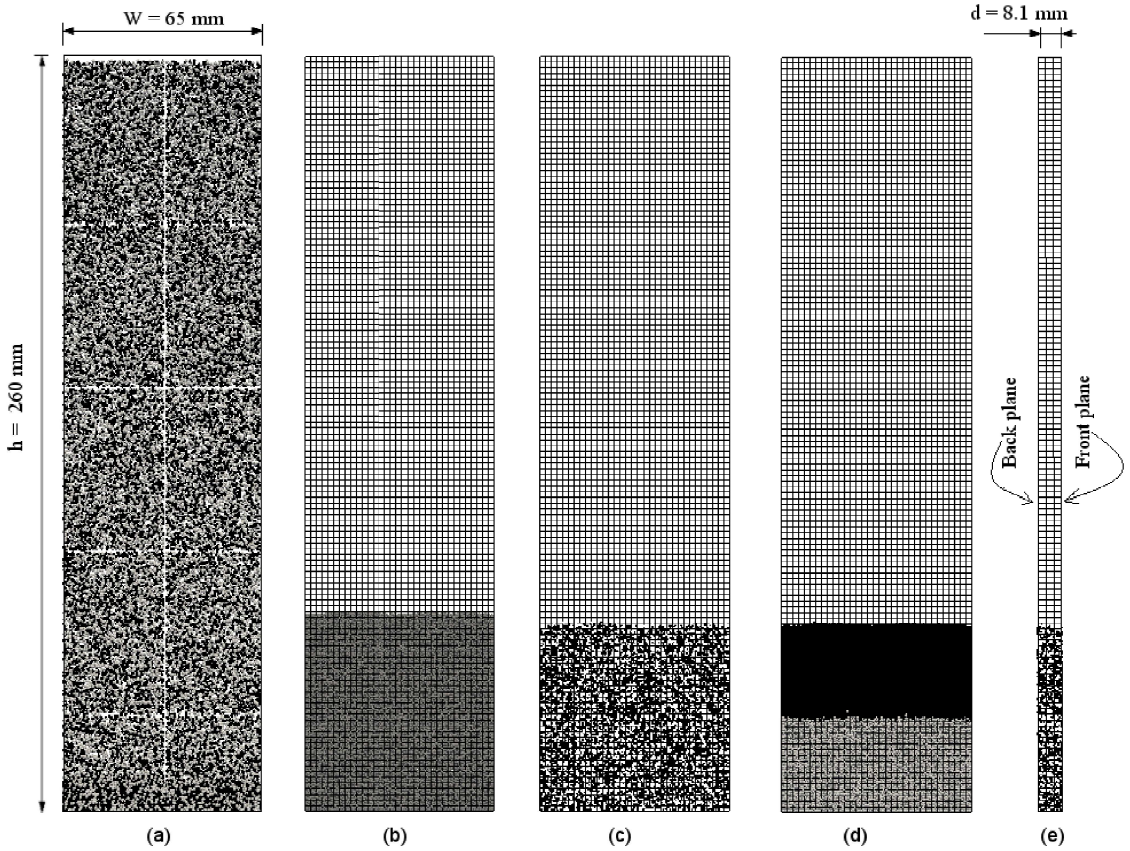

Figure 4.2: Schematic of the geometry, mesh, and initial conditions of the model.
(a) Preparation of the initial condition of the bed by inserting particles at random positions in domain.
(b) Initial condition of fluidization process.
(c) Initial condition of the segregation process - mixed.
(d) Initial condition of the segregation process - segregated.
(e) Side view of the bed.

Pressure outlet is used at the outlet, using a value of zero relative pressure. Particle volume fractions at the outlet are set to zero, so that particles cannot leave the domain.

Slip wall is used for the gas phase on the side walls. The implementation of locally averaged variables does not allow the no-slip boundary conditions for walls [Anderson and Jackson, 1967]. Hertzian walls with the coefficient of restitution of 0.9 are considered for the solid phase.

The effect of front and back planes on the results of simulations is studied by considering periodic and slip wall boundary conditions for the gas phase and periodic, frictional wall, and ideal wall for the dispersed phase.

4.2.4 Materials

Air at -50℃ is used as the gas phase and sand is used as the particles. Later, bitumen pellets at -50℃ are added to study the segregation process. Properties of phases are set according to suggested values in the literature. See Table 5.1 for an overview of properties.

4.2.5 Numerical schemes

The numerical schemes used in a simulation play an important role in the results of the simulations. Following schemes are used for discretization of equations terms:

- First order implicit Euler is used for temporal discretization.
- The divergence terms are estimated by Gaussian scheme with limited linear interpolation scheme.
- The Laplacian terms are estimated by Gaussian scheme with linear correction.

- The linear interpolation scheme is used as default for all terms, otherwise mentioned.

See Appendix A for the complete dictionary of the numerical schemes and explanations.

4.2.6 Initial conditions

The packed bed is formed by inserting 40,000 particles at random positions without overlap in the whole domain when the internal fluid velocity is set to zero. The particles are settled down due to the gravity force.

To study the effect of the initial condition on the segregation process, two different initial conditions are considered namely, initially mixed and initially inverse segregated. In the initially mixed case, flotsam and jetsam particles are inserted at random positions simultaneously to create a fully mixed bed as the initial condition, and a packed bed with Lacey mixing index of one is generated (see Figure 4.2c). The inverse segregated packed bed is formed by adding flotsam particles in a box lower than the jetsam. A packed bed containing two distinct layers of flotsam and jetsam is formed of which the Lacey mixing index is estimated to be zero (see Figure 4.2d).

4.2.7 Computational method

CFDEM ® coupling uses domain decomposition method for parallelization. The domain is transferred to OpenFOAM for simulation of the continuous phase where it is decomposed into sub-domains. Each CPU core is dedicated to one of the sub-domains for calculations. The DEM engine is responsible for calculations of the dispersed phase by using the fast parallel algorithm for short-range molecular dy-

namics to decompose the domain and calculate the force balance and position of particles.

Simulations are performed using a local computer and a cluster on WestGrid and ComputeCanada for parallelization and speed up purposes.

High performance computing

DEM is a resource intensive computational method and it is necessary to use multi-CPU core systems to speed up the process.

A parallel efficiency test is conducted to evaluate the feasibility and efficiency of the parallelization of the solver. The test is performed both on the local server and on the Jasper server at WestGrid facilities. The local server is an Intel Core i7 system with six physical cores at 3.2 GHz clock and 32 GB of RAM. The Jasper server is an SGI Altix XE cluster with an aggregated total of 400 nodes containing 4160 cores and 8320 GB of memory. Jasper nodes consist of Xeon X5676 processors, 12 CPU cores (2 CPUs and 6 cores on each CPU) and 24 GB of memory. The domain is decomposed horizontally and vertically into sub-domains.

Table 4.2: Parallel efficiency test results on Jasper server.

Vertical $\times$ Horizontal decomposition = Number of CPU cores	**Efficiency**	**Speed-up**	**Clock time for 1 s of simulated time**
Ref. $2 \times 1 = 2$	100 %	2	12837
$2 \times 2 = 4$	70.8 %	2.83	9057
$4 \times 1 = 4$	65.3 %	2.61	9829
$4 \times 2 = 8$	100 %	8	3209
$8 \times 1 = 8$	99.5 %	7.92	3240
$6 \times 2 = 12$	94.4 %	11.33	2267
$12 \times 1 = 12$	92.8 %	11.13	2306
$12 \times 2 = 24$	64.9 %	15.59	1646
$24 \times 1 = 24$	59.9 %	14.37	1786

The CFDEM®coupling is designed based on Message Passing Interface (MPI), and at least two CPU cores are required to run in parallel mode. The simulation time of a run with two CPU cores is used as the reference and simulation times are compared with it. Table 4.2 shows parallel efficiency test results. The Jasper sever uses the qsub and torque softwares to schedule jobs. According to their policy CPU cores and nodes are assigned to the jobs based on the job request. A node consisted of Intel Xeon L5420 might be assigned to a job which requests less than 8 CPU cores. As it can be observed in Table 4.2 the efficiency of cases with four CPU cores, a linear speed up was not gained. However, a good scaling was achieved up to 12 CPU cores. For the simulations with 24 CPU cores the speed up of the simulation did not increase linearly. This is mainly because of running simulations on two nodes rather than one node.

The speed-up for the reference test is considered to be 2 and for the other cases the speed-up is defined as below:

$$\text{Speed-up} = \frac{\text{Clock time for the Reference test}}{\text{Clock time for the case}} \times 2 \tag{4.3}$$

The efficiency of the reference test in considered to be 100% and for the other cases the efficiency is defined as below:

$$\text{Efficiency} = \frac{\text{Speed-up}}{\text{Number of CPU cores}} \times 100 \tag{4.4}$$

Chapter 5

Simulation of fluidization process

Air-sand fluidization is simulated as the first step to ensure the model is capturing the hydrodynamics of the fluidized bed. Results of these two-phase simulations are compared with published data. The third phase, bitumen, will be added later to study the segregation process. The pressure drop is estimated along the bed as a response variable and the particles' mean velocity is used as the second response variable. Both response variables are sensitive to the entire flow field within the fluidized bed and, therefore, are good solution indicators.

As it was discussed in Chapter 2, proper grid size is a significant factor in prediction of the bed hydrodynamics. To satisfy the volume average continuity and momentum equations which are introduced by Anderson and Jackson [1967], the minimum grid size is limited to be larger than the particles diameter in each direction [Müller et al., 2009].

Proper boundary conditions are required for a well-posed problem. Periodic and wall boundary conditions are considered to study the effect of the boundary conditions on the flow behavior.

The effect of drag models and momentum exchange models on the simulation results are examined and the simulation settings are set accordingly. The response variables (pressure drop along the bed and particles' mean velocity) are used to compare results with the results of previous works.

5.1 Reference simulation run

The reference simulation properties and settings are presented in Table 5.1.

Table 5.1: Reference simulation run setup

Description	**Value**	**Comment**
Gas density (kg m^{-3})	1.534	Air at -50℃
Gas viscosity (m^2s^{-1})	9.55e-6	Air at -50℃
Particle density (kg m^{-3})	2500	Sand density
Particle diameter (mm)	1	Constant
Particle Young's modulus (Nm^{-2})	1.0×10^7	Feng and Yu [2004]
Particle Poisson ratio (N m^{-1})	0.33	Feng and Yu [2004]
Particle restitution coefficient	0.9	Feng and Yu [2004]
Particle friction coefficient	0.3	Feng and Yu [2004]
Bed size (w × h × d (m))	0.065 × 0.26 × 0.0081	Feng and Yu [2004]
Static bed height (m)	0.065	40,000 particles
Inlet conditions	$\mathbf{u}_g = 0.9$ m s^{-1} $\mathbf{u}_s = 0$ m s^{-1} $\frac{\partial}{\partial \mathbf{n}} p = 0$ $\epsilon_g = 1$	Velocity inlet $\mathbf{u}_g \sim 1.5\ \mathbf{u}_{mf}$

Outlet conditions	$\frac{\partial}{\partial \mathbf{n}}\mathbf{u}_g = 0$ $\frac{\partial}{\partial \mathbf{n}}\mathbf{u}_s = 0$ $p_{relative} = 0$ Pa $\epsilon_g = 1$	Pressure outlet
Side walls	$\frac{\partial}{\partial \mathbf{n}}\mathbf{u}_g = 0$ $\frac{\partial}{\partial \mathbf{n}}\mathbf{u}_s = 0$ $\frac{\partial}{\partial \mathbf{n}}p = 0$ $\frac{\partial}{\partial \mathbf{n}}\epsilon = 0$	Slip walls
Front and back planes	$\frac{\partial}{\partial \mathbf{n}}\mathbf{u}_g\|_{front} = \frac{\partial}{\partial \mathbf{n}}\mathbf{u}_g\|_{back}$ $\frac{\partial}{\partial \mathbf{n}}\mathbf{u}_s\|_{front} = \frac{\partial}{\partial \mathbf{n}}\mathbf{u}_s\|_{back}$ $\frac{\partial}{\partial \mathbf{n}}p\|_{front} = \frac{\partial}{\partial \mathbf{n}}p\|_{back}$ $\frac{\partial}{\partial \mathbf{n}}\epsilon\|_{front} = \frac{\partial}{\partial \mathbf{n}}\epsilon\|_{back}$	Periodic
Drag function	Koch & Hill	Hill et al. [2001b]
Numerical scheme	Central differencing scheme	See Appendix A
Convergence criteria	p: 1e-6 $\mathbf{u}$, ϵ: 1e-5	L_2 norm, see Appendix A
Timestep	CFD: 5e-5 s DEM: 1e-5 s	

In this table $\mathbf{n}$ represents the normal vector of the boundary. A complete dictionary of numerical schemes, equation solvers, tolerance and algorithms can be found in Appendix A.

Table 5.2: 2D grid sensitivity analysis, grid size and statistical information

Case No.	**Number of CVs in width × height × depth**	**Maximum nominal cell size (mm)**	**Number of nodes**	$\frac{\Delta L}{d_p}$
Case 1	15 × 60 × 1	8.1	900	8.1
Case 2	22 × 88 × 1	8.1	1936	8.1
Case 3	33 × 132 × 1	8.1	4356	8.1
Case 4	50 × 200 × 1	8.1	10000	8.1

5.2 Grid sensitivity analysis

A rectangular box with dimensions defined in Table 5.1 is created as the simulation domain. The domain is discretized into orthogonal hexahedral uniform size control volumes. 2D and 3D grid sensitivity analyses are performed by using four different grids for each case to study the effect of grid size on the simulation results. The grid is generated using the *blockMesh* command for grid generation in OpenFOAM.

5.2.1 2D grid sensitivity analysis

The height and width of the bed are discretized into parallel control volumes while the depth of the bed is fixed to be one control volume for the preliminary runs. Table 5.2 presents different grid sizes and statistical information of the grids used in the simulations.

The reference simulation setup values are used for the grid independence analysis. The pressure drop in the system as a global response variable is used to compare results of different simulations with the Ergun analytical equation of the pressure drop. Plots of average normalized solid velocity (ANSV) versus normalized run time (NRT) are used for comparison of results of different cases. The ANSV and NRT are defined as [Azimi et al., 2015]:

$$ANSV = \frac{\text{Average absolute solid velocity}}{\text{Inlet air velocity}} \tag{5.1}$$

$$NRT = \frac{\text{Simulation time (s)}}{\text{Plug flow residence time (s)}} = \frac{\text{Simulation time (s)}}{\left[\frac{\text{Static bed height (m)}}{\text{Superficial air velocity } (\text{ms}^{-1})}\right]} \tag{5.2}$$

Figure 5.1 shows the ANSV in NRT. It can be observed that the average ANSV increases as the size of control volumes are decreasing. The oscillations in ANSV are signs of presence of bubbles in the bed [Azimi et al., 2015]. The amplitudes of oscillations are constant and solutions are stable.

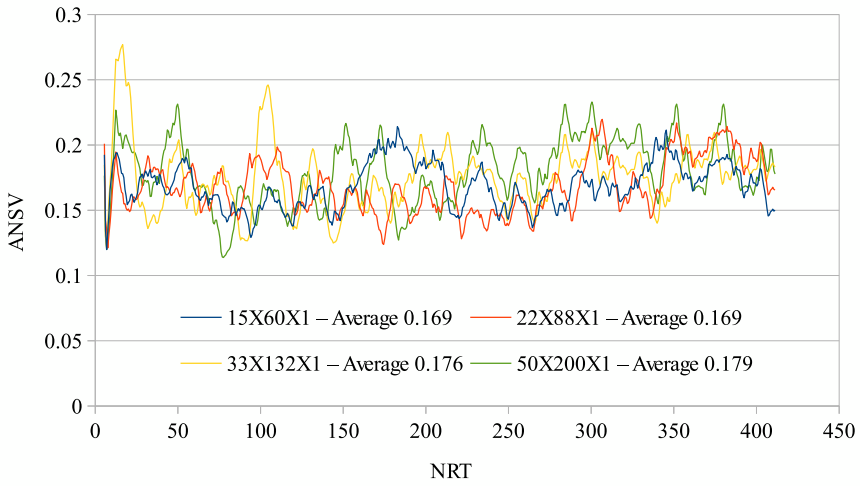

Figure 5.1: ANSV of 2D grid sensitivity analysis

Figure 5.2(a) shows the time averaged ANSV versus number of nodes and Figure 5.2(b) shows the time averaged pressure drop of the bed versus the number of nodes used in simulations. It can be observed that the ANSV and the pressure drop values

are increasing but an asymptotic behavior is not achieved. This lack of asymptotic behavior could be mainly due to the presence of the third direction gradients in the fluidized bed. These gradients are not captured by using a single control volume in that direction. To capture the third direction gradients and approach a grid independent solution, the domain is discretized in the third direction. The result of third dimension refinement is given in the next section.

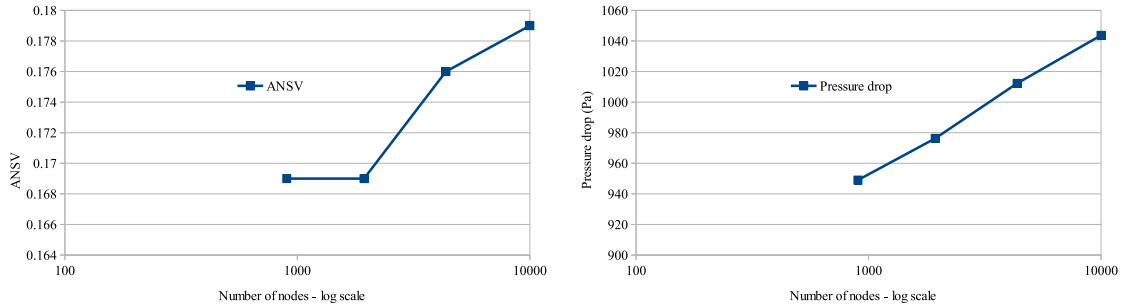

(a) ANSV versus number of nodes.

(b) Pressure drop versus number of nodes.

Figure 5.2: Pressure drop and ANSV versus number of nodes - 2D refinement of a slice of the bed.

5.2.2 3D grid sensitivity analysis

The 2D refinement of the simulation box suggested the presence of gradients in the third direction. These gradients are not captured by using one single control volume in that direction. The domain is now discretized in the third direction to capture the gradients of the flow in the third direction. Table 5.3 shows the different mesh size and statistical information of grids used in the simulation for the grid refinement in the third direction.

Table 5.3: 3D grid sensitivity analysis, grid size and statistical information.

Case No.	**Number of divisions in X × Y × Z**	**Maximum nominal cell size**	**Number of nodes**	$\frac{\Delta L}{d_p}$
Case 1	15 × 60 × 1	8.1	900	8.1
Case 2	22 × 88 × 2	4.05	3,872	4.05
Case 3	33 × 132 × 3	2.7	13,068	2.7
Case 4	50 × 200 × 4	2.025	40,000	2.025

Figure 5.3 shows the ANSV in NRT of the bed for the 3D refined cases. The oscillation of the ANSV implies the presence of bubbles in the bed. It can be observed that the amplitude of oscillations are fixed, and the solution is stable.

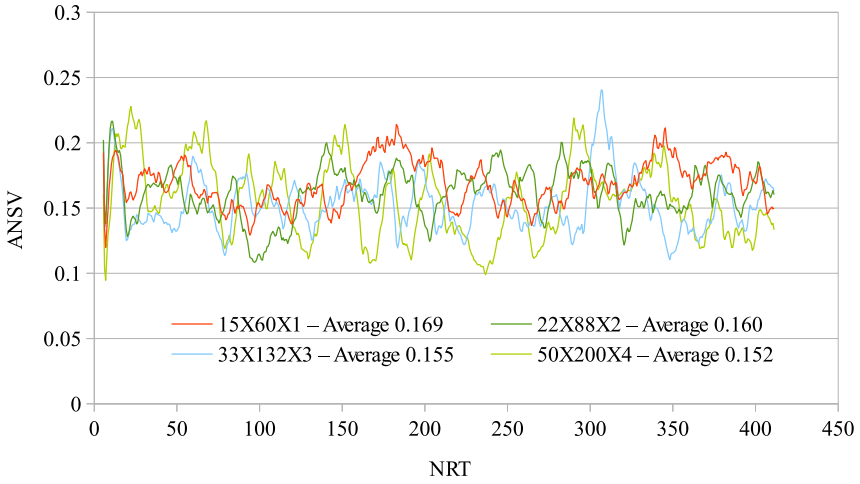

Figure 5.3: ANSV of 3D grid sensitivity analysis

Figure 5.4(a) shows the time averaged ANSV versus number of nodes and Figure 5.4(b) shows the time averaged pressure drop of the bed versus the number of nodes used in simulations. An asymptotic behavior can be observed for the ANSV and pressure drop values. The pressure drop value is approaching the constant values of 1091.25 kPa, which can be calculated using the Ergun equation. The error order of

the simulations, p-value, is estimated by the Richardson's extrapolation equation on results of the last three pressure drop values, and it was found to be to be 1.32. The estimated error order is in good agreement with the order of linear discretization scheme which is 2. The exact pressure drop value is estimated to be 1091.26 Pa by the Richardson's extrapolation which is in good agreement with the predicted value of the Erqun equation, 1084.22 Pa and the error is about 0.65%.

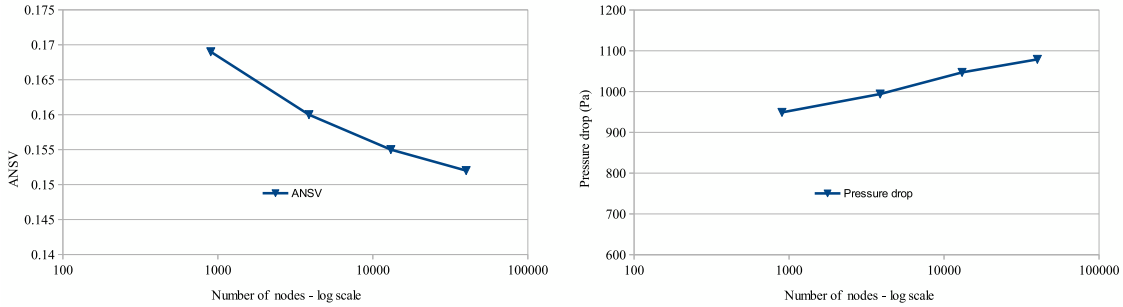

(a) ANSV versus number of nodes.

(b) Pressure drop versus number of nodes.

Figure 5.4: Pressure drop and ANSV versus number of nodes - 3D refinement of a slice of the bed.

Hence, the grid generated by using 13068 (33×132×3) control volumes produces grid independent results, while the size of each CV is greater than two diameters of the particles, as discussed in Chapter 2. Because it shows the best performance and accuracy compromise, this grid will be used for the analysis from here.

5.3 Effect of the drag coefficient

Among all the forces in a fluidized bed, the drag forces of the flow on particles are the most significant forces. Different drag models are available in the literature to calculate the drag force on a particle in a particle cloud as discussed in Section 3.5.2.

The available drag models in the CFDEM® coupling are Gidaspow [Gidaspow, 2012], DiFelice [Di Felice, 1994], and Koch & Hill [Hill et al., 2001b] models.

The pressure drop along the bed is used as an integral quantity to show the effects of drag models on the simulations results. Figure 5.5 shows computed instantaneous pressure drop in the bed versus NRT. The Gidaspow drag model predicts lower time averaged pressure drop in time compared to the two other drag models. Both DiFelice and Koch & Hill drag models estimate the same time averaged pressure drop values. All models converge to steady state and fluctuations in all cases are a sign of presence of large bubbles or slugging in the bed, a poorly fluidized bed, [Kunii and Levenspiel, 1969]. Kunii and Levenspiel [1969] predicted that the pressure drop versus inlet velocity in a poorly fluidized bed might fluctuate up to 10% of the mean value of the pressure drop. Figure 5.6 shows the diagram of pressure drop in a poorly fluidized bed, where large bubbles are formed and slugging might happen in the bed [Kunii and Levenspiel, 1969]. According to Equation 3.2 and Equation 3.1 the maximum and operating pressure drop of a bed with specifications of Table 6.3 are estimated to be 1130 Pa and 975 Pa, respectively.

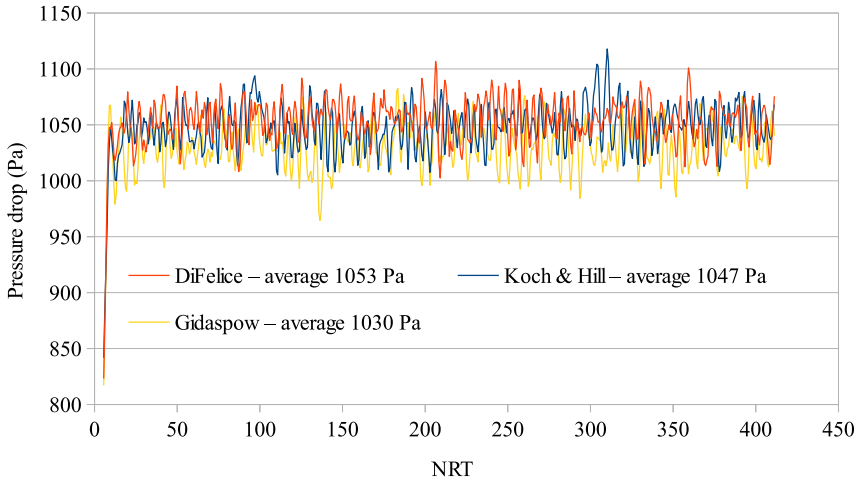

Figure 5.5: Bed pressure drop versus NRT of three different drag models

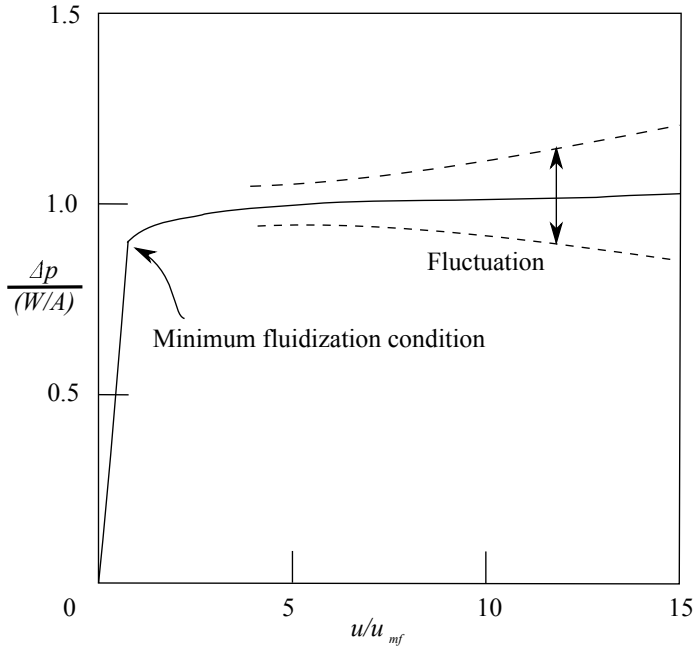

Figure 5.6: Pressure drop in a poorly fluidized beds. Adapted from [Kunii and Levenspiel, 1969]

Screenshots of the bed confirm the presence of large bubbles and slugging in the

bed. Figure 5.7 shows the initial condition of the bed and formation of large bubbles and slugging flow in the bed using Koch & Hill drag model.

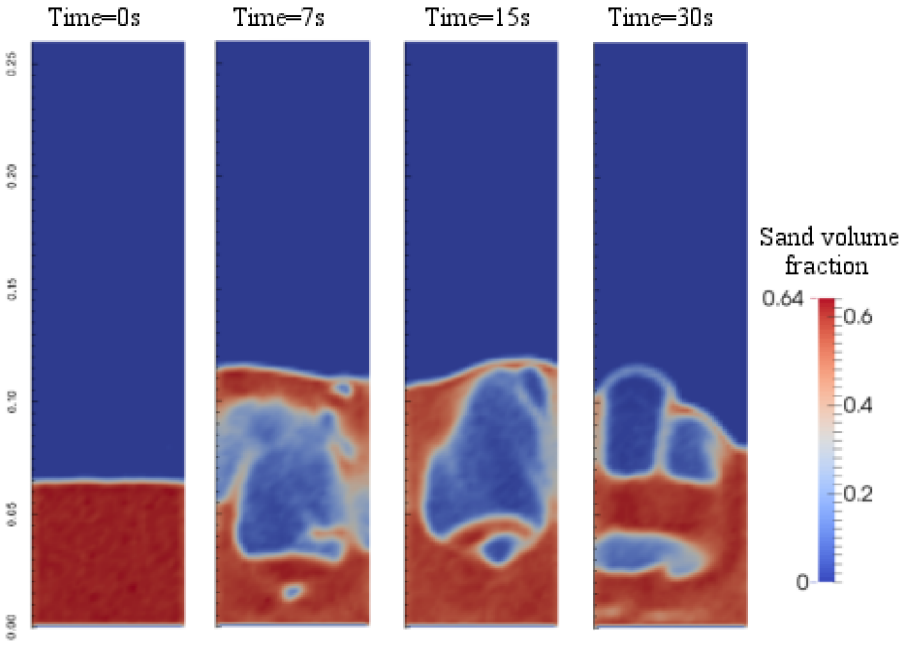

Figure 5.7: Contour of sand volume fraction of bed using Koch & Hill drag model

Figure 5.8 shows the ANSV in NRT for three different cases. It can be observed that the Gidaspow drag model calculated higher ANSV compared to the other models. Fluctuations of ANSV are an evidence of the presence of bubbles in the bed, as discussed above. Gidaspow drag model shows more peaks in the ANSV, which mean that there are bigger bubbles in the bed compared to the Koch & Hill drag model.

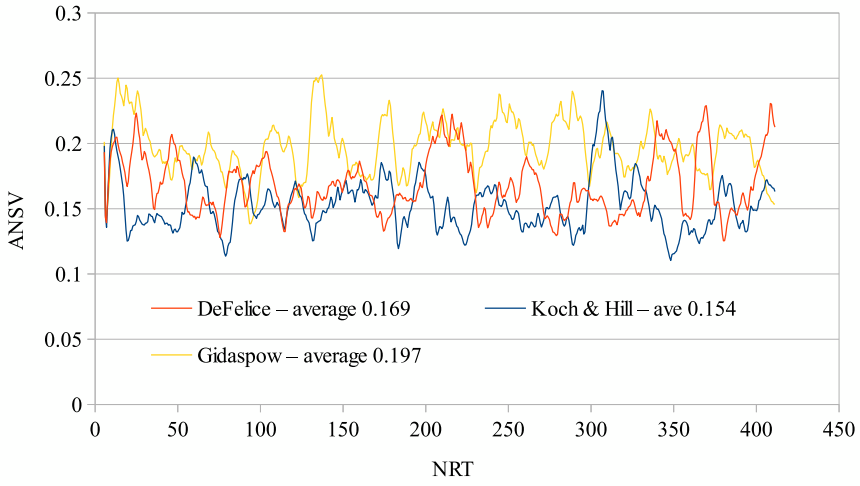

Figure 5.8: ANSV versus NRT for three different drag models.

Figure 5.9 (a) shows the time-averaged void fraction at z=0.02 m. As expected, the void fraction in the center of the bed is higher than at the side walls [Müller et al., 2009]. The void fraction in the center of the bed increases as bubbles are formed at the distributor plate and move rapidly to the center of the bed. These bubbles move towards the surface of the bed, where they erupt. Figure 5.9(b) shows the void fraction of the bed at z=0.05 m in the upper part of thebed. The Gidaspow drag model trend does not follow the bell shape of the void fraction proposed by Xu et al. [2004]. This error could be mainly due to the presence of a discontinuity in Gidaspow drag model at $\epsilon = 0.8$.

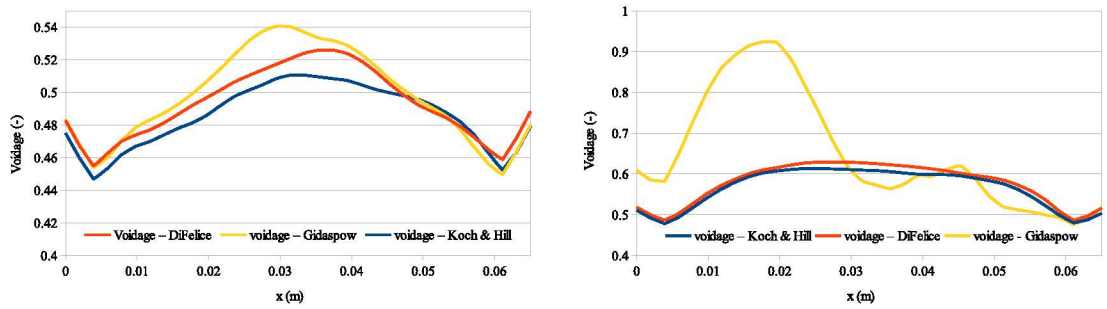

(a) At z=0.02 m (b) At z=0.05 m

Figure 5.9: Comparison of time averaged void fraction of the bed for three different drag models at z=0.02 m (a) and z=0.05 m (b).

Figure 5.10 shows the vector field of particles' time averaged velocity. It can be observed that the Gidaspow drag model predicts regions of higher particle velocity and particles are moved from the center of the bed to the sides.

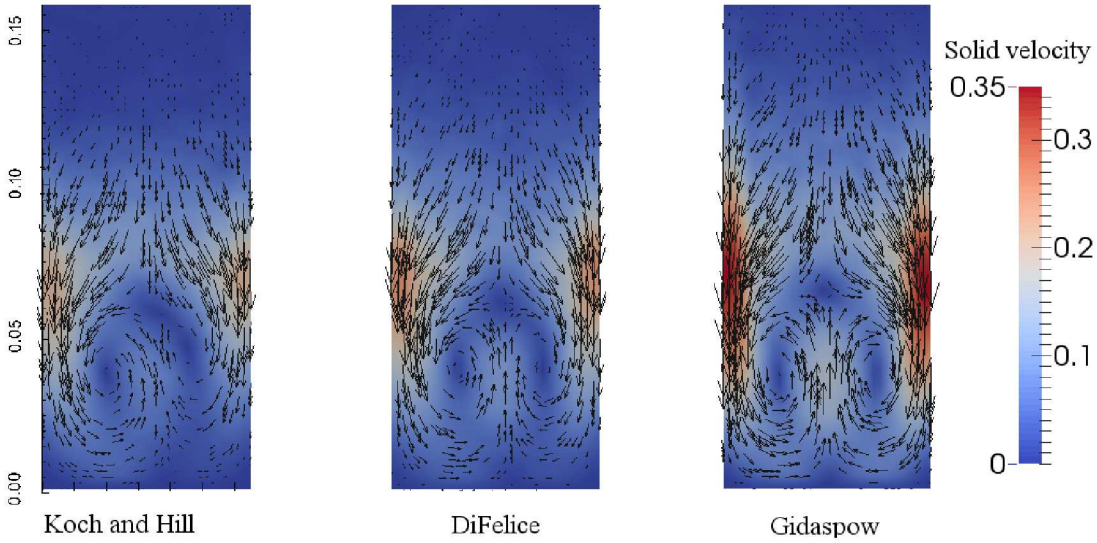

Figure 5.10: Comparison of time averaged particles velocity using three different drag models.

Figure 5.11 shows fluid and solid momentum exchange per unit volume of the bed.

The momentum exchange term is the summation of drag force, lift force, pressure gradient force, and other applicable forces. Koch & Hill and DiFelice drag models show similar trends in the simulation. However, the Koch & Hill drag model is based on Lattice Boltzmann simulation and it predicts the highest drag at volume fractions of gas, which is most likely to happen in a dense fluidized bed [Lundberg and Halvorsen, 2008].

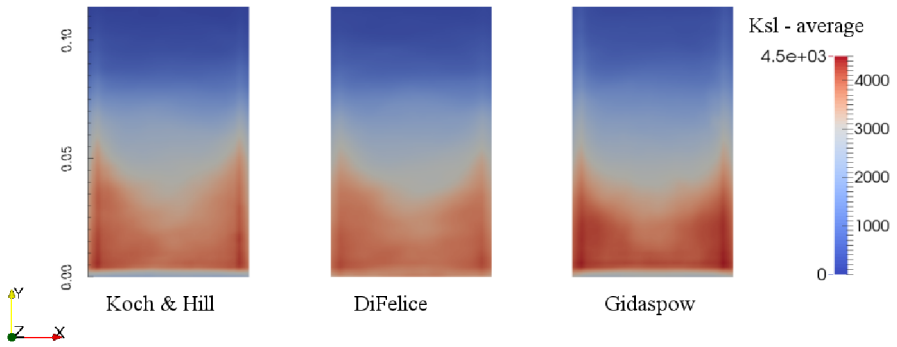

Figure 5.11: Time averaged particle-fluid momentum exchange of the bed of three different drag models.

5.4 Effect of the boundary conditions

The front and back planes are set to either frictional wall or periodic type to study the effect of these boundary conditions on the hydrodynamics of the bed. The frictional walls are considered to have the same physical properties of particles, such as restitution coeff., friction coeff., as listed in Table 5.1. Free-slip condition is imposed for the flow field of the gas phase, even in the case of frictional walls, due to restrictions of the local averaging method. Figure 5.12 compares the pressure drop values for frictional walls with periodic boundary condition on the front and back planes. Frictional wall boundary condition predicts slightly higher pressure drop,

which could be caused by dissipation of particles' kinetic energy and formation of dense zones in the bed.

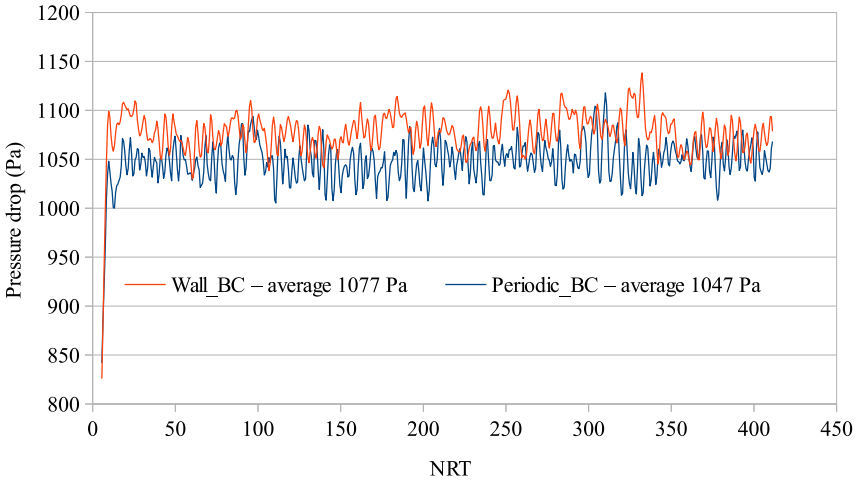

Figure 5.12: Bed pressure drop versus NRT for frictional wall and periodic boundary conditions.

Figure 5.13 presents the ANSV versus NRT comparison for these cases. It can be observed that the time averaged ANSV for the frictional wall condition is 52% less than the periodic boundary condition. The different calculated values of ANSV confirms the idea of dissipation of particles' kinetic energy when colliding with the walls.

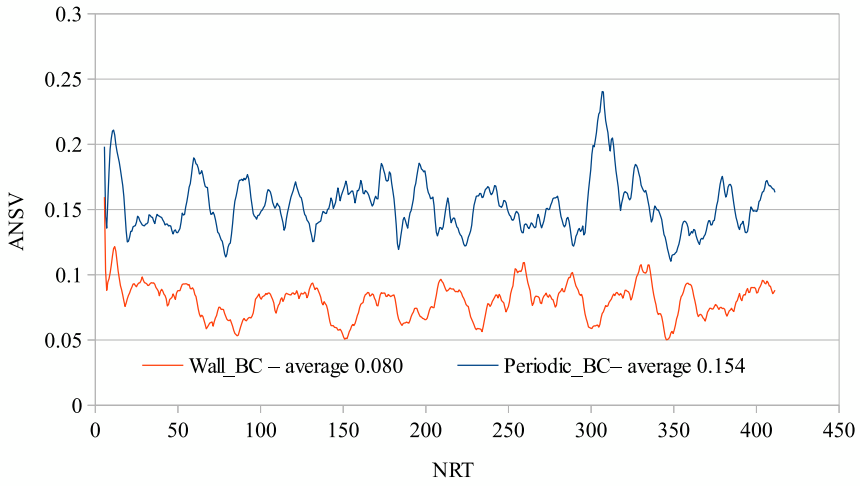

Figure 5.13: ANSV versus NRT for frictional wall and periodic boundary conditions.

Figure 5.14 (a) and Figure 5.14 (b) present time averaged void fraction of the bed at the height of $z = 0.02$ m and $z = 0.05$ m, respectively. It can be observed that the void fraction at the height of $z = 0.02$ m is not affected by the boundary condition setup and the value of the void fraction is equal for both boundary condition types. However, at the height of $z = 0.05$ m, the void fraction is lower in the simulation with frictional wall boundary conditions compared to the periodic boundary condition. Because of dissipation of kinetic energy in the particle-wall collisions, the particles are not moved to the higher elevation of the bed and the void fraction decreases.

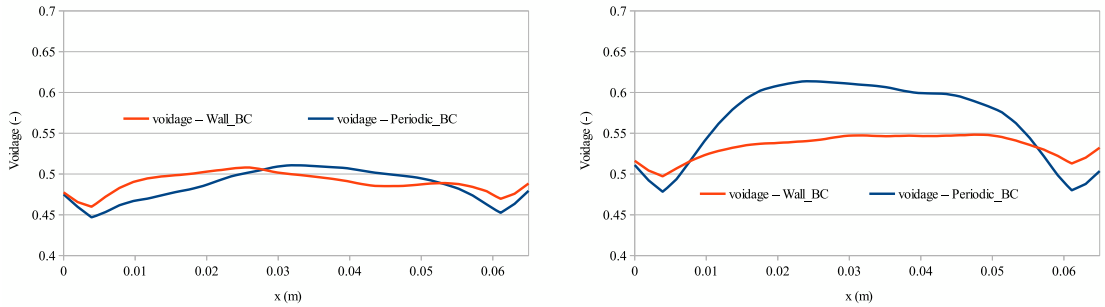

(a) At z=0.02 m (b) At z=0.05 m

Figure 5.14: Time averaged void fraction of the bed of frictional wall and periodic boundary conditions at $z = 0.02$ m (a) and z=0.05 m (b).

5.5 Model A and Model B

The treatment of the momentum exchange term, as discussed in Section 3.5.2, plays a significant role in the result of simulations of gas-solid flows. There has been extensive research on the effect of the treatment of momentum exchange term on the flow field in fluidization process. The objective of the current analysis is to demonstrate differences in the results of simulations using the momentum exchange term models. The pressure drop of the bed in time and ANSV versus NRT are considered to study the effect of the momentum exchange term on the results of the simulations.

Table 5.4 presents the treatment of momentum exchange term and forces which are included in each case.

Table 5.4: Momentum exchange term models and forces

Forces	**Model A**	**Model B**
Pressure gradient force	✓	-
Viscous force	✓	-
Archimedes force	-	✓

Figure 5.15 shows the pressure drop versus time for Model A and Model B. It can be observed that Model B predicts a lower pressure drop in the bed compared to Model A. The time mean value of the pressure drop predicted by Model B is 12% less than predicted value by Model A. The pressure drop in a fluidized bed with parameters of Table 5.1 is calculated to be 975 kPa according to the analytical equation of pressure drop in bed, Equation 3.1. It can be observed that Model B pressure drop is predicting 6% smaller than the analytical estimated value while model predicts 7% greater. Figure 5.16 shows ANSV versus NRT of the bed. Model A calculated smaller mean time ANSV compared to Model B. Further investigation is required to analyze the effect o the momentum exchange term model on the results of the simulations. However, [Feng and Yu, 2004] suggested that the Model B is more favorable for simulation of fluidization process.

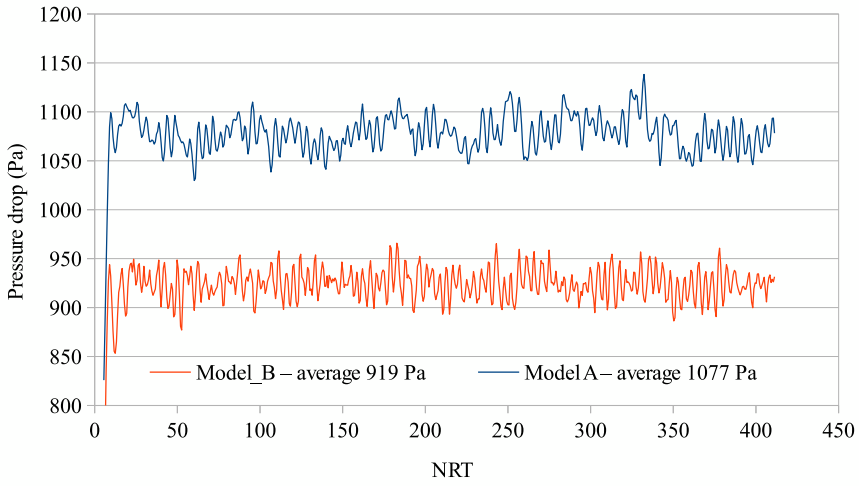

Figure 5.15: Bed pressure drop using Model A and Model B for momentum exchange term.

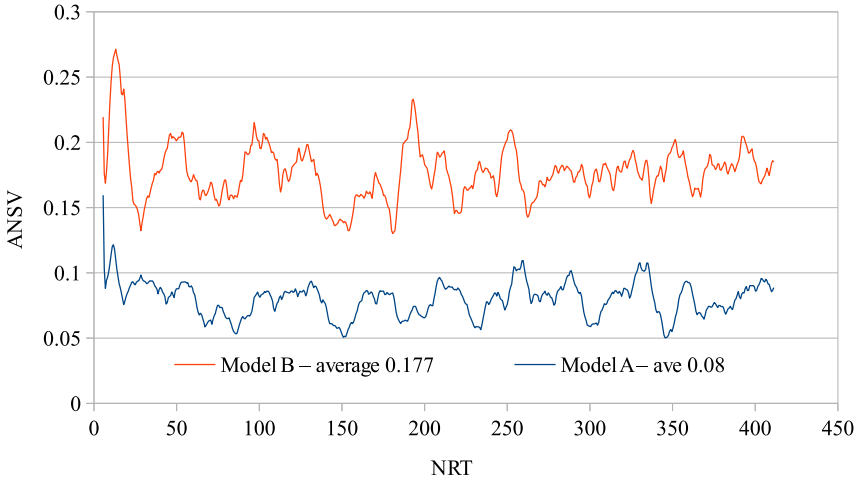

Figure 5.16: ANSV versus NRT, Model A and Model B for momentum exchange term.

Chapter 6

Simulation of segregation of particles in fluidized bed

The Discrete Element Method (DEM) is used to study the segregation of particles in a fluidized bed. Following results of the fluidization process in Chapter 5, the simulation settings, such as mesh size and numerical schemes, are set. The Lacey mixing index is used to quantify the quality of the mixture and provide a statistical picture of it. The affecting parameters on the mixing index are studied to analyze the sensitivity of the mixing index and provide an accurate picture of the mixture.

The segregation process is analyzed in a bed formed by a binary mixture of particles with a high density ratio (2.5) at the first step to analyze the effect of boundary conditions and momentum exchange model. The effect of superficial inlet velocity on the final quality of the mixture and rate of segregation of particles is explained.

Later, the density ratio of the mixture components is decreased to 1.33 in order to increase the sensitivity of the segregation process and analyze the effect of different

parameters on the quality of the mixture. The effect of carrier phase properties and the aspect ratio of the bed on the final quality of mixture and rate of segregation is analyzed.

6.1 Lacey mixing index

The Lacey mixing index [Lacey, 1954], as described in Section 3.6.3, can be used to quantify the quality of the mixture. The Lacey mixing index compares the achieved mixing to the possible mixture, which is based on statistical analysis. Based on this statistical approach, the following parameters should be considered in the calculation of the mixing index: box width and the sample size. Both are investigated to determine their optimal values. The value of the mixing index is substituted by the average of the ten neighboring points in time to remove the noise from the plots of the Lacey mixing index.

6.1.1 Box width

The DEM method uses an adjustable sample size and a proper sample size needs to be determined which represents an accurate statistical picture of the mixture. Rectangular boxes are used to discretize the domain and obtain samples of the mixture. Once the width of the boxes are fixed, the height of the boxes are changed so that the total number of particles in each sample is the same and the scale of scrutiny is fixed. A Matlab code was developed for this purpose, which can be reached at Appendix B.

Table 6.1 shows for all the test cases the number of particles in each sample box and the number of divisions in the width of the bed to measure the mixing index.

The bed properties are taken from Table 6.3(p. 95) with frictional wall boundary conditions for front and back planes and Model A for the momentum exchange term.

Table 6.1: Sample size

Case	**Divisions in width**	**Sample size**
2×20000	2	20000
2×10000	2	10000
10×200	10	200
10×400	10	400
10×1000	10	1000
20×200	20	200
20×2000	20	2000
100×200	100	200

Figure 6.1 and Figure 6.2 show particles' mean elevation and their elevation standard deviation in time, respectively. It can be observed that the average height of jetsam particles decreases, while the average height of the flotsam particles increases. Also, the standard deviation of particles' heights is decreasing for both components of mixture. This statistical analysis of the bed suggests that flotsam particles aggregate at the top, and jetsam particles aggregate at the bottom of the bed, as expected.

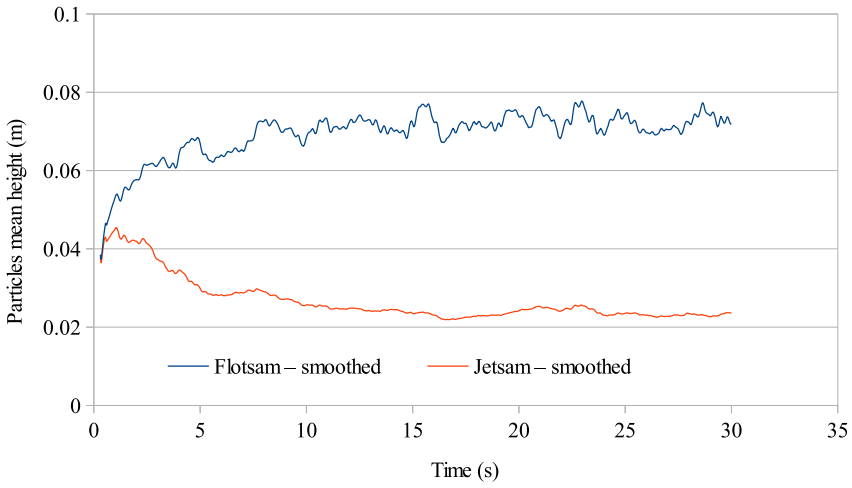

Figure 6.1: Particles' mean height in time.

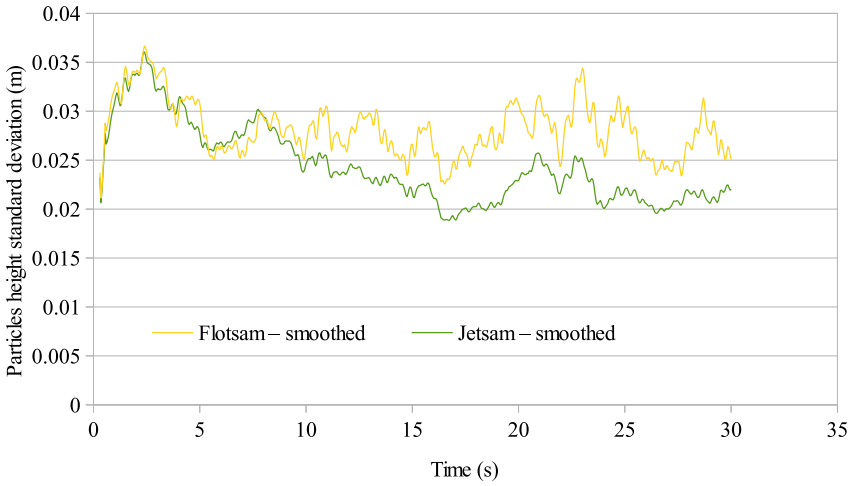

Figure 6.2: Standard deviation of particles' height in time.

Figure 6.3 shows the mixing index in time for different box widths, represented by the number of horizontal divisions of the bed. It can be concluded that the bed should be divided into a reasonable number of horizontal divisions, as it can

be observed that the extreme levels of divisions, 2 and 100, produce poor statistical pictures of the mixture. A number of divisions above 10 does not seem required to improve the results.

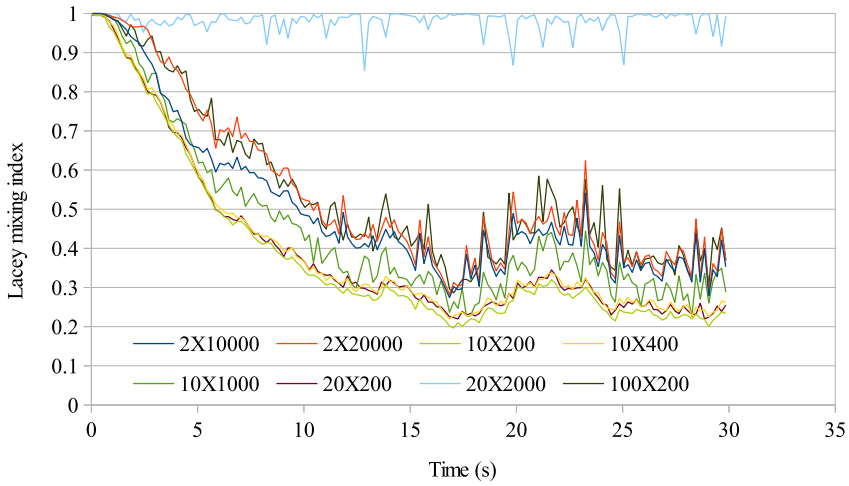

Figure 6.3: Effect of sample size on the Lacey mixing index in time.

6.1.2 Sample size

The sample size can affect the mixing index. In the current work, the total area of the bed is scanned so that the required number of samples are provided to represent the bed.

Figure 6.3 shows the mixing index in time using different sample size for the same bed in time. It can be observed that the mixing index estimated based on the sample size of 200 to 400 is independent of the sample size and represents the mixture statistically.

Following these results of mixing index analysis, the sample size of 200 and number of divisions in the width of 10 will be used for analysis of the mixture in next

sections.

6.2 Validation

Feng and Yu [2004] analyzed segregation of a binary mixture of particles in a fluidized bed by performing numerical simulations and experiments. A binary mixture of particles with the same density and different diameters was fluidized for enough time to be segregated. They compared results of the numerical simulations to experiments. A series of simulations with same conditions as their work is considered to validate the CFDEM® coupling software. A rectangular box with the same dimensions of their work is used as the simulation domain which is discretized into orthogonal hexahedral control volumes, as described in Section 5.2. Description of the simulation settings can be found in Table 5.1. Table 6.2 presents the solid phase properties.

Table 6.2: Parameters used for the validation case adapted from Feng and Yu [2004]

Description	**Particle**	**Value**	**Comment**
Particle density	Flotsam	2500	Sand
(kg m^{-3})	Jetsam	2500	Sand
Particle diameter	Flotsam	1	Constant
(mm)	Jetsam	2	Constant
Number	Flotsam	22,223	50% mass fraction
of particles	Jetsam	2,777	50% mass fraction

For a fluidized bed formed from particles described in Table 6.2, the maximum pressure drop of the bed is calculated to be 1083 Pa using Equations 3.1. Figure 6.4 presents the variation of pressure drop in time using Model A for momentum exchange model, when the superficial gas velocity is 1.2 m s^{-1}. The mean value of the numerical pressure drop in the study by Feng and Yu [2004] using Model A is

estimated to be 1043 Pa, while it is estimated to be 1022 Pa in the current work, which is 2% less.

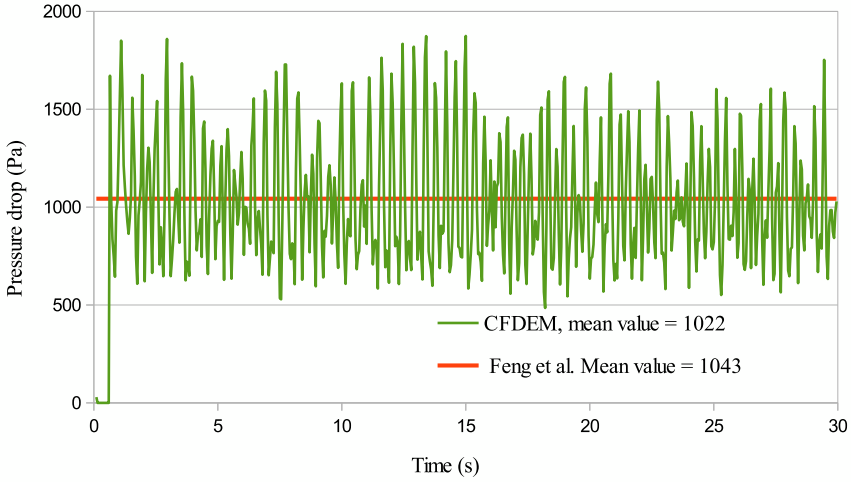

Figure 6.4: Comparison of pressure drop in bed using Model A when superficial gas velocity is 1.2 m s^{-1}.

Figure 6.5 presents the variation of the pressure drop in time using Model B for momentum exchange model, when superficial gas velocity is 1.2 m s^{-1}. The mean value of the numerical pressure drop in the study by Feng and Yu [2004] using Model B is estimated to be 1042 Pa, and it is estimated to be 1021 Pa in the current run with Model B, which is 2% less.

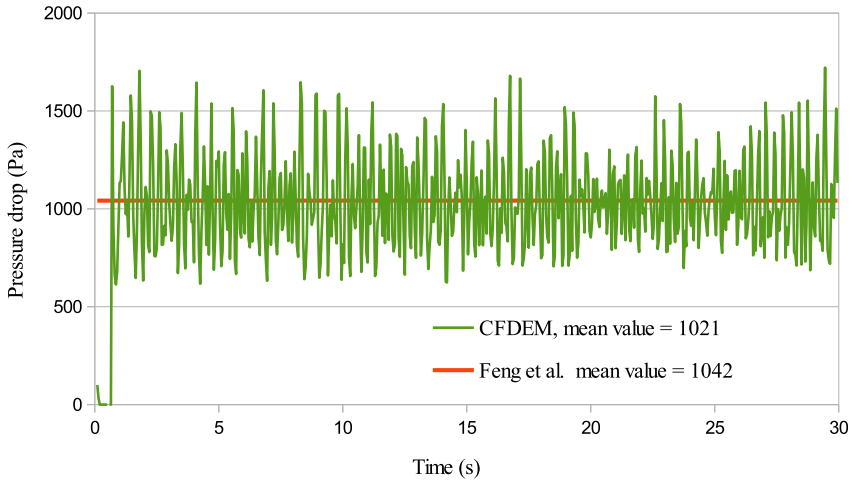

Figure 6.5: Comparison of pressure drop in bed using Model B when superficial gas velocity is 1.2 m s^{-1}.

The quality of the mixture is quantified by the Lacey mixing index which was described in Section 6.1. Figure 6.6 presents variation of Lacey mixing index in time for a fluidized bed formed from particles with physical properties of Table 6.2. Similar trends can be observed for both momentum exchange terms in the current simulations and the study by Feng and Yu [2004]. However, differences can be observed in comparison with the current work and their results. These differences could be mainly due to the sampling method used for the Lacey mixing index. Feng and Yu [2004] used fixed sample cell size, in which case the variance of particles' volume fraction is weighted according to the equivalent number of particles to estimate the Lacey mixing index. In that method, the number of particles in each sample cell is not fixed, which affects the scale of scrutiny. Besides, it should be noticed that the Lacey mixing index is influenced by the number of particles in each sample [Fan et al., 1970]. This could explain the differences between the Lacey indices from Feng and Yu [2004] and from the present results. But we notice that the trend of Model

A and Model B in both simulations is the same.

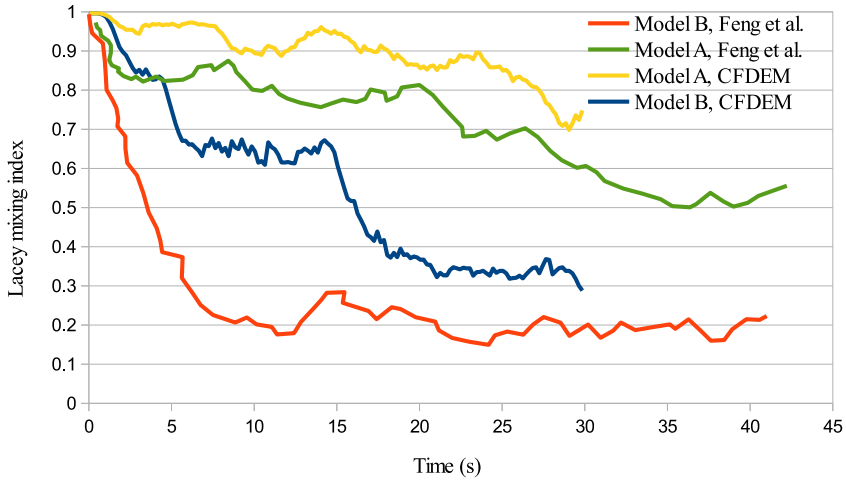

Figure 6.6: Comparison of Lacey mixing index from simulations with results from Feng and Yu [2004].

Therefore, the present model can be considered validated by comparison with Feng and Yu [2004] numerical results, which in turn were validated by them with experiment.

6.3 Sand and bitumen

The third phase is considered to be pellets of bitumen at a very low temperature of -50℃, and is added to the sand particles to study the segregation process in the fluidized bed. The domain is considered to be the same size of the study performed by Feng et al. [2004] and is discretized into 13,068 orthogonal hexahedral control volumes as described in Section 5.2.2. Table 5.1 shows the reference simulation setup and the third phase properties are shown in Table 6.3 below.

Table 6.3: Reference simulation settings

Description	Particle	Value	Comment
Particle density	Flotsam	1000	Bitumen at -50℃
(kg m^{-3})	Jetsam	2500	Sand at -50℃
Particle diameter	Flotsam	1	Constant
(mm)	Jetsam	1	Constant
Number	Flotsam	20,000	50% volume fraction
of particles	Jetsam	20,000	50% volume fraction

The packed bed is formed by inserting particles at random positions in the bed without overlapping, when there is no gas injected to the inlet at the presence of the gravity field for 0.5 s. Particles are settled and a packed bed of random mixture is formed. Then, the gas is uniformly injected at the inlet and particles are fluidized. The pressure drop of the bed is considered a charectiristic quantity to compare with Equation 3.1, the analytical solution of pressure drop for validation of the results. Averaged normalized solid velocity (ANSV) versus normalized run time (NRT) is plotted to study the hydrodynamics of the bed.

Lacey mixing index is used as a tool to quantify the quality of mixture and to compare the simulation results with published data.

6.3.1 Effect of the boundary conditions and momentum exchange model

Comparison with 3D case

Following results of simulations of fluidization process in Section 5.4 the front and back planes condition can affect the hydrodynamics of the fluidized bed. Here, the effect of boundary conditions applied to these planes on the results of segregation process simulation is studied carefully to increase the accuracy of the results. Peri-

odic, frictional wall, and reflective walls are considered for this purpose, and results of the narrow channel case are compared with the simulation of a bed with a square (0.065×0.065 m) cross-section, referred to as the 3D case. The total number of particles is changed to 321,000 particles to keep the height of the bed the same as the narrow channel case. The bed is discretized into 143,748 (33×33×132) orthogonal hexahedral control volumes. Models A and B of momentum exchange are considered separately. Table 6.4 presents front and back planes setup used in the simulations.

Table 6.4: Different boundary conditions used in simulation models.

Description	**Phase**	**Value**
Periodic	Gas phase	Periodic boundary condition
	Particles	Periodic boundary condition
Frictional wall	Gas phase	Slip wall
	Particles	Frictional wall, e=0.9
Reflective wall	Gas phase	Slip wall
	Particles	Reflective wall
3D case	Gas phase	Slip wall
	Particles	Frictional wall, e=0.9

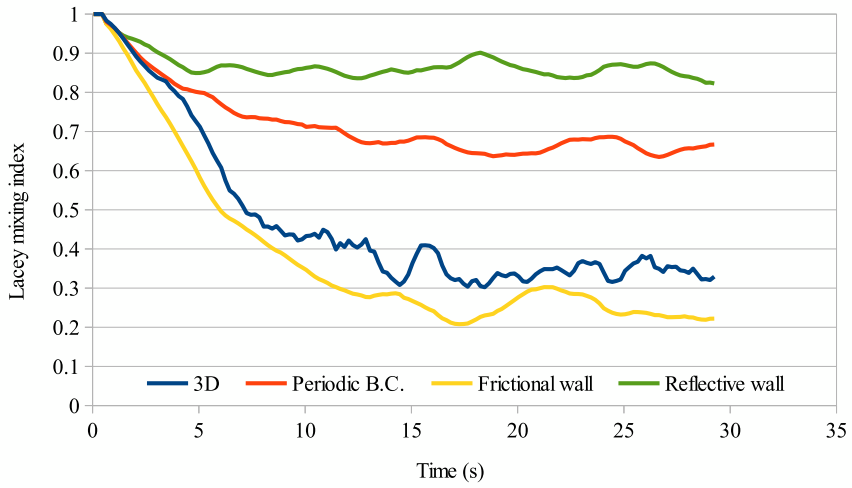

Figure 6.7: Effect of discrete phase boundary condition on Lacey mixing index - Model A.

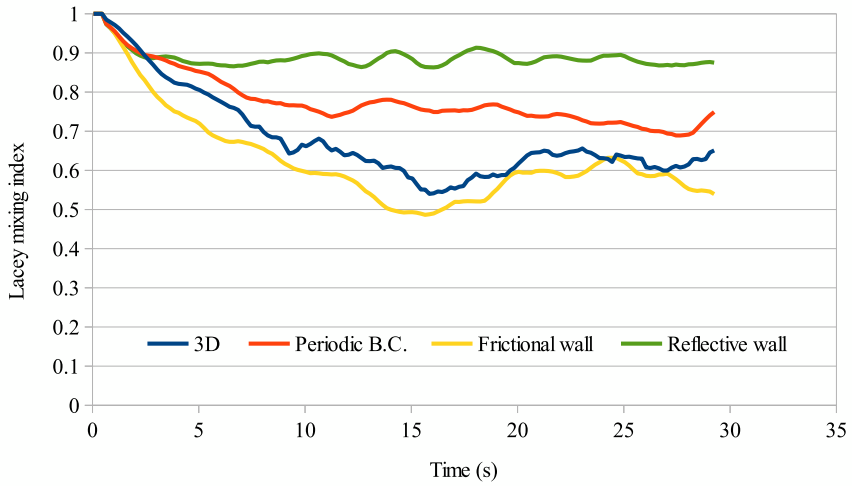

Figure 6.8: Effect of discrete phase boundary condition on Lacey mixing index - Model B.

Figure 6.7 and Figure 6.8 a show comparison of Lacey mixing index versus time for different boundary conditions applied to the narrow channel and the 3D case using

Model A and Model B for particle-fluid momentum exchange model, respectively. For both momentum exchange models, the frictional wall condition for the front and back planes clearly approaches the mixing index predicted by the 3D case in the macroscopically stable state condition of the bed better than the other two boundary conditions. Figure 6.9(a-d) shows detailed comparisons of the effect of boundary conditions on ANSV in NRT. The frictional wall boundary condition shows the best agreement with the 3D case for both Model A and Model B. The dissipation of kinetic energy in the particles - wall collision may be the source of the differences in the results. The idea that the dissipation of particles' kinetic energy is the cause for the differences between these boundary conditions can be further confirmed by considering the reflective wall case. Regardless of the momentum exchange model, the ANSV values of both mixture components have higher value for the reflective wall cases compared to the other two cases.

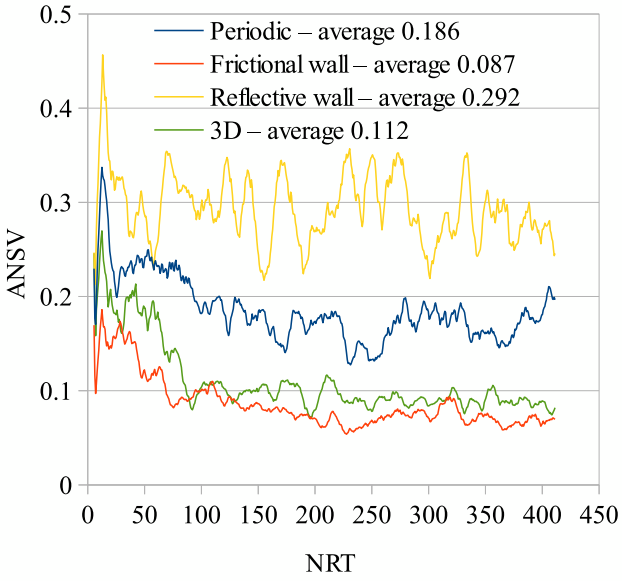

(a) Model A - Sand

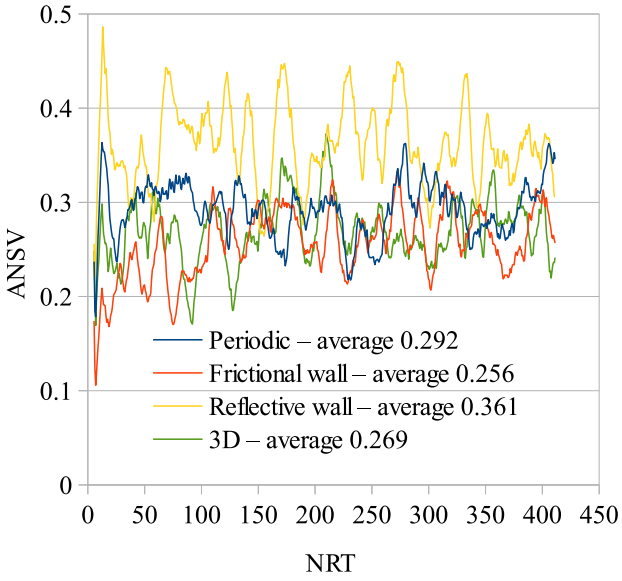

(b) Model A - Bitumen

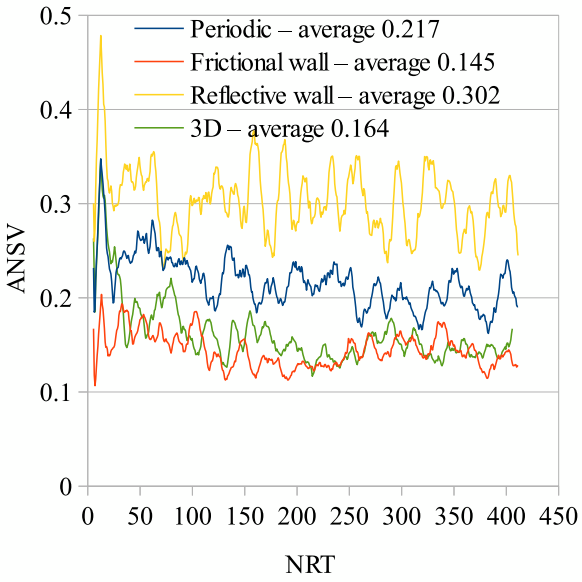

(c) Model B - Sand

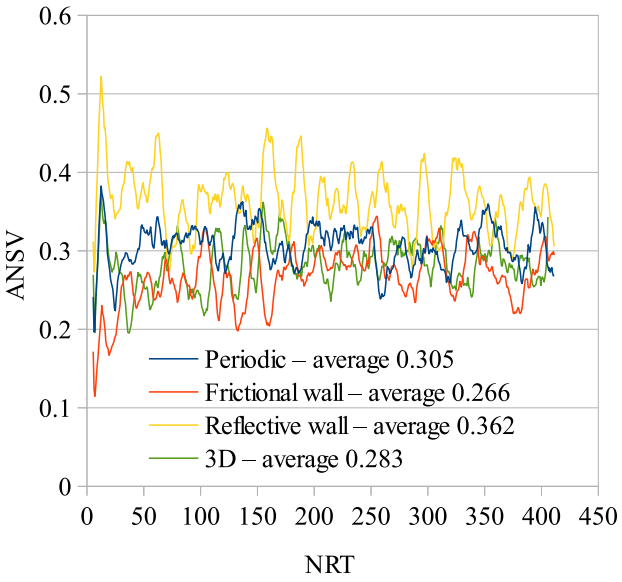

(d) Model B - Bitumen

Figure 6.9: Comparison of effect of boundary conditions on ANSV versus NRT for sand and bitumen using Model A and B.

Initial condition of the bed

The effect of the initial condition of the bed on the segregation process is examined by considering two different scenarios: an initially randomly mixed bed and an initially inversely segregated bed. The formation of the randomly mixed bed was discussed in Section 6.3. The inversely segregated bed is formed by inserting particles in two separate boxes at different elevations. The flotsam particles are inserted in the lower half of the bed height, and jetsam particles are inserted in the top portion of the bed. Particles are settled in the presence of gravity when there is no gas injected at the inlet for 0.5 s.

Figure 6.10 shows the Lacey mixing index in time using periodic boundary condition for the front and back planes. It can be observed that at the macroscopically stable state of the bed, the Lacey mixing index is independent of the initial condition of the bed for both momentum exchange models. In an initially segregated packed bed with periodic boundary conditions for front and back planes, particles are lifted and moved upward when the gas is injected to the inlet, then mixing starts after a very short period with Model A or after a significant period with the Model B type of momentum exchange, as explained next.

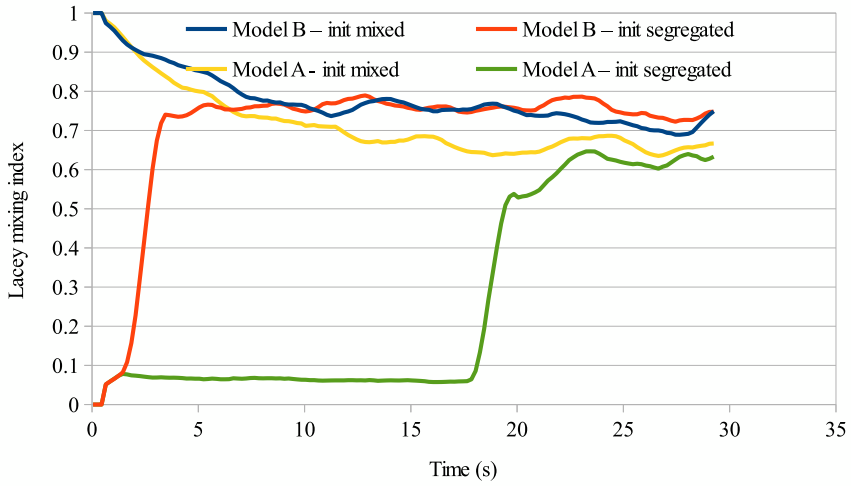

Figure 6.10: Effect of initial condition on Lacey mixing index - Periodic boundary condition.

Figure 6.11 and Figure 6.12 show snapshots of the bed at different time steps using periodic boundary conditions for the front and back planes, and Model A and Model B. For the initially inverse segregated packed bed, particles are lifted and moved to the outlet, where they block the outlet for 18 seconds, if Model A is used for momentum exchange and periodic boundary condition is set for front and back planes. Same results can be observed when Model B is used for the momentum exchange term in an inverse segregated packed bed. However, in this case, the particle cloud at the outlet collapses in less than 2 seconds.

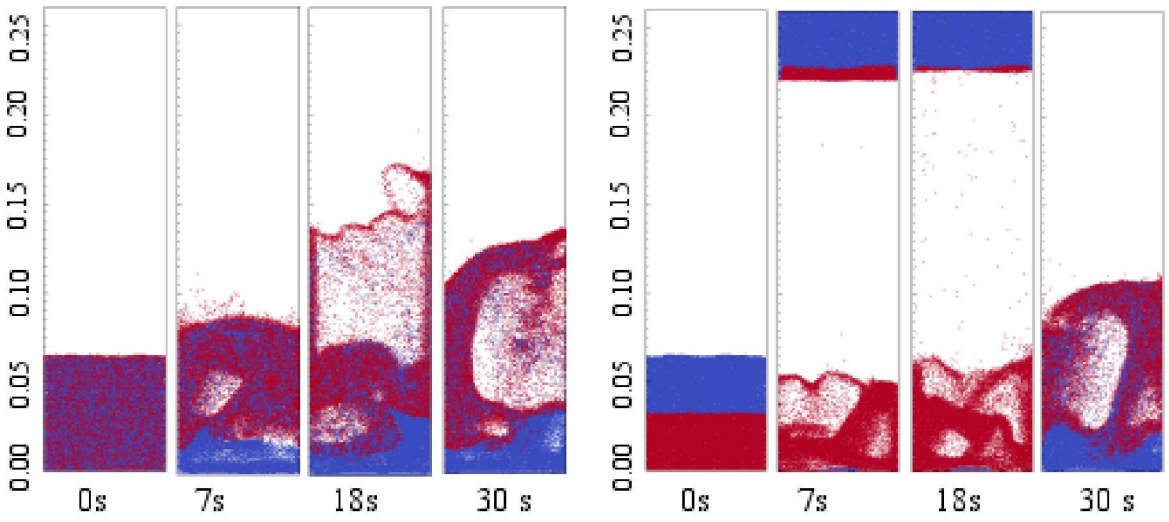

(a) Initially mixed (b) Initially segregated

Figure 6.11: Snapshot of the bed at different times - periodic boundary conditions and Model A.

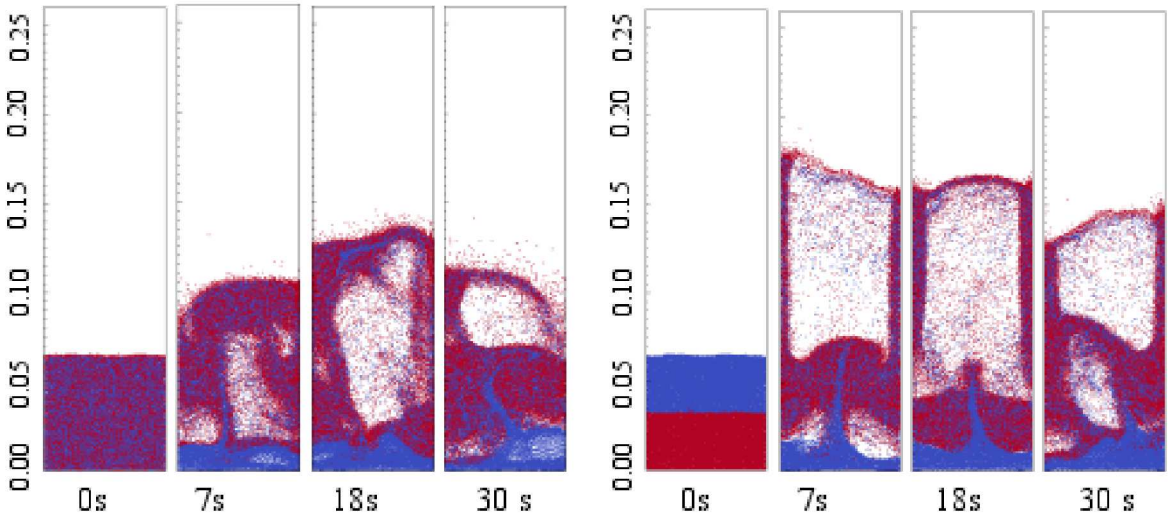

(a) Initially mixed (b) Initially segregated

Figure 6.12: Snapshot of the bed at different times - periodic boundary conditions and Model B.

Figure 6.13 again shows the Lacey mixing index in time, but now using frictional wall boundary condition for the front and back planes. It can be observed that at the macroscopically stable state of the bed, the Lacey mixing index is independent of the initial condition for both boundary conditions (frictional, as well as periodic) and both momentum exchange models. However, a big difference can be observed between the predicted values by Model A and Model B in the case of the frictional boundaries. As it was described in Section 3.5.2, pointwise pressure drop values are needed to calculate the particle - fluid interaction forces. However, by using the local average method pointwise pressure values are not available and only mean values are calculated. This results in differences between the results of Model A and B [Feng and Yu, 2004]. Feng and Yu [2004] verified results of the simulation of a fluidized bed using Model A and Model B for momentum conservation equation set against experiments quantitatively and qualitatively and suggested that results of Model B are more favorable.

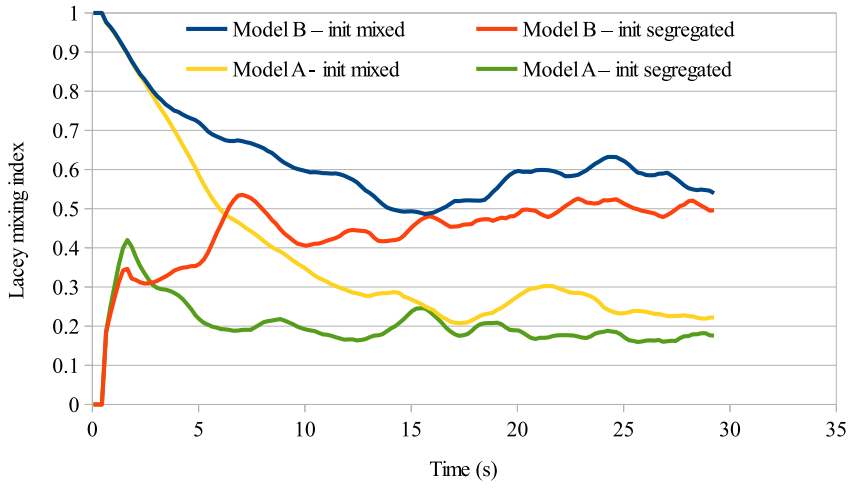

Figure 6.13: Effect of initial condition on Lacey mixing index - frictional wall boundary condition.

Figure 6.14 and Figure 6.15 show snapshots of the bed at different time steps using frictional wall for front and back planes. For an initially segregated packed bed when the gas is injected to the inlet, the bed first expands and collapses, then fluidization begins. Compared to the periodic boundary case, particles are not lifted to block the outlet.

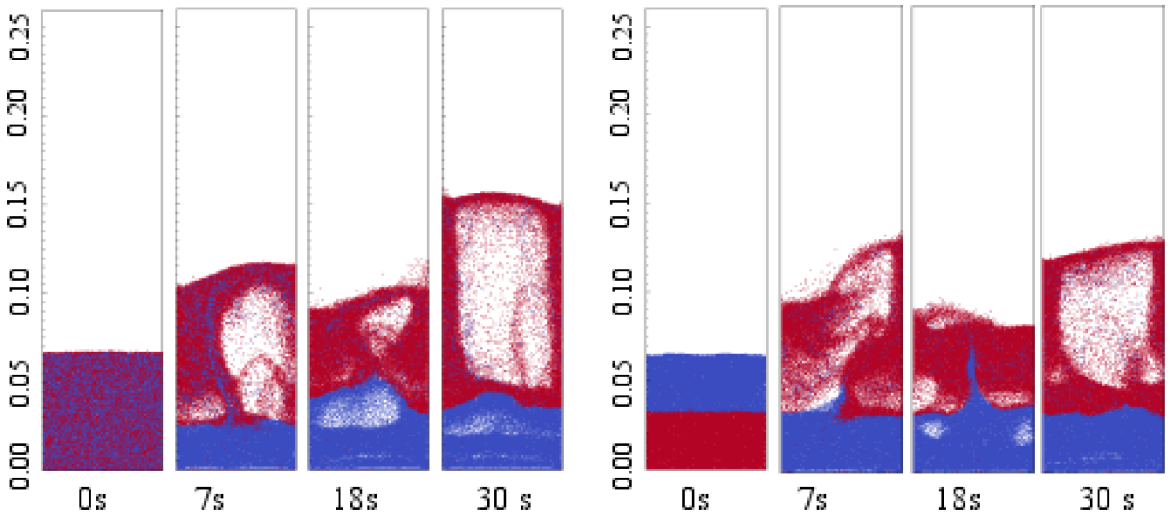

(a) Initially mixed

(b) Initially segregated

Figure 6.14: Snapshot of the bed at different times - frictional wall boundary conditions and Model A.

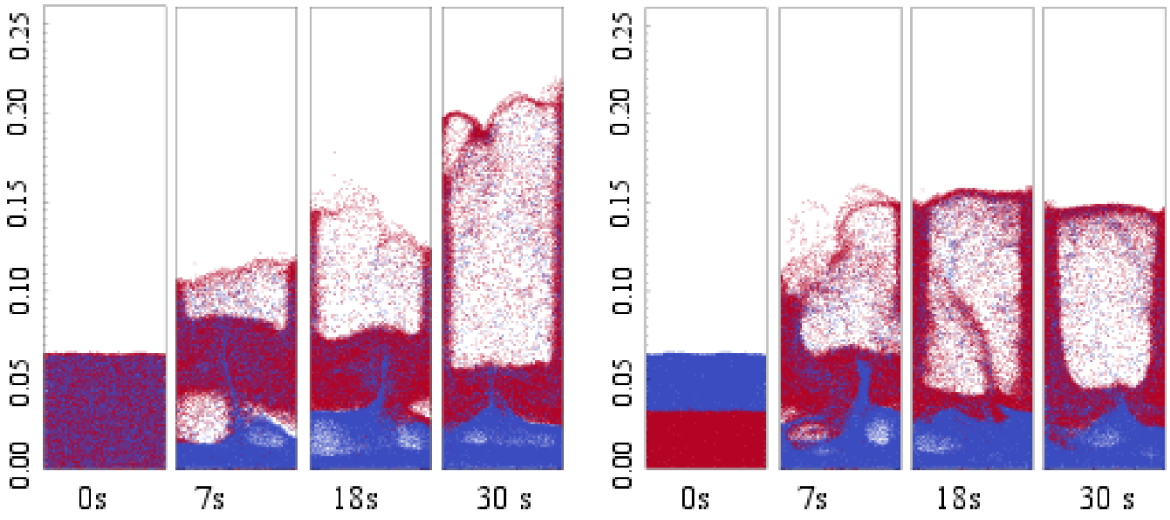

(a) Initially mixed

(b) Initially segregated

Figure 6.15: Snapshot of the bed at different times - frictional wall boundary conditions and Model B.

Effect of the inlet velocity

Gibilaro and Rowe [1974] and Daw and Frazier [1988] suggested that the mixture quality can be affected by the superficial inlet velocity. The effect of the inlet velocity of the segregation process is analyzed in this section. Five different inlet velocities are considered. The minimum fluidization velocity for the jetsam particles is calculated to be 0.6 m s^{-1}, according to Kunii and Levenspiel [1969] Equation 3.3 described in Section 3.2.

Five different inlet velocities are considered to examine the effect of gas velocity on the quality of the mixture. Table 6.5 shows the superficial inlet velocities, which are used in this study.

Table 6.5: Superficial inlet velocities.

Inlet velocity (m s^{-1})	**Comment**
0.55	$0.91U_{mf,jetsam}$
0.6	$1.00U_{mf,jetsam}$
0.75	$1.25U_{mf,jetsam}$
0.9	$1.50U_{mf,jetsam}$
1.05	$1.75U_{mf,jetsam}$

Figure 6.16 (a) shows the Lacey mixing index in time for different inlet velocities when Model A is used for the momentum exchange term. For the inlet velocities lower than the minimum fluidization velocity of jetsam, the bed expands, but fluidization does not happen and the mixing index remains constant around one, which means that particles remain mixed. Particle fluidization is expected at minimum fluidization velocity of the jetsam particles. However, it can be observed that even at this condition the bed is expanded without any fluidization and segregation of particles, which can be confirmed by the constant mixing index in the bed. This makes it clear that Model A, which assumes a highly resolved pressure field in each control volume, instead of the average pressure used in the current carrier phase model, is not ideal for this model combination and Model B should be preferred.

Further increase of the inlet velocity, as exemplified by the gas velocity of $1.25U_{mf,jetsam}$, causes the Lacey mixing index to decrease in time and particles to be segregated. The fastest rate of segregation and the most stable state of the bed is observed in this particular case. Further increase of the inlet velocity, increases the instability of the bed. As a consequence, the Lacey mixing index at the macroscopically stable condition of the bed is higher and fluctuates around the mean value.

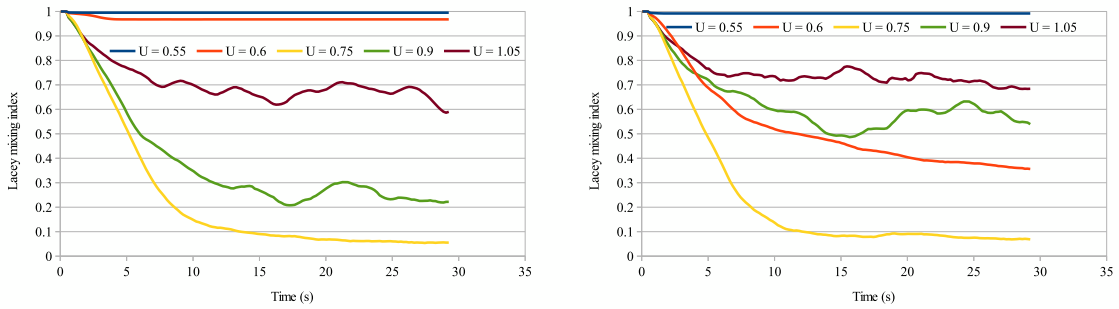

(a) Model A (b) Model B

Figure 6.16: Effect of superficial inlet velocity on Lacey mixing index (a) Model A and (b) Model B.

Figure 6.16 (b) shows the Lacey mixing index in time for different inlet velocities, when Model B is used for the momentum exchange term. At the inlet velocities up to the minimum fluidization velocity of jetsam the bed expands, but there is no fluidization. However, in contrast with Model A, when the inlet velocity is equal to the minimum fluidization velocity of jetsam, fluidization and segregation of particles start. This reveals the effect of momentum exchange model on the results of simulations. Increasing the inlet velocity to $1.25U_{mf,jetsam}$ increases the rate of segregation of particles, while the Lacey mixing index at the macroscopically stable state of the bed reaches its minimum value. Further increase of the inlet velocity leads to increase of Lacey index at the macroscopically stable state of the bed and to its fluctuation, as also shown in the case of Model A.

Summary of comparisons

Comparison of boundary conditions with the 3D case, and results produced by comparison of initial conditions with the results of the inlet velocity analysis suggests that the frictional wall boundary condition for the front and back planes and Model

B for the momentum exchange term produce better qualitative and quantitative results. Model B can be used to study the segregation process in a bed formed from clay and bitumen pellets.

Results of inlet velocity comparison show that when the gas velocity is set to 1.25 times the minimum fluidization velocity of jetsam, the rate of segregation of participles is the highest, and the mixing index has a lower value at the macroscopically stable state of the bed.

6.4 Clay and bitumen

In addition to the inlet velocity, the other factor which has a significant effect on the segregation process is the density ratio of the mixture components. A smaller density ratio is considered to increase the sensitivity of the problem. The density ratio is changed from 2.5 in the previous section to 1.33. Two different types of particles are considered. It is assumed that the jetsam particles are made of a mixture of bitumen and sand with a density of 1600 kg m^{-3} and the flotsam particles are pellets of clay with the density of 1200 kg m^{-3}. Following results of Section 6.3, the Model B is used for the momentum exchange term, the frictional wall boundary condition is used on the front and back planes, and the superficial inlet velocity is set to be $1.25U_{mf,jetsam}$.

The effects of the carrier phase properties and of the bed aspect ratio on the mixture quality are studied in the following sections.

6.4.1 Aspect ratio of the bed

Four different cases are considered to study the effect of the bed aspect ratio on the segregation quality. In the first three cases, the width of the bed is set to be the same, and for the forth case the width of the bed is changed to study the effect on the mixing index of scaling the bed. Air is used as the carrier phase, and the superficial inlet velocity is set to be $1.25U_{mf,jetsam}$. Table 6.6 presents the bed dimensions used in the simulations.

Table 6.6: Bed dimensions.

Case	**Bed width (m)**	**Static bed height (m)**	**Aspect ratio**
Air 0.065:0.065	0.065	0.065	1:1
Air 0.065:0.05	0.065	0.05	1.3:1
Air 0.065:0.032	0.065	0.032	2:1
Air 0.13:0.05	0.13	0.05	2.6:1

Figure 6.17 shows the Lacey mixing index in time for different aspect ratios of the bed. It can be observed that by decreasing the height of the bed the rate of segregation of particles increases and the fastest segregation of particles occurs in a bed with the least static height. By comparing the mixing index of the cases 2 and 4, i.e. with the same bed height but different bed width, it can be seen that the segregation process is not affected by the width of the bed.

It can be concluded that the rate of particles' segregation is not affected by the width of the bed, but it is a significant function of the static height of the bed. However, at the macroscopically stable state of the bed, the mixing index is independent of the aspect ratio of the bed.

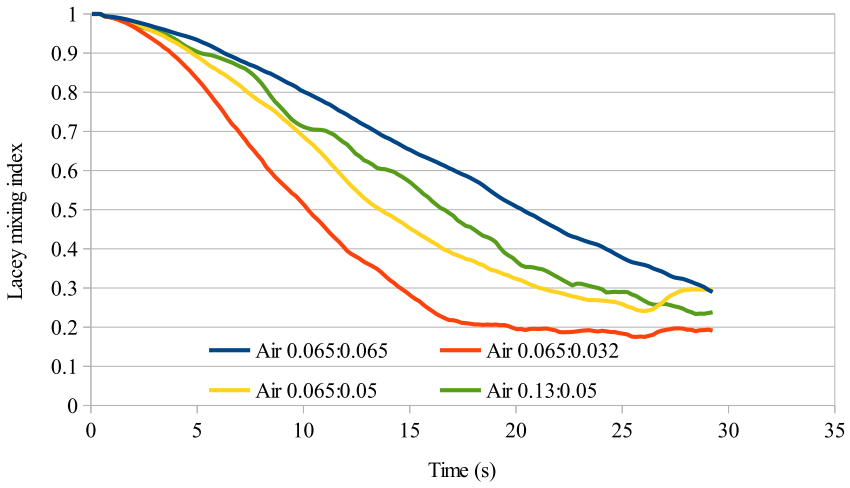

Figure 6.17: Effect of bed aspect ratio on Lacey mixing index.

6.4.2 Carrier phase

Three gasses are considered to study the effect of the carrier phase properties on the segregation of particles. Table 6.7 presents parameters used in the study of the effect of the carrier phase properties on the segregation quality. The bed aspect ratio of 0.065:0.032 is used to minimize the segregation time and reach the stable state condition faster.

Table 6.7: Carrier phase properties.

Variable	**Carrier phase**		
	He	**Air**	**CO_2**
Density (kg m^{-3})	0.222	1.534	2.403
Viscosity (kg $m^{-1}s^{-1}$)	1.603e-5	1.465e-5	1.122e-5
Superficial inlet velocity (m s^{-1})	0.825	0.57	0.5
Particles' Stokes number (-)	11	60	107
Particles' Reynolds number (-)	70	53	61

Figure 6.18 shows the Lacey mixing index in time for the three different carrier phases. Although all simulations were stopped at the physical time of 30 s, the trend of the curves clearly indicates that at the macroscopically stable state of the mixture, segregation of particles can be identical if the inlet velocity of the carrier phase is set properly. Also, it can be observed that the rate of segregation of particles is independent of the carrier phase properties.

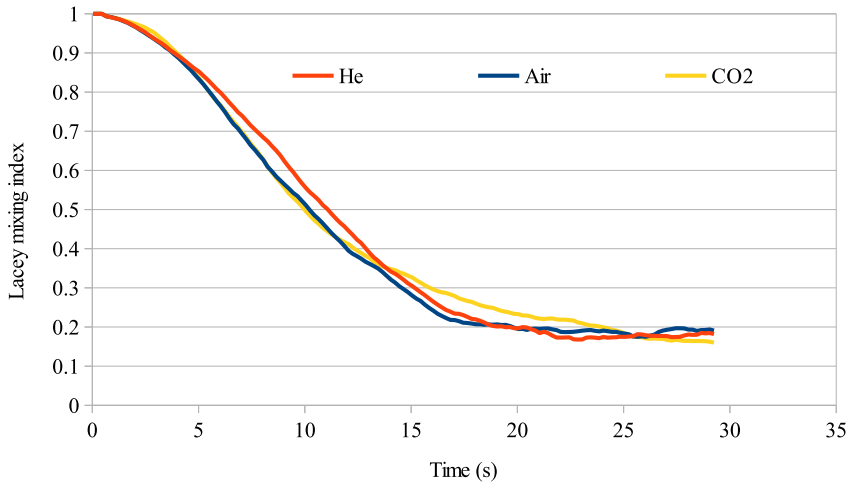

Figure 6.18: Effect of carrier phase properties on Lacey mixing index.

Chapter 7

Conclusion and future work

7.1 Conclusion

The open source CFDEM® coupling was used as the software to develop a model for the process of fluidization and segregation of particles. The Average Normalized Solid Velocity (ANSV) and the pressure drop versus Normalized Run Time (NRT) were used to verify and validate the model. Results of simulations suggest the following conclusions an recommendations for model setup.

- A slice of the bed could be used to represent a full bed, if the slice grid is discretized in the depth to capture the gradients of the flow.
- The frictional wall boundary condition for the front and back planes of the bed slice predicts more accurate results compared to the periodic boundary condition, as it represents better the full size bed.
- The cell size of 2.7 times the particle diameter was found to be suitable to predict the correct pressure drop and grid independent solution.

- The set of Model A momentum conservation equations and also the set of Model B momentum conservation equations predict the same pressure drop values. However, comparison of the results of the Lacey mixing index for both models and also comparison of the results of different inlet velocities suggest that Model B is more favorable to be used to model the fluidized bed, as mentioned by Feng and Yu [2004].

- Koch & Hill, DeFelice and Gidaspow drag models were used to study the effect of drag model on simulations results. The Gidaspow drag model predicted the least pressure drop in the bed compared to DeFelice, and Koch & Hill drag models. The Gidaspow drag model did not follow the bell shape of the void fraction profile proposed by Xu et al. [2004]. The Koch & Hill drag model predicted higher drag at volume fractions compared to DiFelice, which is most likely to happen in a dense fluidized bed.

- The solution of the numerical model, after reaching the macroscopically stable state of the bed, should be independent of the initial conditions, if the boundary conditions and the momentum conservation equations are set properly.

The developed numerical model in the CFDEM® coupling was used to study the effect of the operating conditions of the bed on the segregation process. Particles of the same size and density ratios of 2.5 and 1.33 were considered to examine the segregation process. The ANSV versus NRT and Lacey mixing index versus time were considered to analyze the results, and quantify the quality of the mixture. Results of simulations suggest the following conclusions and recommendations.

- There is an optimum superficial inlet velocity for the segregation of particles in a fluidized bed as it was suggested by Feng and Yu [2007]. The inlet velocity

of $1.25U_{mf,jetsam}$ was found to segregate particles with the highest rate among the tested velocities. This means that the lowest Lacey mixing index at the macroscopically stable state of the bed was observed at this inlet velocity. Also the fastest rate of segregation was found at this same inlet velocity.

- The static height of the bed is inversely correlated with the rate of segregation of particles. However, the macroscopically stable state of the bed is independent of the static height of the bed.

- The rate of segregation of particles and the final state of the bed are independent of the width of the bed.

- The carrier phase thermo-physical properties do not affect the macroscopically stable state of the bed.

7.2 Future work

The current analysis of the segregation process considers a batch of the mixture. However, in the industrial applications of the fluidized bed, the process is mostly a continuous process. The continuous process of segregation of particles can be studied using Eulerian - Lagrangian approach by the CFDEM® coupling software.

The jetsam and flotsam are considered to be the same size. However, the size ratio is one of the dominant factors in segregation of particles. It is necessary to study segregation of particles considering the size ratio of the particles.

In the current work the particles' size is considered to be uniform, and particle size distribution is neglected. However, particles' sizes are mostly distributed about a mean value. It is necessary to study the segregation of particles considering the

size distribution. The Lagrangian approach allows to introduce the size distribution without increasing the complexity of the problem.

The current work assumes particles to be spherical and the shape factor of particles is neglected. However, the shape factor can affect the initial packing of the bed and the drag forces on the particles. It is necessary to study the effect of particles shape factor on the fluidization and segregation processes.

Due to limitations on the available computational power, the size of the bed was considered to be relatively small in the current work. It is necessary to study the scaling process on the fluidization and segregation processes and identify significant factors in the scaling procedure. Discrete Particle Method (DPM) can be implemented to analyze the fluidization and segregation processes in industrial size fluidized beds by considering parcels of particles.

Cooling of particles was one of the objectives of segregation of particles in a fluidized bed in the proposed mechanical separation of bitumen and clay method. However in the current work, the heat transfer was not considered, and it is necessary to consider the heat transfer in the fluidization and segregation processes as one of the objectives of the proposed method.

Bibliography

Government Alberta. Alberta energy: Facts and statistics, 2016. URL http://www.energy.alberta.ca/oilsands/791.asp.

T Bo Anderson and Roy Jackson. Fluid mechanical description of fluidized beds. Equations of motion. *Industrial & Engineering Chemistry Fundamentals*, 6(4): 527–539, 1967.

Ebrahim Azimi. *Simulation and performance characterization of air dense medium fluidized bed for coal beneficiation.* PhD thesis, University of Alberta, 2014.

Ebrahim Azimi, Shayan Karimipour, Petr Nikrityuk, Jozef Szymanski, and Rajender Gupta. Numerical simulation of 3-phase fluidized bed particle segregation. *Fuel*, 150:347–359, 2015.

Ralph A Bagnold. Experiments on a gravity-free dispersion of large solid spheres in a Newtonian fluid under shear. In *Proceedings of the Royal Society of London A: Mathematical, Physical and Engineering Sciences*, volume 225, pages 49–63. The Royal Society, 1954.

HT Bi and JR Grace. Flow regime diagrams for gas-solid fluidization and upward transport. *International Journal of Multiphase Flow*, 21(6):1229–1236, 1995.

National Energy Board. Canada's oil sands. Opportunities and challenges to 2015: An update, 2006.

GA Bokkers, M van Sint Annaland, and JAM Kuipers. Mixing and segregation in a bidisperse gas–solid fluidised bed: a numerical and experimental study. *Powder Technology*, 140(3):176–186, 2004.

Nicholas P Cheremisinoff and Paul N Cheremisinoff. *Hydrodynamics of gas-solids fluidization*. Gulf Publishing Co., Houston, TX, USA, 1984.

Matteo Chiesa, Vidar Mathiesen, Jens A Melheim, and Britt Halvorsen. Numerical simulation of particulate flow by the Eulerian–Lagrangian and the Eulerian–Eulerian approach with application to a fluidized bed. *Computers & Chemical Engineering*, 29(2):291–304, 2005.

Clayton T Crowe, John D Schwarzkopf, Martin Sommerfeld, and Yutaka Tsuji. *Multiphase flows with droplets and particles*. CRC Press, 2011.

Peter A Cundall and Otto DL Strack. A discrete numerical model for granular assemblies. *Geotechnique*, 29(1):47–65, 1979.

CS Daw and GC Frazier. A quantitative analysis of binary solids segregation in large-particle gas-fluidized beds. *Powder Technology*, 56(3):165–177, 1988.

Surya Deb and Danesh Tafti. Discrete element modeling and validation of fluidized bed with multiple jets. In *ASME 2012 Fluids Engineering Division Summer Meeting collocated with the ASME 2012 Heat Transfer Summer Conference and the ASME 2012 10th International Conference on Nanochannels, Microchannels, and Minichannels*, pages 605–613. American Society of Mechanical Engineers, 2012.

R Di Felice. The voidage function for fluid-particle interaction systems. *International Journal of Multiphase Flow*, 20(1):153–159, 1994.

Francesco P Di Maio, Alberto Di Renzo, and Vincenzino Vivacqua. Extension and validation of the particle segregation model for bubbling gas-fluidized beds of binary mixtures. *Chemical Engineering Science*, 97:139–151, 2013.

Alberto Di Renzo, Francesco Paolo Di Maio, Rossella Girimonte, and Brunello Formisani. DEM simulation of the mixing equilibrium in fluidized beds of two solids differing in density. *Powder Technology*, 184(2):214–223, 2008.

Alberto Di Renzo, Francesco P Di Maio, and Vincenzino Vivacqua. Prediction of the flotsam component in a gas-fluidized bed of two dissimilar solids. *International Journal of Chemical Reactor Engineering*, 10(1), 2012.

T. Duma. Mechanical processing of oil sands, December 13 2012. URL http://www.google.com/patents/US20120312723. US Patent App. 13/579,276.

Sabri Ergun. Fluid flow through packed columns. *Chemical Engineering Progress*, 48, 1952.

LT Fan, SJ Chen, and CA Watson. ANNUAL REVIEW solids mixing. *Industrial and Engineering Chemistry*, 62(7):53–69, 1970.

YQ Feng and AB Yu. Assessment of model formulations in the discrete particle simulation of gas-solid flow. *Industrial & Engineering Chemistry Research*, 43 (26):8378–8390, 2004.

YQ Feng and AB Yu. Microdynamic modelling and analysis of the mixing and segregation of binary mixtures of particles in gas fluidization. *Chemical Engineering Science*, 62(1):256–268, 2007.

YQ Feng and AB Yu. CFD-DEM modelling of gas fluidization of particle mixtures with size and density differences. In *Seventh International Conference on Computational Fluid Dynamics in the Process Industries*, pages 9–11, 2009.

YQ Feng, BH Xu, SJ Zhang, AB Yu, and P Zulli. Discrete particle simulation of gas fluidization of particle mixtures. *AIChE Journal*, 50(8):1713–1728, 2004.

Joel H Ferziger and Milovan Perić. *Computational methods for fluid dynamics*. Springer Berlin, 3rd edition, 2002.

D Geldart and A R Abrahamsen. Homogeneous fluidization of fine powders using various gases and pressures. *Powder Technology*, 19(1):133–136, 1978.

Derek Geldart. Types of gas fluidization. *Powder Technology*, 7(5):285–292, 1973.

L G_ Gibilaro and PN Rowe. A model for a segregating gas fluidised bed. *Chemical Engineering Science*, 29(6):1403–1412, 1974.

Dimitri Gidaspow. *Multiphase flow and fluidization: continuum and kinetic theory descriptions*. Academic press, 2012.

MJV Goldschmidt, R Beetstra, and JAM Kuipers. Hydrodynamic modelling of dense gas-fluidised beds: comparison and validation of 3D discrete particle and continuum models. *Powder Technology*, 142(1):23–47, 2004.

Christoph Goniva, Christoph Kloss, Niels G Deen, Johannes AM Kuipers, and Stefan Pirker. Influence of rolling friction on single spout fluidized bed simulation. *Particuology*, 10(5):582–591, 2012. URL http://www.cfdem.com/cfdemrcoupling-open-source-cfd-dem-framework.

A Haider and O Levenspiel. Drag coefficient and terminal velocity of spherical and nonspherical particles. *Powder technology*, 58(1):63–70, 1989.

Y He, NG Deen, M Van Sint Annaland, and JAM Kuipers. Gas- solid turbulent flow in a circulating fluidized bed riser: Experimental and numerical study of monodisperse particle systems. *Industrial & Engineering Chemistry Research*, 48 (17):8091–8097, 2009.

Reghan J Hill, Donald L Koch, and Anthony JC Ladd. The first effects of fluid inertia on flows in ordered and random arrays of spheres. *Journal of Fluid Mechanics*, 448:213–241, 2001a.

Reghan J Hill, Donald L Koch, and Anthony JC Ladd. Moderate-Reynolds-number flows in ordered and random arrays of spheres. *Journal of Fluid Mechanics*, 448: 243–278, 2001b.

Afshin Honarvar, Jon Rozhon, Dinara Millington, Thorn Walden, Carlos A Murillo, and Zoey Walden. *Economic impacts of new oil sands projects in Alberta (2010-2035)*. CERI, 2011.

Lu Huilin, Zhao Yunhua, Jianmin Ding, Dimitri Gidaspow, and Li Wei. Investigation of mixing/segregation of mixture particles in gas–solid fluidized beds. *Chemical Engineering Science*, 62(1):301–317, 2007.

Raad I Issa. Solution of the implicitly discretised fluid flow equations by operator-splitting. *Journal of Computational Physics*, 62(1):40–65, 1986.

Christoph Kloss, Christoph Goniva, Alice Hager, Stefan Amberger, and Stefan Pirker. Models, algorithms and validation for opensource DEM and CFD–DEM.

Progress in Computational Fluid Dynamics, an International Journal, 12(2-3):140–152, 2012. URL www.cfdem.com/liggghtsr-open-source-discrete-element-method-particle-simulation-code.

Donald L Koch and Reghan J Hill. Inertial effects in suspension and porous-media flows. *Annual Review of Fluid Mechanics*, 33(1):619–647, 2001.

Daizo Kunii and Octave Levenspiel. *Fluidization Engineering*. New York : Wiley, [c1969], 1969. ISBN 0471510807.

Daizo Kunii and Octave Levenspiel. Circulating fluidized-bed reactors. *Chemical Engineering Science*, 52(15):2471–2482, 1997.

P_ M_ C_ Lacey. Developments in the theory of particle mixing. *Journal of Applied Chemistry*, 4(5):257–268, 1954.

Joachim Lundberg and Britt M Halvorsen. A review of some existing drag models describing the interaction between phases in a bubbling fluidized bed. In *Proc. 49th Scand. Conf. Simulation and Modeling, Oslo University College, Oslo, Norway*, pages 7–8, 2008.

Kun Luo, Fan Wu, Shiliang Yang, and Jianren Fan. CFD–DEM study of mixing and dispersion behaviors of solid phase in a bubbling fluidized bed. *Powder Technology*, 274:482–493, 2015.

Sung Joon Moon, S Sundaresan, and IG Kevrekidis. Coarse-grained computations of demixing in dense gas-fluidized beds. *Physical Review E*, 75(5):051309, 2007.

Séverine Thérèse FC Mortier, Thomas De Beer, Krist V Gernaey, Jean Paul Remon, Chris Vervaet, and Ingmar Nopens. Mechanistic modelling of fluidized bed drying

processes of wet porous granules: a review. *European Journal of Pharmaceutics and Biopharmaceutics*, 79(2):205–225, 2011.

Christoph R Müller, Stuart A Scott, Daniel J Holland, Belinda C Clarke, Andrew J Sederman, John S Dennis, and Lynn F Gladden. Validation of a discrete element model using magnetic resonance measurements. *Particuology*, 7(4):297–306, 2009.

K Ganesh Palappan and PST Sai. Studies on segregation of binary mixture of solids in a continuous fast fluidized bed: Part i. effect of particle density. *Chemical Engineering Journal*, 138(1):358–366, 2008a.

K Ganesh Palappan and PST Sai. Studies on segregation of binary mixture of solids in continuous fast fluidized bed: Part iii. quantification of performance of the segregator. *Chemical Engineering Journal*, 145(1):100–111, 2008b.

Steve Plimpton. Fast parallel algorithms for short-range molecular dynamics. *Journal of Computational Physics*, 117(1):1–19, 1995. URL http://lammps.sandia.gov/index.html.

M Poux, P Fayolle, J Bertrand, D Bridoux, and J Bousquet. Powder mixing: some practical rules applied to agitated systems. *Powder Technology*, 68(3):213–234, 1991.

A Putnam. Integratable form of droplet drag coefficient. *Ars Journal*, 31(10):1467–1468, 1961.

Akhil Rao, Jennifer S Curtis, Bruno C Hancock, and Carl Wassgren. Classifying the fluidization and segregation behavior of binary mixtures using particle size and density ratios. *AIChE Journal*, 57(6):1446–1458, 2011.

Martin J Rhodes. *Introduction to particle technology*. John Wiley & Sons, 2008.

MJ Rhodes, Xiao Shan Wang, M Nguyen, P Stewart, and Kurt Liffman. Study of mixing in gas-fluidized beds using a DEM model. *Chemical Engineering Science*, 56(8):2859–2866, 2001.

JF Richardson and WN Zaki. The sedimentation of a suspension of uniform spheres under conditions of viscous flow. *Chemical Engineering Science*, 3(2):65–73, 1954.

PN Rowe, AW Nienow, and AJ Agbim. The mechanism by which particles segregate in gas fluidised beds-binary systems of near-spherical particles. *Trans. Inst. Chem. Eng*, 50:310–323, 1972.

L Schiller and Z Naumann. A drag coefficient correlation. *VDI Zeitung*, 77(318):51, 1935.

Ravi Inder Singh, Anders Brink, and Mikko Hupa. CFD modeling to study fluidized bed combustion and gasification. *Applied Thermal Engineering*, 52(2):585–614, 2013.

Vladimír Staněk. *Fixed bed operations: Flow distribution and efficiency*. Prentice Hall, 1994.

Philippe Traoré, Jean-Charles Laurentie, and Lucian Dascalescu. An efficient 4 way coupling CFD–DEM model for dense gas–solid particulate flows simulations. *Computers & Fluids*, 2014.

Takuya Tsuji, Keizo Yabumoto, and Toshitsugu Tanaka. Spontaneous structures in three-dimensional bubbling gas-fluidized bed by parallel DEM–CFD coupling simulation. *Powder Technology*, 184(2):132–140, 2008.

Yutaka Tsuji, Toshihiro Kawaguchi, and Toshitsugu Tanaka. Discrete particle simulation of two-dimensional fluidized bed. *Powder Technology*, 77(1):79–87, 1993.

MA Van der Hoef, M Ye, M van Sint Annaland, AT Andrews, S Sundaresan, and JAM Kuipers. Multiscale modeling of gas-fluidized beds. *Advances in Chemical Engineering*, 31:65–149, 2006.

Qinggong Wang, Yuqing Feng, Junfu Lu, Weidi Yin, Hairui Yang, Peter J Witt, and Man Zhang. Numerical study of particle segregation in a coal beneficiation fluidized bed by a TFM–DEM hybrid model: Influence of coal particle size and density. *Chemical Engineering Journal*, 260:240–257, 2015.

Wei Wang, Bona Lu, Nan Zhang, Zhansheng Shi, and Jinghai Li. A review of multiscale CFD for gas–solid CFB modeling. *International Journal of Multiphase Flow*, 36(2):109–118, 2010.

Henry G Weller, G Tabor, Hrvoje Jasak, and C Fureby. A tensorial approach to computational continuum mechanics using object-oriented techniques. *Computers in physics*, 12(6):620–631, 1998.

CY Wen and YH Yu. A generalized method for predicting the minimum fluidization velocity. *AIChE Journal*, 12(3):610–612, 1966.

CY Wen and YH Yu. Mechanics of fluidization. In *Chem. Eng. Prog. Symp. Ser.*, volume 62, page 100, 2013.

David C Wilcox et al. *Turbulence modeling for CFD*, volume 2. DCW industries La Canada, CA, 1998.

BH Xu and AB Yu. Numerical simulation of the gas-solid flow in a fluidized bed by combining discrete particle method with computational fluid dynamics. *Chemical Engineering Science*, 52(16):2785–2809, 1997.

Guangwen Xu, Guogang Sun, and Shiqiu Gao. Estimating radial voidage profiles for all fluidization regimes in circulating fluidized bed risers. *Powder Technology*, 139 (2):186–192, 2004.

JG Yates. *Fundamentals of Fluidized-Bed Chemical Processes: Butterworths Monographs in Chemical Engineering*. Butterworth-Heinemann, 2013.

Wenqi Zhong, Aibing Yu, Guanwen Zhou, Jun Xie, and Hao Zhang. CFD simulation of dense particulate reaction system: Approaches, recent advances and applications. *Chemical Engineering Science*, 140:16–43, 2016.

ZY Zhou, SB Kuang, KW Chu, and AB Yu. Discrete particle simulation of particle–fluid flow: model formulations and their applicability. *Journal of Fluid Mechanics*, 661:482–510, 2010.

HP Zhu, ZY Zhou, RY Yang, and AB Yu. Discrete particle simulation of particulate systems: theoretical developments. *Chemical Engineering Science*, 62(13):3378–3396, 2007.

HP Zhu, ZY Zhou, RY Yang, and AB Yu. Discrete particle simulation of particulate systems: a review of major applications and findings. *Chemical Engineering Science*, 63(23):5728–5770, 2008.

Appendix A

Dictionary files

Numerical schemes:

fvSchemes

```
/*--------------------------------*- C++ -*----------------------------------*\
| =========                 |                                                 |
| \\      /  F ield         | OpenFOAM: The Open Source CFD Toolbox           |
|  \\    /   O peration     | Version:  1.6                                   |
|   \\  /    A nd           | Web:      www.OpenFOAM.org                      |
|    \\/     M anipulation  |                                                 |
\*---------------------------------------------------------------------------*/
FoamFile
{
    version     2.0;
    format      ascii;
    class       dictionary;
    location    "system";
    object      fvSchemes;
}
// * * * * * * * * * * * * * * * * * * * * * * * * * * * * * * * * * * * * //

ddtSchemes
{
    default         Euler;
}

gradSchemes
{
    default         Gauss linear;
    grad(p)         Gauss linear;
    grad(U)         Gauss linear;
}

divSchemes
{
```

```
    default                                 Gauss linear;
    div(R)                                  Gauss linear;
    div(phi,U)                              Gauss limitedLinearV 1;
    div(phi,k)                              Gauss limitedLinear 1;
    div(phi,epsilon)                        Gauss limitedLinear 1;
    div(phi,R)                              Gauss limitedLinear 1;
    div(phi,nuTilda)                        Gauss limitedLinear 1;
    div((viscousTerm*dev(grad(U).T())))     Gauss linear;
    div((nu*dev(grad(U).T())))              Gauss linear;
    div((nuEff*dev(grad(U).T())))           Gauss linear;
}

laplacianSchemes
{
    default                                 Gauss linear corrected;
    laplacian(viscousTerm,U)                Gauss linear corrected;
    laplacian(nu,U)                         Gauss linear corrected;
    laplacian(nuEff,U)                      Gauss linear corrected;
    laplacian((1|A(U)),p)                   Gauss linear corrected;
    laplacian((voidfraction2|A(U)),p)       Gauss linear corrected;
    laplacian(DkEff,k)                      Gauss linear corrected;
    laplacian(DepsilonEff,epsilon)          Gauss linear corrected;
    laplacian(DREff,R)                      Gauss linear corrected;
    laplacian(DnuTildaEff,nuTilda)          Gauss linear corrected;
}

interpolationSchemes
{
    default         linear;
    interpolate(U)  linear;
}

snGradSchemes
{
    default         corrected;
}

fluxRequired
{
    default         no;
    p               ;
}


// ************************************************************************* //
```

The ddtSchemes is the temporal numerical scheme ($\frac{\partial \phi}{\partial t}$, $\frac{\partial \rho \phi}{\partial t}$) and the keyword *Euler* represents the first order implicit Euler scheme.

The gradSchemes is used to define the numerical scheme for gradient terms. The default value is set to Gauss integration with linear (central difference scheme (CDS)) interpolation scheme. The pressure and velocity gradient terms are defined.

The divSchemes is used to define the numerical schemes for the divergence terms. The divergence scheme for the default value and Reynolds stress terms ($\nabla \cdot R$), div(R), are set to Gauss integration with linear (CDS) interpolation scheme. The convection term of the velocity ($\nabla \cdot (\phi U)$), div(phi,U), is estimated with Gaussian integration with limitedLinearV interpolation scheme. The limitedLinearV is an improved version of limited linear differencing interpolation scheme for vectors, which take into account the direction of the field. The convection term for the kinetic turbulence energy, div(phi,k), turbulence dissipation, div(phi,epsilon), Reynolds stress term, div(phi,R) and the kinematic turbulence viscosity, div(phi,nuTilda), are estimated by the Gaussian integration with limitedLinear interpolation scheme. The divergence of the viscous term, $\nabla \cdot (\tau + \tau_T)$, is represented by ((viscousTerm*dev(grad(U).T()))), div((nu*dev(grad(U).T()))), div((nuEff*dev(grad(U).T()))) entries and each term is used based on the applied turbulence model.

The laplacianSchemes is used to define the numerical schemes for the laplacian terms. The default keyword is set to Gauss integration with linear corrected numerical scheme. The keyword *linear* represents the linear (central difference scheme(CDS)) and *corrected* is used for unbounded, first order and conservative numerical behaviour. for this scheme the terms represent as below:

laplacian(viscousTerm,U)	$\nabla \cdot \tau \nabla U$
laplacian(nu,U)	$\nabla \cdot \nu \nabla U$
laplacian(nuEff,U)	$\nabla \cdot \nu_{eff} \nabla U$
laplacian((1| A(U)),p)	$\nabla \mathrm{A}^{-1} \cdot \nabla p$
laplacian((voidfraction2| A(U)),p)	$\nabla \cdot \epsilon_g \mathrm{A}^{-1} \nabla p$
laplacian(DkEff,k)	$\nabla \cdot D^{(\widetilde{k})} \nabla \widetilde{k}$
laplacian(DepsilonEff,epsilon)	$\nabla \cdot D^{\epsilon} \nabla \epsilon$
laplacian(DREff,R)	$\nabla \cdot D^{\widetilde{R}} \nabla \widetilde{R}$
laplacian(DnuTildaEff,nuTilda	$\nabla \cdot D^{\nu_t} \nabla \nu_t$

- A^{-1} is the inverse of the diagonal elements in the discretised momentum equation.
- $D^{(\widetilde{k})}$ is the diffusion coefficient of the turbulence kinetic energy.
- D^{ϵ} is the diffusion coefficient of the turbulence kinetic energy dissipation.
- $D^{\widetilde{R}}$ is the diffusion coefficient of the Reynolds stress tensor.
- D^{ν_t} is the diffusion coefficient of the turbulence viscosity.

The snGradSchemes is used to define the surface normal gradients and the corrected scheme is used , which represents an explicit non orthogonal correction for the surface normal gradients.

The fluxRequired is used to define fields which are required to generate the flux. The pressure field flux is define to be generated.

Equation solvers, tolerance and algorithms:

fvSolution

```
/*--------------------------------*- C++ -*----------------------------------*\
| =========                 |                                                 |
| \\      /  F ield         | OpenFOAM: The Open Source CFD Toolbox           |
|  \\    /   O peration     | Version:  1.6                                   |
|   \\  /    A nd           | Web:      www.OpenFOAM.org                      |
|    \\/     M anipulation  |                                                 |
\*---------------------------------------------------------------------------*/
FoamFile
{
    version     2.0;
    format      ascii;
    class       dictionary;
    location    "system";
    object      fvSolution;
}
// * * * * * * * * * * * * * * * * * * * * * * * * * * * * * * * * * * * * * //

solvers
{
    "(p)"
    {
        solver          PCG;
        preconditioner  DIC;
        tolerance       1e-06;
        relTol          0.1;
    }

    pFinal
    {
        solver          PCG;
        preconditioner  DIC;
        tolerance       1e-06;
        relTol          0;
    }

    "(U|k|epsilon|R|nuTilda)"
    {
        solver          PBiCG;
        preconditioner  DILU;
        tolerance       1e-05;
        relTol          0;
    }

    "(voidfraction|Us|Ksl|dSmoothing|UsNext|voidfractionNext)"
    {
        solver          PCG;
        preconditioner  DIC;
        tolerance       1e-05;
        relTol          0;
    }
}

PISO
{
    nCorrectors     4;
    nNonOrthogonalCcorrectors 1;
    pRefCell        0;
    pRefValue       0;
}

```

```
61
62 // ************************************************************************ //
```

Appendix B

Mixing index code

```
1
2  clc;
3  clear all;
4  close all;
5  fclose all;
6  format long
7
8  Stime=input('Start time = ');
9  Ftime=input('End time = ');
10 DeltaT=input('Time step = ');
11
12 W=input('Domain width = ');
13 H=input('Domain height = ');
14
15 Nx=input('Divisions in X = ');
16 Nsample=input('Number of particles in cells = ');
17
18 rA=input('Paricle A radius in m = ');
19 rB=input('Particle B radius in m = ');
20
21 RuA=input('Particle A density = ');
22 RuB=input('Particle B density = ');
23
24 VA=4/3*pi*rA^3;% Volume of particle A
25 VB=4/3*pi*rB^3;
26
27 x=linspace(0,W,Nx);
28 time=[Stime:DeltaT:Ftime];
29
30
31 % Defining the mesh in x coordinate
32
33
34 for i=1:1:length(time)
35     cd(['./CFD/' num2str(time(i)) '/lagrangian/particleCloud']);
36
37     fidpos=fopen('positions','r');
38     for j=1:1:17
39     temp=fgets(fidpos);
```

```
    end
    temp=textscan(fidpos,'%f\n',1);
    TotPar(i)=temp{1};
    temp=fgets(fidpos);
    temp=textscan(fidpos,'%1s %f %f %f %1s %f\n');
    Pos{i}=[temp{2}(1:end-1,1) temp{3}(1:end-1,1) temp{4}(1:end-1,1)];


    fidr=fopen('r','r');
    for j=1:1:18
    temp=fgets(fidr);
    end
    temp=fgets(fidr);
    temp=fgets(fidr);
    temp=textscan(fidr,'%f\n');
    r{i}=temp{1};



sampN=TotPar./Nsample;




    for j=1:1:length(x)-2
        ParIndx{i}{j}= find(Pos{i}(:,1)>=x(j) & Pos{i}(:,1)<x(j+1));
        ParIndxCount(i,j)=length(ParIndx{i}{j});
    end
    j=length(x)-1;
        ParIndx{i}{j}= find(Pos{i}(:,1)>=x(j) & Pos{i}(:,1)<x(j+1));
        ParIndxCount(i,j)=length(ParIndx{i}{j});


Ny=floor(ParIndxCount/Nsample);




  for j=1:1:length(x)-1
        [yValue ParIndy{i}{j}]=sort(Pos{i}(ParIndx{i}{j},2));
    end



for j=1:1:length(x)-1
        for k=1:1:Ny(i,j)
     Cell{i}{j}(:,k)=ParIndx{i}{j}(ParIndy{i}{j}...
         ((k-1)*Nsample+1:k*Nsample));
        end
    end



 for j=1:1:length(x)-1
        for k=1:1:Ny(i,j)
            NA{i}{j}(k)=sum(r{i}(Cell{i}{j}(:,k))==rA);
            NB{i}{j}(k)=sum(r{i}(Cell{i}{j}(:,k))==rB);
        end
```

```
    end



     for j=1:1:length(x)-1
        for k=1:1:Ny(i,j)
            temp=NA{i}{j}(k)+NB{i}{j}(k);
           fracA{i}{j}(k)= NA{i}{j}(k)/temp;
           fracB{i}{j}(k)=NB{i}{j}(k)/temp;
        end
    end



    meanfracA(i)=0;
    meanfracB(i)=0;
    for j=1:1:length(x)-1
        for k=1:1:Ny(i,j)
            meanfracA(i)=meanfracA(i)+fracA{i}{j}(k);
            meanfracB(i)=meanfracB(i)+fracB{i}{j}(k);
        end
    end
     meanfracA(i)=meanfracA(i)/sum(Ny(i,:));
     meanfracB(i)=meanfracB(i)/sum(Ny(i,:));



    stdfracA(i)=0;
    stdfracB(i)=0;
    for j=1:1:length(x)-1
        for k=1:1:Ny(i,j)
            stdfracA(i)=stdfracA(i)+(fracA{i}{j}(k)-meanfracA(i)).^2;
            stdfracB(i)=stdfracB(i)+(fracB{i}{j}(k)-meanfracB(i)).^2;
        end
    end
     stdfracA(i)=stdfracA(i)/sum(Ny(i,:));
     stdfracB(i)=stdfracB(i)/sum(Ny(i,:));



    clear Pos r yValue Ny ParIndx ParIndxCount ...
    ParIndy fracA fracB temp NA NB Cell
        fclose all;
    cd ../../../..
end

 sigr=meanfracA.*(1-meanfracA)./Nsample;
 sig0=meanfracA.*(1-meanfracA);
 sigA=stdfracA;
 sigB=stdfracB;



 MIA=(sig0-sigA)./(sig0-sigr);


figure;
hold on;
```

```
156 plot(time,MIA,'k-o')
157 title('Lacey mixing index in time')
158 xlabel('Time s')
159 ylabel('Lacey Mixing Index')
160 print('MI_','-depsc')
161 CSV=[time',MIA']
162 csvwrite('MI',CSV)
```